Ensemble Simulations of Atmospheric Angular Momentum and its Influence on the Earth's Rotation

Dissertation

zur

Erlangung des Doktorgrades (Dr. rer. nat.)

der

Mathematisch-Naturwissenschaftlichen Fakultät

der

Rheinischen Friedrich-Wilhelms-Universität Bonn

vorgelegt von

Timo Winkelnkemper

aus

Hilden

Bonn, Juli 2008

Contents

CONTENTS

Kurzfassung

Der Drehimpulsaustausch zwischen der festen Erde und der Atmosphäre sorgt für kleine messbare Schwankungen in der Erdrotation. In den letzten Jahren verbesserte sich die Qualität der geodätischen Beobachtungen und der atmosphärischen Modellierung und führte zu neuen Erkenntnissen über Erdrotationsschwankungen. Atmosphärische Zirkulationsmodelle simulieren die Massenbewegungen und die Massenkonzentrationen auf der globalen Skala realistisch. Die Atmosphäre hat aufgrund von Variationen in ihrer Massenverteilung und Dynamik einen großen Einfluss auf die Erdrotationsparameter (ERPs). Für diese Arbeit wurden Ensemblesimulationen mit dem globalen Zirkulationsmodell ECHAM5 für den Zeitraum 1880 bis 2006 gerechnet. Zum Antrieb der Simulationen wurden Meeresoberflächentemperaturen, Meereis-, Treibhausgas-, Aerosolkonzentrationen und solare Einstrahlung vorgegeben. Um langzeitliche Trends in den ERPs abschätzen zu können, wurden A1B-Szenarienläufe von 2000 bis 2060 mit dem gekoppelten Atmosphären-Ozean-Modell ECOCTH verwendet.

Eine Strukturanalyse vergleicht Zeitreihen der beobachteten und von Reanalysen abgeleiteten ERPs mit simulierten Werten. Im Allgemeinen können die ECHAM5 Simulationen im Vergleich zu den Vorgängerversionen einen größeren Teil der beobachteten Varianz in den ERPs erklären. Schwankungen in den ERPs, die auf die quasi-biennial oscillation zurückzuführen wären, werden nicht simuliert, da das Modell keine stratosphärischen Windoszillationen im entsprechenden Frequenzbereich enthält. Durch ENSO und den Jahresgang verursachte Schwankungen der Tageslänge (LOD) werden gut wiedergegeben. Ähnlich zu den atmosphärischen Reanalysen wird die Amplitude der Halbjahresoszillation signifikant unterschätzt; sie erreicht lediglich ca. 66 Prozent des beobachteten Wertes.

Eine Varianzanalyse der Ensemblesimulationen zeigt, dass die Halbjahreswelle nur zu einem geringen Anteil durch externe Faktoren bestimmt wird, sondern vielmehr ein Ergebnis interner Prozesse ist. Variationen lokaler Drehimpulsdichten werden über dem tropischen Ozean hauptsächlich durch externe Antriebe bestimmt. Im simulierten Jahresgang der axialen Drehimpulskomponente werden signifikante Abweichungen von einer überlagerten halb- und ganzjährlichen harmonischen Schwingung in den Monaten Mai und Juni während des starken Abfalls festgestellt. Diese nicht-harmonischen Anteile müssen im Spektrum durch höher frequente Signale beschrieben werden.

Die äquatoriale x-Komponente des simulierten atmosphärischen Drehimpulses korreliert signifikant mit der solaren Einstrahlung. Die von ozeanischen und Gezeiteneffekten korrigierte beobachtete Polbewegung korreliert signifikant mit den entsprechenden simulierten atmosphärischen Anregungen.

Die ECOCTH Szenarienläufe induzieren einen, ausschließlich durch den Windterm bedingten, Zuwachs in der LOD von $0.26 \pm 0.03 ms$ für das Jahr 2060. Das ECHO-G Modell projiziert hingegen einen Anstieg von $0.17 \pm 0.03 ms$, der auch einen kleinen signifikanten Anteil des Massenterms beinhaltet.

Die meisten Studien über den atmosphärischen Einfluss auf die Erdrotation benutzen Reanalysedaten. Als Fazit lässt sich festhalten, dass der gewählte Modellansatz den Vorteil bietet, dass sich die Variabilität in den ERPs klar in Teile interner und extern angetriebener Variabilität unterscheiden lässt. Außerdem lassen sich mögliche zukünftige Zustände im System Erde-Atmosphäre ableiten. Bei einem teilweise chaotischen System wie der Atmospäre besitzen abgeleitete Größen (z.B. ERPs) deterministische und stochastische Anteile, Ensemblesimulationen können dies respektieren.

Abstract

The exchange between angular momentum of the solid portion of the Earth and of the atmosphere plays a vital role in exciting small but measurable changes in the rotation of our planet. Recent improvements in geodetic data and atmospheric research has allowed for new insights into fluctuations of the Earth's rotation. Atmospheric general circulation models (GCMs) are able to simulate mass movements and mass concentrations on a global scale in a realistic way. Due to enormous changes in the mass distribution and motions relative to the rotating Earth the atmosphere has an important impact on Earth rotation parameters (ERPs). For this thesis ensemble simulations with the ECHAM5 GCM for the period from 1880 to 2006 have been conducted — driven by sea surface temperatures, sea ice concentrations, green house gas concentrations, aerosols, and solar forcing. For the purpose of investigating possible future long term trends in ERPs, A1B scenario runs from 2000 to 2060 were carried out with the coupled atmosphere-ocean GCM ECOCTH.

A detailed structure analysis compares time series of observed ERPs and those deduced from atmospheric reanalyses with the atmospheric ensemble sim-

ulations. In general ECHAM5 is able to explain a larger proportion of the variance in observed ERPs than its predecessors. Fluctuations in Earth rotation linked to the quasi-biennial oscillation are not present in the simulations, as the model fails to generate this stratospheric mode. Variations in the length-of-day (LOD) induced by ENSO and the annual cycle are well comprehended by the simulation. As for reanalyses the amplitude of the semiannual cycle is significantly underestimated and only reaches about 66 percent of the observed one.

An analysis of variance of the ensemble simulations indicates that the semi-annual variations can not be explained by external boundary conditions to a large extent. They are primarily driven by internal processes. Densities of local atmospheric angular momentum (AAM) variations tend to be mainly driven by boundary conditions over sea in the tropics. Significant departures from harmonic annual and semiannual oscillations in the seasonal axial AAM cycle are found during the strong annual decrease in May and June, resulting in higher frequency contributions in the power spectrum.

The equatorial x-component of the simulated AAM shows a significant statistical correlation with the solar irradiance. Observed polar motion with the oceanic and tidal effects removed shows significant correlations with both the simulated equatorial x- and y-component of the atmospheric excitation.

The ECOCTH scenario runs show a significant increase in LOD by $0.26 \pm 0.03ms$ for the year 2060, solely caused by an increase in the motion term. However, under the same conditions the ECHO-G model projects a smaller trend with an increase of $0.17 \pm 0.03ms$ for the year 2060 containing a small but significant positive contribution of the matter term.

Most studies dealing with the impact of the atmosphere on Earth rotation use reanalysis data. As a conclusion it is stated, that model approaches are able to clearly distinguish between internally induced and externally driven variability. Additionally possible future states of the whole Earth-atmosphere system can be derived. Variables (e.g. ERPs) derived from a partially chaotic system, such as the atmosphere, contain deterministic and chaotic signals. Ensemble simulations are able to respect the nature of these signals.

CONTENTS

Chapter 1

Introduction

1.1 Motivation

For more than a century, the rotation of the Earth has been known to vary by small but measurable amounts. The Earth's rotation affects our daily life in many ways. The most prominent effect is the direct one which determines the time of the day. Collateral indirect effects have forced cultures to adapt in the past. For instance diurnal and semidiurnal tides are caused by the daily revolution of the planet. Nowadays the economy and modern societies have an enormous interest in a superior knowledge of variations in the Earth rotation. Atmospheric analyses and forecasts are used to improve the determination and prediction of changes in the Earth's orientation in space, which is of increasing importance to space agencies and global positioning techniques.

Throughout the entire last century the quality of polar motion observation was rather adequate. Some of the observed temporal changes have long been recognised as being due to the exchange of angular momentum between the solid Earth and the atmosphere. With the advent of both modern geodetic observation techniques on the one hand and global atmospheric analyses based on atmospheric general circulation models on the other, it has become possible to make detailed assessments of the extent to which fluctuations in A̲tmospheric A̲ngular M̲omentum (AAM) are responsible for the observed changes in the E̲arth R̲otation P̲arameters (ERPs). ERP variations are measured with respect to a uniformly rotating geocentric reference with its z-axis, about which it rotates, pointing approximately to the direction of the maximum moment of inertia. Changes in the angular velocity of the Earth lead to changes in the L̲ength O̲f the D̲ay (LOD) and changes in the position of the Earth's pole of rotation are

linked to *polar motion.*

The atmospheric contribution to changes in the Earth's rotation is important for a variety of reasons. Other geophysicists like to be able to evaluate the atmosphere's contribution to the Earth's motion so that they can study other remaining effects, such as that of the Earth's liquid core, core-mantle coupling, ocean, hydrosphere, biosphere etc. Finally, for the meteorologists themselves fluctuations in AAM can give information about the large scale behaviour of the atmosphere. ERPs are measurable variables containing informations of global AAM components. AAM components are the only measurable integral variables of the whole atmospheric system. This work was part of a joint project from oceanography, hydrology, geodesy and meteorology. The project exists for more than ten years. Throughout the research process earlier versions of atmospheric <u>G</u>eneral <u>C</u>irculation <u>M</u>odels (GCMs) were used. Those predecessors failed to explain some major observed characteristics of AAM components.

1.2   Aims

The aims of this thesis can be formulated in questions which will be addressed:

- State-of-the-art atmospheric GCMs have established a higher quality and a more detailed description of the general atmospheric circulation in recent years. But what about the global and local angular momenta? Has their quality improved as well?

- What are the structural characteristics of GCM derived AAM? Where are differences to reanalysis AAM in frequency, time and spatial domain?

- Statistically GCM derived AAM time series can be regarded as a superposition of a signal coming along from external boundary conditions and "noise" from internal variations. To what extent can the variance of AAM time series be explained by external boundary conditions?

- The atmosphere is a stochastic system. A model based approach is able to derive conditional probability densities given the external boundary conditions of the model. What about these "uncertainties" and their structure?

- Economic and demographic conditions are unknown for the future. Scenarios describe different possible economic, demographic and ecological developments (Nakicenovic and Swart, 2000). Scenario driven atmospheric

GCM runs indicate an increase in axial AAM within the 21st century. Can we trust them, how certain are they? How well do observed and simulated long term trends correspond with each other?

1.3 From History to Current Research Fields

An historic synopsis of achievements in Earth system science starts in 1687 when Newton published his famous work "Philosophiae Naturalis Principia Mathematica" where he postulated his famous three laws of motion. This work forms the basis for classical mechanics. In principle, all further works on Earth system science can be traced back to these fundamental laws.

Euler's equations describing the rotation of a rigid body in a frame of reference fixed in the rotating body were derived from the idea of seeing a body as many fixed mass points (Demtröder, 2000). The set of coupled non-linear differential equations is able to describe the rotation of a rigid body in a fixed reference frame in the rotating body. Some characteristics of the Earth's rotation can be assessed from Euler's equations. For instance one can derive a free nutation movement of the Earth's rotation axis from this set of equations after making the assumption of two equally sized equatorial moments A and B and neglecting external torques which is quite realistic to the Earth. The solution of these equations showed an oscillation of the position of the poles with a frequency of about 304 days which Euler forecasted in 1758. He could not prove his hypothesis as at that time there were no accurate and reliable measurements of polar motion available.

It took nearly one hundred years until Peters in 1844 had first hints that Euler was right and the rotation axis of the Earth does indeed vary in space with respect to the Earth reference system. To get further knowledge of the Earth's rotation observatories intensified their measurements in the second half of the 19th century. Polar motion would manifest itself as periodic variations in latitude of the observatory.

In 1876, the English physicist William Thomson pointed out that polar motion might be much more complex than generally believed due to possible redistributions of matter in and on the Earth which would influence the position of the pole itself. Thomson expected a more or less irregular phenomenon. As Friederich Küstner (1856-1936) was investigating the constant of aberration by carefully observing stars from the Berlin observatory, it turned out that there is

a variation of latitude from a few tenths of a second of arc in about one year. In 1888 the announcement of his observation aroused great international interest.

The private American astronomer Seth Carlo Chandler (1846-1913) made stellar observations parallel to Küstner's ones, however, neither was aware of the other's work. Chandler had observed the identical effect but, unlike Küstner, still refused to publish it. When reading Küstner's report Chandler became very ambitious in this matter and wanted clarity on this effect. Thorough investigations of all appropriate observation series made in the world during the last 50 years were started by him and should lead to a robust result. Finally in 1891 when he had analysed several simultaneous series, he was ready to publish a great surprise, in "On the Variation of Latitude" in the Astronomical Journal. The general result of preliminary discussions was to show a revolution of the Earth's pole, from West to East, with a radius of thirty feet, measured at the Earth's surface. But he stated a period of 427 days, contradicting perspicuously Euler's predictions of 304 day. This result was not expected at all and lots of doubts about Chandler's research remained. Chandler himself could offer no plausible explanation.

Others went into this field and the real reason was quickly discovered. In 1891, Newcomb was able to demonstrate that an elastic body would lengthen the period effectively compared to a rigid body, less than one year after Chandler detected the 427 day period in polar motion. On the other hand Newcomb argued that the ocean pole tides lead to a lengthening of the polar motion period as well. His calculations predicted a 443 days periodicity combining these two effects. This result was fairly close to the actual frequency and it considered already all major effects on polar motion.

After Küstner and Chandler had demonstrated the need for independent observations of astronomical latitude from different points on the Earth's surface, enormous efforts were made in this field. An international bureau has been established to organise and collect certain measurements all around the world.

During the past decades remarkable advances in the field of Earth's rotation have been achieved. Particularly the role of Earth's fluid surroundings — namely ocean and atmosphere — in contributing to changes in Earth rotation were a major topic of research. Nowadays it is commonly accepted that the dominant excitation of nontidal changes in Earth rotation from intradaily up to the decadal time scales is the atmosphere. More precisely stated it is the change in mass dis-

tribution and mass movements within the atmosphere.

The pursuit of this result has encompassed a wide spectrum of research, including studies of tropospheric and stratospheric wind fields, the E1 Niño / Southern Oscillation (ENSO) phenomenon, the Quasi-Biennial Oscillation (QBO) in the tropical stratosphere, and tropical 40-50 day wind Madden Julian Oscillations (MJO).

Meteorologists' interest in the subject of Earth's rotation dates back to Starr (1948). Although primarily concerned with explaining how the atmosphere's jet streams are maintained against dissipation, Starr noted in passing that *"there is no reason to expect that the partition of angular momentum - between the solid Earth and the atmosphere — should remain constant when seasonal and other short time-intervals are considered."*

Munk and Miller (1950) then pointed out that seasonal changes in AAM should be able to explain variations in LOD. They quantified the magnitude of seasonal changes and derived corresponding LOD variations. They are known to be the first to estimate LOD variations directly from meteorological measurements. Further progress was established by Munk and MacDonald (1960). Advances in geodynamics, instrumentation and international co-operation improved the quality of observational data for both atmosphere and the Earth's angular velocity leading to a more precise assessment of the atmospheric effect on LOD. They could explain about 60 percent of the seasonal LOD cycle by atmospheric effects. Another achievement which was published in their book was to show the equivalence of the torque and angular momentum approach which will be discussed in chapter 5.

Twenty years later Lambeck (1980) gave an extensive and comprehensive overview of the geophysical causes and consequences of the Earth's variable rotation. He assigned variations of characteristic frequencies to certain geophysical causes. The approach to distinguish effects by their frequencies is still very popular and will be used throughout this work, too. In the same year Hide et al. (1980) used a data set covering the whole troposphere. He postulated that core-mantle interaction does not contribute to interannual and higher frequency variations, which is still accepted but not yet proven. Similar to Lambeck he could show that the different extent of the Northern Hemisphere and Southern Hemisphere seasonal cycle in AAM leads to a global annual signal. Hide was one of the first to be concerned about the error estimation of the AAM. For the geodetic ob-

servations every measurement is accompanied by accurate error estimations. He gave a rudimentary but practical AAM error estimation by taking atmospheric data from two independent weather services. It is currently still very difficult to estimate errors in the atmospheric data as only very few reanalysis data sets exist (namely the European, American and Japanese service who operationally calculate AAM estimates). Rosen and Salstein (1983) extended the insights of Hide and used modern meteorological reanalysis data covering a six year period. They also looked at regional contributions to the global AAM and were able to do so as geodetic observations and meteorological data had improved dramatically since 1980.

A conceptual theoretical framework to link variations in polar motion and LOD to AAM was developed by Barnes et al. (1983). He formulated dimensionless functions which describe the excitations of polar motion and LOD variations. Today the transformation to these excitation functions — simply called χ-functions — is commonly used and applied to all geophysical fluids.

The historic outline ends here. In the early 1980s paradigms research into Earth rotation changed. Then scientists started to investigate much more specific issues of Earth's rotation. Previous achievements so far formed the basis for analysing certain effects. Works and research after 1983 will be introduced within this work when it seems more thematically appropriate.

1.4 Reference Data

The high quality of observational data in the field of the Earth's rotation and atmospheric reanalysis have boosted research activity since 1980. The fundamental theoretical background was already well comprehended decades earlier and scientists yearned for a higher quality of data. This chapter will briefly introduce observational data including atmospheric reanalysis which will be used as a reference in this study.

1.4.1 Geodetic Observation of Earth Rotation

This work is a nice example of a highly interdisciplinary research area. It combines fields of meteorology/climatology, oceanography, hydrology and geodesy in a very intense way. The latter is responsible for accurate measurements of ERPs by combining several independent techniques on the one hand and on the other

hand it provides knowledge of the interior of the solid Earth which is also an important aspect in Earth system modelling. Parameters of Earth rotation are monitored by the International Earth Rotation and Reference Systems Service (IERS). This service provides daily measurements of ERPs. The C04 time series published by the IERS is a high quality product which provides pole coordinates and length of day measurements with error estimates from the year 1962 to present (McCarthy and Petit, 2004). Earlier measurements were not based on atomic clock time measurements. In the 1950s the quality of the angular velocity measurements was heavily improved by the introduction of the atomic clock. In the following the C04 time series is used as geodetic reference throughout this work. In recent years five major observational techniques independently measure ERPs:

- Global Positioning System (GPS)

- Satellite Laser Ranging (SLR)

- Lunar Laser Ranging (LLR)

- Very Long Baseline Radio Interferometry (VLBI)

- Doppler Orbit determination and Radiopositioning Integrated on Satellite (DORIS)

Furthermore, VLBI measurements improved the quality of the data stepwise in 1980 as they were introduced and in 1984 as a huge network was installed (Pâquet et al., 1997). The technique is the most accurate and most important for measuring LOD. Nowadays it contributes 94 percent to the LOD published by the IERS. A closer look at the technical properties will follow in the next chapter.

Very Long Baseline Interferometry

Very Long Baseline Interferometry (VLBI) is a technique in radioastronomy allowing for high precision space and position measurements. It is commonly used for astronomic observations and geodetic applications.

The measurement of ERPs is based on the measurements of extragalactic space objects — such as radio galaxies or quasars/quasi-stellar objects. These objects themselves, starlike in appearance and irradiating spectra with characteristically large redshifts are an optimal reference to measure because a special quasar is easy to identify, sends varying signals in time and is very far away. The

temporal difference in the arrival of a special signal of a single quasar at different observational locations is the observed variable. The target variables are the precise coordinates of the observational locations and their temporal changes. An accurate monitoring of the Earth's irregular rotation is derived. Precision to some millimetres is a big benefit which comes along with a VLBI network involving many observational locations. One can show that the error of the VLBI derived measurements depends inversely on the volume spanned by the observatories.

The synchronisation of parallel measurements by high precision clocks helps reduce errors. Modern radio telescopes are able to record 5 to 20 different extragalactic radio sources within an hour. These capabilities are used operationally to span a huge network.

The Earth's rotation forces incessantly change positions of the observational locations in time with respect to a fixed reference frame. Taking all positional changes of observational locations into account all ERPs can be derived.

Some filters are applied to the raw measurement data set to correct the effects of disturbances — such as:

- tropospherical refraction — dry and wet: correction regards temperature and pressure,

- ionospherical refraction depends on frequency of radio waves,

- time after synchronisation events,

- instrumental effects, and others.

Removing Tidal Effects on Earth's Rotation

Oceanic tides influence the rotational properties of the Earth effectively (Doodson and Warburg, 1941). Not only the well known diurnal and semidiurnal variations but also lower frequency variations leave a fingerprint in ERPs. For instance, there are also tidal variations in rotation rate and polar motion caused by the near-equilibrium long-period tides, which have periods from about 9 days to 18.6 years. Two effects of ocean tides can cause variations in the Earth's rotation. As the tides move water around the globe the total mass distribution of the Earth ocean system changes, and hence the moment of inertia of the

Earth changes. Through conservation of angular momentum, the solid Earth changes its rotation rate accordingly. The other mechanism is due to tidal currents which slow down or speed up, they exchange angular momentum with the solid earth, which is manifested in the rotation rate (Munk and MacDonald, 1960). The motion effect is slightly more important for rotation rate variations and both mechanisms are about equally important for polar motion variations. Both mechanisms are well comprehended in ocean models and their effects on ERPs can be calculated quite accurately (Brosche et al., 1989).

Compared to atmospheric and other oceanic drivers of ERP variations the errors of tidal effects on ERP changes are some orders of magnitudes smaller. Forecasts of tidal effects achieve similar precision as their ephemeris forcing is at hand for future conditions. The tidal effect can be regarded as an effect caused by superposing lunar, solar and planetary gravitational potentials affecting the ocean. Models, describing the zonal tidal effect on LOD are described by a superposition of a couple of harmonic oscillations coming from diverse configurations of moon, sun and major planets.

These so called constituents and their characteristics are listed in the appendix C. The tidal model used for filtering the raw ERP C04 data set is compliant with the IERS 2000 conventions containing 63 major constituents. In table C.1 the column "UT1-UT1R" gives the amplitude of the single constituent's effect on ΔLOD (McCarthy and Petit, 2004). Important frequencies are found at periods of 13.66 days (moon's libration period), 27.56 days (period of Earth-moon distance called anomalistic month), 182.62 days (half year), 365.26 days (year) and 6790.36 days (lunar node period). In the following the tidal corrected ERPs are meant when talking about ERPs.

1.4.2 Atmospheric Reanalysis Data

In numerical weather prediction (NWP) the observational data are adjusted to an atmospheric model. The analysis scheme respects statistical-dynamical relations of a variable in time and space and between other variables (Hense, 2008). Observations from radiosondes, satellite measurements, remote sensing, aircraft, ship and local station measurements are adopted in the so-called data-assimilation. All the measurement data are interpolated to a three dimensional grid. Reanalysis projects arising in the 1990s were using the analysis schemes from NWP to make backwards analysis taking all data available into account. Reanalyses form a consistent data set for all meteorological parameters because the same analysis

scheme with the same set of parameterisations is applied to the observations for several decades. For each time step the reanalysis can intuitively be regarded as the most probable state of the atmosphere given the related observations. The NCEP and ERA40 data sets have advantages and disadvantages therefore both data sets are selectively used in dependence of their specific appropriateness. E.g. NCEP covers a greater time span with more recent values whereas ERA40 has a finer grid resolution especially in the vertical.

NCEP/NCAR

The NCEP reanalyses (Kalnay et al., 1996) cover a period from 1948 to present. The temporal resolution is six hours. The data is available on a 2.5x2.5 degree regular grid on 17 pressure level (up to 10 hPa) or on a 192x94 gaussian grid with 28 level of an orography following vertical coordinate. It is pointed at literature where the NCEP II data set can be found. It is based on another analysis scheme with higher resolution and shorter temporal coverage. Referring to the notation, throughout this work the term NCEP stands for the NCEP data set described by (Kalnay et al., 1996).

ERA40

The ERA40 reanalyses (Uppala et al., 1999) are based on the analysis scheme of the operational ECMWF weather model. They cover the period from mid 1957 to mid 2001 with a minimum time step of six hours. The highest available global resolution is T159 with a corresponding 480x240 gaussian grid coinciding with a distance of two neighbouring grid points of $\sim 0.75°$. The orography following vertical coordinate is divided into 60 levels.

Chapter 2

Statistical Analysis

Atmospheric GCM simulations generate a huge amount of data. The atmospheric standalone simulations which have been conducted for the research produced more than 10,000 GB. To analyse the data statistical postprocessing is needful. This chapter is divided into two sections. The "Sample Analysis" section treats statistical aspects of given samples and the "Frequency Analysis" section deals with time series and their statistical analyses in frequency domain. Some of the concepts which will be outlined in the following "Sample Analysis" section will also be applied to time series. The section will point at limitations and necessary assumptions when dealing with time series.

Evidently, this chapter does not cover the entire statistics. In the following only those parts of statistics are introduced which are relevant for this work. The whole chapter is drawn on the works of Storch and Zwiers (1999); Hense et al. (2005) and Schoenwiese (2006) who give a more detailed and comprehensive coverage of statistics.

2.1   Sample Analysis

Every new experiment conducted is called a *realisation*. The results from an experiment may have discrete or continuous values. Results from a finite number of experiments will span a certain finite space within the space of all conceivable results. The space spanned by results of an infinite number of realisations is called *sample space* $\mathcal{S}$.

A non-empty sample space always has a subspace $\mathbf{A}$ of $\mathcal{S}$. Hence, it is possible to decide for every result of a realisation whether it is in or it is not in $\mathbf{A}$. If the

result is in $\mathbf{A}$, it is called *event A*. Alternatively it is called the *complement of event $\overline{A}$*.

2.1.1 Probability of an Event

For N realisations of an experiment with discrete sample space the *probability* of the occurrence of an event A is defined as:

$$P(A) = \lim_{N \to \infty} \frac{n(A)}{N} \tag{2.1}$$

The term $n(A)$ represents the number of occurrences of the event A. Kolmogorov (Kolmogoroff, 1933) defined three axioms for probabilities:

- The probability of an event $P(E)$ is positive semidefinite:

$$P(E) \geq 0 \tag{2.2}$$

- The probability that some elementary event in the entire sample space will occur is 1. More specifically, there are no elementary events outside the sample space.

$$P(E) = 1 \tag{2.3}$$

- Any countable sequence of pairwise disjoint events $E_1, E_2, \ldots$ satisfies:

$$P(E_1 \cup E_2 \cup \ldots) = \sum_i P(E_i) \tag{2.4}$$

2.1.2 Univariate Continuous Random Variables

This work is solely based on continuous variables (zonal wind (u), surface pressure (p_{surf}), temperature (T), atmospheric angular momentum (AAM), etc.), thus sample spaces are continuous as well. In such sample spaces no "discrete" probabilities $P(x)$ for the event of a certain number x exist. Let the sample space $\mathcal{S}$ be a one dimensional continuous interval $I = [a, b]$, a univariate real random variable is defined as the set $\mathbf{X}$:

$$\mathbf{X} = \{(x, F(x)), x \in I\} \tag{2.5}$$

The monotonically increasing function $F(x)$ maps the interval I onto the finite interval $[0, 1]$. It fulfils the following three axioms:

$$0 \leq F(a) \leq F(b) \leq 1 \tag{2.6}$$

$$\lim_{x \to a} F(x) = 0 \tag{2.7}$$

$$\lim_{x \to b} F(x) = 1 \tag{2.8}$$

The function $F(x)$ is called *cumulative distribution function* (cdf) and returns the probability $F(x) = P(\mathbf{X} \leq x)$ that the random variable $\mathbf{X}$ exceeds a certain value x.

For $F(x)$ being continuously differentiable the derivative $f(x) = F'(x)$ exists. The derivative $f(x)$ is the *probability density function* (pdf). In the following random variables are assumed to be continuous, univariate and real.

2.1.3 Moments of a Random Variable

The k-th moment of the random variable $\mathbf{X}$ is defined by:

$$m_k = \int_a^b x^k \, f(x) \, dx \tag{2.9}$$

and the k-th central moment by:

$$\mu_k = \int_a^b (x - m_1)^k \, f(x) \, dx \ . \tag{2.10}$$

The first moment m_1 is often called *expectation value* $E(\mathbf{X})$ of $\mathbf{X}$. The second central moment μ_2 is the *variance* $Var(\mathbf{X})$ of $\mathbf{X}$:

$$Var(\mathbf{X}) = E((\mathbf{X} - E(\mathbf{X}))^2) \tag{2.11}$$

The *standard deviation* σ is expressed by:

$$\sigma = \sqrt{Var(\mathbf{X})}. \tag{2.12}$$

2.1.4 Quantiles

For the cdf $F(x)$ of a random variable $\mathbf{X}$ being strictly monotonic increasing and $p \in (0, 1)$:

$$F^{-1}(p) := inf\{x \in \mathbb{R} : F(x) \geq p\} \tag{2.13}$$

defines the quantile function. The return $F^{-1}(p)$ is called the *p-quantile* of $\mathbf{X}$ and $F^{-1}(p = 0.5)$ is called the *median* of $\mathbf{X}$.

2.1.5 Correlation

The correlation coefficient between two random variables $\mathbf{X}$ and $\mathbf{Y}$ with mean μ_X and μ_Y respectively is defined by the normalised covariance between the two variables. For the covariance given by:

$$\text{Cov}(\mathbf{X},\mathbf{Y}) = E((\mathbf{X}-\mu_X)(\mathbf{Y}-\mu_Y)) \tag{2.14}$$

the correlation coefficient follows directly by

$$\rho_{XY} = \frac{\text{Cov}(\mathbf{X},\mathbf{Y})}{\sigma_X \sigma_Y} \tag{2.15}$$

with $\sigma_X = \sqrt{\text{Var}(\mathbf{X})}$ and $\sigma_Y = \sqrt{\text{Var}(\mathbf{Y})}$. For a sample of n independent realisations $\{x_1, \ldots, x_n\}$ and $\{y_1, \ldots, y_n\}$ an estimator of the correlation coefficient ρ_{XY} is

$$\hat{\rho}_{XY} = \frac{\sum_{i=1}^{n}(x_i - \overline{x})(y_i - \overline{y})}{\sqrt{\sum_{i=1}^{n}(x_i - \overline{x})^2 \sum_{i=1}^{n}(y_i - \overline{y})^2}}. \tag{2.16}$$

For bivariate normally distributed $(\mathbf{X},\mathbf{Y})$ Eq. 2.16 is the maximum likelihood estimator (Storch and Zwiers, 1999).

2.1.6 Auto-correlation

Suppose that $\mathbf{X}_t$ is a stationary process with mean μ. A stochastic process $\mathbf{X}_t : t\epsilon\mathbb{N}^+$ is called *stationary* if all stochastic properties are independent of index t. The auto-covariance function of lag-τ is then defined by:

$$\gamma = E((\mathbf{X}_t - \mu)(\mathbf{X}_{t+\tau} - \mu)^*) \tag{2.17}$$

$$= \text{Cov}(\mathbf{X}_t, \mathbf{X}_{t+\tau}) \tag{2.18}$$

The *-sign denotes the adjoint form of the matrix. By normalising one obtains the auto-correlation function of $\mathbf{X}_t$,

$$\rho(\tau) = \frac{\gamma(\tau)}{\gamma(0)}. \tag{2.19}$$

The notation in the following will be compliant to Zwiers and von Storch (1995) with ρ_{xx} identifying the auto-correlation function of $\mathbf{X}_t$.

For the applications within this theses an important aspect which comes along temporal auto-correlation has to be respected. In order to test the statistical robustness of a certain parameter statistical tests will be performed. These statistical tests use the sample size n_X of an independent sample $\{x_1^{\text{ind.}}, \ldots, \text{x}_{\text{n}_\text{X}}^{\text{ind.}}\}$ as free parameter. These tests are only valid for an independent sample. To comply this demand an equivalent sample size has to be considered for dependent samples. The use of an equivalent sample size n'_X faces the problem of overconfidence when dealing with auto-correlated data.

In meteorology and climatology time series are generally auto-correlated at least for small lags τ. Auto-correlated time series contain less information than independent samples because some of the information is already comprehended in the neighbouring values. The equivalent sample size n'_X is defined as the number of independent random variables that are needed to provide the same amount of information about the parameter.

Let $\{x_1^{\text{dep.}}, \ldots, \text{x}_{\text{n}_\text{X}}^{\text{dep.}}\}$ be a dependent sample taken from a time series with constant size of time steps. The variance of the sample mean follows the definition of n'_X:

$$\text{Var}(\overline{x}) \quad = \quad \sigma^2/n'_X \qquad\qquad , \text{with} \qquad (2.20)$$

$$n'_X \quad = \quad \frac{n_X}{1 + 2\sum_{\tau=1}^{n_X-1}(1 - \frac{\tau}{n_X})\rho_{XX}(\tau)} \qquad (2.21)$$

2.1.7 Normal Distribution

The pdf of a normal distribution $\mathcal{N}(\mu, \sigma)$ is denoted by:

$$\text{f}_N(x) = \frac{1}{\sqrt{2\pi}\sigma}\exp\left(-\frac{1}{2}\left(\frac{x-\mu}{\sigma}\right)^2\right) \qquad (2.22)$$

The normal distribution (or gaussian distribution) is an important distribution of univariate continuous random variables. A major reason for the importance of the normal distribution is the *central limit theorem*:

Let $\mathbf{X}_1, \mathbf{X}_2, \mathbf{X}_3, \ldots, \mathbf{X}_n$ be a sequence of n independent and identically distributed random variables having each finite values of expectation $\text{E}(\mathbf{X_i}) = \mu$ and variance $\text{Var}(\mathbf{X_i}) = \sigma^2 > 0$. The central limit theorem states that as the sample

size n increases, the distribution of the sample average of these random variables approaches the normal distribution irrespective of the shape of the original distribution.

$$\lim_{n\to\infty} \frac{\frac{1}{n}\sum_{i=1}^{n}(\mathbf{X}_i - \mu)}{\frac{1}{\sqrt{n}}\sigma} \in \mathcal{N}(0,1) \tag{2.23}$$

Throughout this work other distributions are required, their definitions can be found in standard textbooks (Schoenwiese, 2006; Storch and Zwiers, 1999; Hense et al., 2005).

2.1.8 Simple Linear Regression and Linear Trend Estimation

This chapter wants to basically introduce the method of linear regression (compare Storch and Zwiers, 1999) as it will be used for trend estimation in chapter five and six. The aim here is also to give respect to the uncertainties occurring in a trend estimation.

The main idea is to presume a linear statistical model in a sense that a response variable $\mathbf{Y}$ depends linearly on an indicator variable $\mathbf{X}$, for a sample of n realisations $(x_i, y_i) : i = 1, \ldots, n$ of the random variable pair $(\mathbf{X},\mathbf{Y})$ the formulation in terms of the statistical model would yield

$$y_i = a_0 + a_1 x_i + e_i \tag{2.24}$$

In the following independent realisations i and identically bivariate normally distribution for every random variable pair $(\mathbf{X}_i, \mathbf{Y}_i)$ are assumed to be valid. In the field of regression the term e_i is called "residual". If estimates $\hat{a}_0$ and $\hat{a}_1$ for the parameter pair a_0, a_1 were at hand, the realised errors e_i would be estimated by:

$$\hat{e}_i = y_i - \hat{a}_0 - \hat{a}_1 x_i \tag{2.25}$$

Now one can think of a metric describing the size of all errors. For normally distributed data a popular and convenient metric is *the sum of squared errors* defined by $\sum_{i=1}^{n} \hat{e}_i^2$. The corresponding estimators for the parameters a_0, a_1 are then called *least square* estimators.

Demanding minimisation of the sum of squared errors $\sum_{i=1}^{n} \hat{e}_i^2 \stackrel{!}{=} min.$ reduces the degrees of freedom in a manner that solutions for the parameters can be formulated as

$$\hat{a}_0 = \overline{y} - \hat{a}_1 \overline{x} \tag{2.26}$$

$$\hat{a}_1 = \frac{\sum_{i=1}^{n} x_i y_i - n\overline{xy}}{\sum_{i=1}^{n} x_i^2 - n\overline{x}^2}. \tag{2.27}$$

The term $\frac{1}{n} \sum_{i=1}^{n} \hat{e}_i^2$ is an optimistic estimate of the error variance σ_E^2 because the fit of the statistical model reduces the number of degrees of freedom by two. Therefore an unbiased estimate is given by

$$\hat{e}_E^2 = \frac{\sum_{i=1}^{n} \hat{e}_i^2}{n-2} \tag{2.28}$$

The parameter a_1 describes the slope of the line fit. To test the certainty of the slope estimation for a particular value $\tilde{a}_1$ of this parameter the following null hypothesis is useful:

$$H_0 : \hat{a}_1 - \tilde{a}_1 = 0 \tag{2.29}$$

The corresponding T-statistic looks as follows:

$$T = \frac{\hat{a}_1 - \tilde{a}_1}{\frac{\sigma_E}{\sqrt{S_{XX}}}} \tag{2.30}$$

against critical values from the Student-t-distribution with $n-2$ degrees of freedom $T \sim t(n-2)$. S_{XX} denotes the sum of squares concerning the realisations x_i with $S_{XX} = \sum_{i=1}^{n} (x_i - \overline{x})^2$.

For time series the slope parameter is conform to the linear trend. Throughout this work the test procedure is solely applied to time series.

2.1.9 Gaussian Mixture Models

A probability density distribution of a general mixture model is a linear combination of other pdfs. In case of a Gaussian mixture model these probability distributions are normal.

Suppose that the random variable $\mathbf{X}$ is a mixture of n component discrete random variables $\mathbf{Y}_k$. Then, the probability mass function of $\mathbf{X}$, $f_X(x)$, is a weighted sum of its component distributions (Everitt and Hand, 1981).

$$f_X(x|y_k) = \sum_{k}^{n} \mathrm{P}(\Theta_{i,k}|y_k) f_Y(x|y_k, \Theta_{i,k}) \tag{2.31}$$

test result	H_0 is true / H_A is false within the population	H_A is true / H_0 is false within the population
H_0 accepted	correct, $1 - \alpha$	type II error β
H_A accepted	type I error α	correct, $1 - \beta$

Table 2.1: Decision table of a hypothesis test.

The term $P(\Theta_{i,k}|y_k)$ denotes the prior probability of the ith component parameter $\Theta_{i,k}$ given a cluster y_k. The distribution of each cluster is normal $f_Y(x|y_k, \Theta_{i,k}) = \mathcal{N}_k(\Theta_{i|k})$ with parameters $\Theta_{i,k}$.

In order to ensure that the resulting function $f_X(x|y_k)$ of the random variable $\mathbf{X}$ is a probability density function the prior probabilities have to fulfil:

$$\sum_k^N P(\Theta_{i,k}|y_k) = 1 \ \lor P(\Theta_{i,k}|y_k) \geq 0. \tag{2.32}$$

2.1.10 Hypothesis Testing

In many cases assumption about the population from which a sample is drawn do exist. A statistical hypothesis test determines objectively how well the result of the sample and the assumption agree (Hense et al., 2005; Storch and Zwiers, 1999). This assumption is expressed in the *null hypothesis* H_0. The *alternative hypothesis* H_A is disjoint to H_0. The procedure of hypothesis testing is not able to decide whether H_0 or H_A is correct with absolute certainty. It can only return significance/error levels wherein the decision is correct.

In general the test procedure processes as follows. Firstly the null hypothesis H_0 and the alternative hypothesis H_A are formulated. Next, a *significance level* or *error level* α is set. The error level α represents the probability that H_0 will be rejected although it is true (*type I error*). In case of any rejection, it is stated that "the null hypothesis H_0 is rejected with a significance of α". The alternative hypothesis H_A will be offered as unproven statement. Beside a type I error another error may occur. The null hypothesis H_0 could be accepted although it is not true (*type II error*). The probability of such an error is β which is unknown in general, it depends on α and H_A.

Table 2.1 illustrates the definitions of type I and type II errors. The *power* of a test is denoted by $(1 - \beta)$. This means a powerful test is a test which has a small type II error β.

Student's T-test

The Student's t-test is a common statistical test which has some limitations. A short introduction will be given in this section. The t-test is a parametric test of the null hypothesis that two univariate gaussian variables $\mathbf{X}$ and $\mathbf{Y}$ have equal means:

$$H_0 : \mathrm{E}(\mathbf{X}) = \mathrm{E}(\mathbf{Y}) \Leftrightarrow \mu_X = \mu_Y \tag{2.33}$$

The assumptions mentioned and another restriction have to be considered concerning the t-test. T-testing demands that both random variables have the same variance $\mu_X = \mu_Y$. In most cases the variances are unknown. Therefore it is recommended to perform a test on equal variances (e.g. F-test is adequate, see next section). Admittedly for large sample sizes the t-test is quite robust against departures of the variance precondition. For samples $\{x_1, \ldots, x_{n_X}\}$ and $\{y_1, \ldots, y_{n_Y}\}$ the optimal test statistic is stated by (Storch and Zwiers, 1999):

$$t = \frac{\hat{\mu}_X - \hat{\mu}_Y}{S_P \sqrt{\frac{1}{n_X} + \frac{1}{n_Y}}} \tag{2.34}$$

$$S_P^2 = \frac{\sum_{i=1}^{n_X}(x_i - \hat{\mu}_X)^2 + \sum_{i=1}^{n_Y}(y_i - \hat{\mu}_Y)^2}{n_X + n_Y - 2} \tag{2.35}$$

For a valid null hypothesis (2.33) the t-statistic (2.34) is t-distributed with $n_X + n_Y - 2$ degrees of freedom $t \sim \mathbf{t}(n_X + n_Y - 2)$.

Another application of the t-test quite frequently used in this research is outlined in the following. Any estimated correlation between two samples ought to be statistically tested. For independent samples $\{x_1, \ldots, x_n\}$ and $\{y_1, \ldots, y_n\}$ from bivariate normally distributed random variables $\mathbf{X}$ and $\mathbf{Y}$ the null hypothesis to be tested is:

$$H_0 : \rho_{XY} = 0 \tag{2.36}$$

The advisable t-statistic returns:

$$t = \hat{\rho}_{XY} \sqrt{\frac{n - 2}{1 - \hat{\rho}_{XY}^2}} \tag{2.37}$$

for comparison with critical values from the t-distribution $t(n - 2)$. In this work negative correlations are regarded as well, which leads to the alternative hypothesis:

$$H_1 : \rho_{XY} \neq 0 \tag{2.38}$$

The alternative hypothesis determines a two-sided test. Note, that for practical

applications dependent samples will be assumed, meaning that the equivalent sample size n' (see Eq. 2.21) replaces the "real sample size" n in Eq. 2.37.

F-test

The F-test is the fundamental statistical test of the ANalysis Of VAriance (ANOVA) concept which will be introduced later (see section 2.1.14). In the previous subsection identical variances were assumed, this characteristic should as well be tested. The F-statistic is adequate for such a purpose. The standard application of the F-test is to test whether two Gaussians $\mathbf{X}$ and $\mathbf{Y}$ have the same variance, the appropriate null hypothesis is:

$$H_0 : \sigma_X^2 = \sigma_Y^2 \tag{2.39}$$

The alternative hypothesis is:

$$H_1 : \sigma_X^2 \neq \sigma_Y^2 \tag{2.40}$$

For given independent samples $\{x_1, \ldots, x_{n_x}\}$ and $\{y_1, \ldots, y_{n_y}\}$ the F-ratio is calculated by:

$$F = \frac{\sigma_X^2}{\sigma_Y^2} \tag{2.41}$$

H_0 is rejected, if the F-ratio is less than the $(1 - \tilde{p}(\alpha))/2$-quantile or greater than the $(1+\tilde{p}(\alpha))/2$-quantile of the corresponding F-distribution $F(n_X-1, n_Y-1)$. At this point it is alluded that the F-distribution is sensitive to departures from a Gaussian and dependent samples. Note also, that the alternative hypothesis could have different formulation (e.g.: $H_1 : \sigma_X^2 > \sigma_Y^2$) which would result in a "one-sided" test, whereas the alternative hypothesis (2.40) resulted in a "two-sided" test.

2.1.11 Bootstrapping

The climate system including principal constituents — like the atmosphere, the ocean, the hydrosphere, the cryosphere, the lithosphere, and the biosphere — can be regarded as continuously evolving. Starting with a given initial state, the solutions of the equations that govern the dynamics of a highly non-linear system result in a set of long term statistics.

If, on the one hand, all initial states ultimately lead to the same set of statistical properties the system is called *ergodic* or *transitive* (Lorenz, 1964). If,

on the other hand, there are two or more different sets of statistical properties, where some initial states lead to one set, while the other initial states lead to another, the system is called *intransitive*.

The assumption of ergodicity/transitivity is an implicit a-priori selection of almost any description of the climate system using classical statistics. For instance, the definition of 30y mean states which is quite popular in climate research is based on the ergodicity expectation. The intransitivity assumption means that there is only one sample available from the observations regardless of the time series length of the observation. Any natural system including the Earth's climate system is ultimately such an intransitive system because of the time varying and uncontrollable boundary conditions which are not affected by the climate system itself but which change the statistics of the climate state vector (Hense, 2006).

As stated, the climate system is almost completely intransitive at least on the time scales focussed here. The generation of an ensemble simulation with certain ensemble members only differing in their initial states weakens the ergodicity assumption and respects intransitive aspects of the climate system. Hence for these studies ensemble simulations are favoured.

In section 3.2 the initialisation procedure for the different ensemble members of the standalone atmosphere simulations will be introduced. As a matter of fact the CPU time was limited to an extent which only allowed for the creation of five ensemble members. Five realisations are far to few to derive statistical properties of the ensemble runs. An appropriate technique to increase the number of realisations is the bootstrapping procedure (Efron and Tibshirani, 1993).
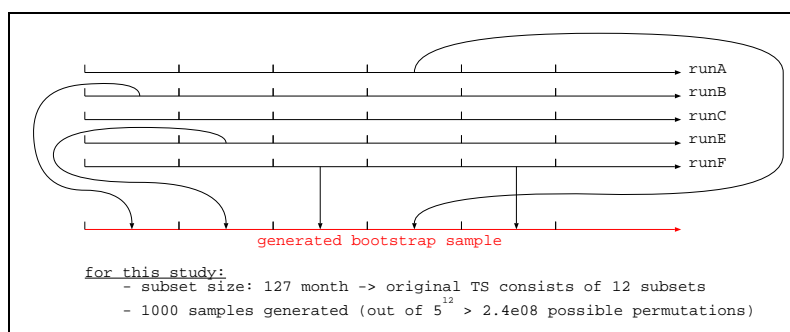

Figure 2.1: Bootstrapping procedure to create numerous bootstrap samples.

Bootstrapping is a statistical method in order to draw new samples from an original sample. It helps to estimate the sampling distribution of an estimator.

Robust non-parametric estimates of standard errors or confidence intervals of population parameters like mean, median or correlation coefficient can be derived. Also conditions for hypothesis tests can be tested by the bootstrapping technique.

The practical implementation for the whole simulation period will be presented. The atmospheric standalone simulation is conducted five times differing in its initial conditions. Fig. 2.1 represents each run as a time line. The nomenclature has assigned letter "D" for the preindustrial control run, and "A", "B", "C", "E", and "F" for the ensemble member runs. The bootstrap samples are generated by randomly taking a subset from one of the five runs for each corresponding subperiod. The size of the subperiod is chosen to be 1/12 of the whole period. Two aspects ought to be respected when setting the size of the subperiod:

- The subset should cover a bigger time span than the variations which will be investigated.

- The subset size should be small enough to allow a number of permutations which is some orders of magnitudes larger than the number of bootstrap samples drawn.

The first point is important because auto-correlations with lags longer than the subperiod size will be destroyed. The second point encounters the pitfall of overconfidence which happens if the chance of drawing identical bootstrap samples becomes to large.

This concept will only be beneficial if estimators of the whole bootstrap samples are derived. Here, a Fourier transformation of the whole bootstrap sample to the frequency domain ensures the regard of this aspect.

2.1.12   Locally Weighted Regression

Parametric methods, such as neural networks and Gaussians mixture models, use training data to fit a certain model. Afterwards, the model is used for predictions while the data are generally discarded. In contrast non-parametric approaches explicitly retain the training data and use it each time a prediction needs to be made. LOcally weighted regrESSion (LOESS) (Cleveland, 1979) [1] is a "non-parametric" method that is built on "classical" methods, like linear and

---

[1]Cleveland's fundamental article has been cited more than 2,000 times

nonlinear least squares regression. It has become popular in fields like "signal detection" or "non-parametric smoothing".

The approach is realised by fitting simple models to localised subsets of the data to build up a function that describes the deterministic part of the variation in the data, point by point. The main advantage of the LOESS method is its flexibility which is achieved by considering only segments of the whole data set. It is not necessary to choose a global prior function of a particular form to fit a model.

The polynomial fit is done by trimming a low order polynomial to given data for every single point in a way that a cost function is minimised. The cost function sums up distance weighted least squares of all data points. This method is computationally expensive compared to "classical" methods.

Only information pertaining to a neighbourhood of the input query is used. Suppose a data point y_i to be composed of a deterministic part $g(x_i)$ and an error ϵ_i, then y_i can be written as

$$y_i = g(x_i) + \epsilon_i. \tag{2.42}$$

The random variable ϵ has mean zero $\overline{\epsilon} = 0$ and constant scale. The smooth function g gives an estimate of $\hat{y}_i = g(x_i)$. A weight function $W(x)$ returns decreasing weights $w_k(x_i)$ as the distance of x_k from x_i increases. The size of the subset used for the estimation procedure depends on the bandwidth parameter f. f ought to be chosen in such a manner that f is as large as possible to minimise variability but respecting the deterministic pattern of the data.

This study applies LOESS filtering to equally spaced time series or power spectra, therefore a fix f delivers a fix number n of data points respected for each local fit. The distance of x_i from x_k is reflected in a distance function $h_k(x_i) \sim \mid x_k - x_i \mid$ which leads to $w_k(x_i) = W(h_i^{-1}(x_k - x_i))$. As proposed in the original article, a tricubic distance function has been applied.

$$
\begin{aligned}
W(h(x)) = & \quad (1 - \mid h \mid^3)^3 & , for \ \mid h \mid < 1 & \qquad (2.43) \\
= & \quad 0 & , for \ \mid h \mid \geq 1 & \qquad (2.44)
\end{aligned}
$$

The distance function $h(x)$ returns $h(x) < 1$, if the data point x_k belongs to the subset, if not, it becomes zero. Fig. 2.2 is emphasising that the weights $W(h)$ decrease quite rapidly as the distance increases.
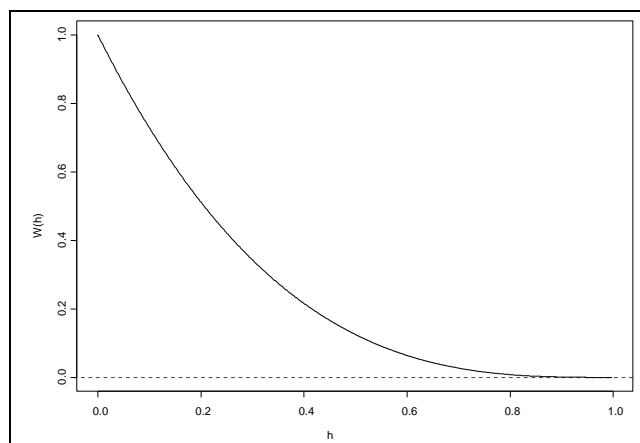
Figure 2.2: Weight function $W(h)$ as proposed by Cleveland (1979).

The cost function J looks as follows:

$$J = \sum_{k=i-(n-1)/2}^{k=i+(n-1)/2} w_k(x_i) \left(y_k - \sum_{l=0}^{l=d} (\beta_l x_k^l) \right)^2 \tag{2.45}$$

The degree of the polynomial d is a prior and mainly set to 1, 2 or 3. Throughout this work a polynomial of the order of two is chosen. Another prior is the bandwidth n which determines the smoothing characteristic. The coefficients β_l represent the polynomial. Demanding $J(x_i) \overset{!}{=} min.$ provides the estimates $\hat{\beta}_l$ and $\hat{y}_i$ respectively.

2.1.13 Discriminant Analysis

The Student's t-test was introduced in section 2.1.10 to test the null hypothesis,

$$H_0 : \mu_X = \mu_Y \ , \tag{2.46}$$

that a pair of univariate random variables $\mathbf{X}$ and $\mathbf{Y}$ have equal means. In general, for all significance levels α the probability of rejecting H_0 converges to 1 as the sample size increases to infinity $n \to \infty$ (Storch and Zwiers, 1999). Thus, paradoxically, small sample sizes result less likely in insignificant differences than larger ones. The discriminant analysis offers a solution to this problem by constructing a test which classifies the cdfs of the random variables. The outlined concept is drawn on the work of von Storch and Zwiers (1988).

Two random variables $\mathbf{X}$ and $\mathbf{Y}$ are *(q, p)-recurrent* if

$$P(\mathbf{Y} > X_q) = p , \tag{2.47}$$

where X_q is the q-th quantile of the random variable $\mathbf{X}$. The term *p-recurrent* is synonymous with (0.5,p)-recurrent.

A realisation z is drawn from either $\mathbf{X}$ or $\mathbf{Y}$. It is not possible to determine from which population z was drawn with absolute certainty, but it is possible, to state probabilities of making an incorrect decision. The decision is made as follows:

- for $z < X_q$ z is drawn from $\mathbf{X}$

- for $z > X_q$ z is drawn from $\mathbf{Y}$

If z is really drawn from $\mathbf{X}$ then $P(z < X_q) = q$ so that the probability of a correct decision is q. If z is really drawn from $\mathbf{Y}$ then $P(z > X_q) = p$ (see Eq. 2.47). Therefore the probabilities of incorrect decisions are $(1-q)$ and $(1-p)$.

The application of the discriminant analysis within this work is to decide whether two samples $\{x_1, x_2, \ldots, x_m\}$ and $\{y_1, y_2, \ldots, y_n\}$ are drawn from different populations. Assume the samples are drawn from $\mathbf{X}$ and $\mathbf{Y}$ which are normally distributed random variables with expectations values μ_X and μ_Y and identical variances σ^2. For $Z_p = F_{\mathcal{N}(0,1)}^{-1}(p)$ being the p-quantile of the standard normal distribution the null hypothesis that $\mathbf{X}$ and $\mathbf{Y}$ are less than p-recurrent and an alternative hypothesis H_A can be formulated.

$$H_0 : \frac{\mu_Y - \mu_X}{\sigma} \quad < \quad 2Z_p \tag{2.48}$$

$$H_A : \frac{\mu_Y - \mu_X}{\sigma} \quad \geq \quad 2Z_p \tag{2.49}$$

If H_0 is valid the standard t-statistic has a non-central Student-t distribution with $n_X + n_Y - 2$ degrees of freedom. The *non-centrality parameter* Δ can be calculated by:

$$\Delta = \frac{2Z_p}{\sqrt{\frac{1}{n_X} + \frac{1}{n_Y}}}. \tag{2.50}$$

The test can be conducted with the usual t-statistic:

$$t = \frac{\overline{\mathbf{Y}} - \overline{\mathbf{X}}}{S_p\sqrt{\frac{1}{n_X} + \frac{1}{n_Y}}} \tag{2.51}$$

For α being the acceptable risk of falsely rejecting H_0, the t-value is compared with the $(1-\alpha)$ percentile of the non-central Student-t distribution $t_{n_X+n_Y-2,\Delta,(1-\alpha)}$ with n_X+n_Y-2 degrees of freedom and non-centrality parameter Δ. The sample variance $S_P^2 = ((m-1)s_x^2 + (n-1)s_y^2)/(m+n-2)$ is calculated from the sample variances s_x^2 and s_y^2 respectively.

For large sample sizes the percentiles will be approximated by

$$t_{n_X+n_Y-2,\Delta,(1-\alpha)} = \Delta + Z_{1-\alpha}. \tag{2.52}$$

2.1.14 Analysis of Variance

<u>AN</u>alysis <u>Of</u> <u>VA</u>riance (ANOVA) is a statistical procedure, in which the observed variance of an indicator variable is partitioned into components due to different explanatory variables/factors (Storch and Zwiers, 1999). The basic concept is to clearly identify the sources of variances and how they sum up to the observed variance of the indicator variable. The initial techniques of the analysis of variance were developed by the statistician and geneticist R. A. Fisher in the 1920s and 1930s, and is sometimes known as Fisher's ANOVA or Fisher's analysis of variance, due to the use of Fisher's F-distribution as part of the test of statistical significance.

A one- and two-way ANOVA based on a 2-factor mixed effects model is used with the ensemble of ECHAM5 simulations (see chapter 5.3). The design of the ANOVA is primarily accorded with the one introduced by Zwiers (1996). The much simpler one-way ANOVA will be handled as a special case of the two-way ANOVA presented in the following.

Two-Way ANOVA

The explanatory variables mentioned in the chapter 2.1.14 can be figured out as characteristic properties of a sample. For instance the results of an opinion poll can be grouped into smaller samples of respondents characterised by the same sex, age, income, educational level etc. Then these characteristics would be explanatory variables, in a sense that they are or are not able to explain an effect on the indicator variable which here is the opinion. The ANOVA simply quantifies the effect of the explanatory variables on the indicator variable in a statistical manner considering randomness as well.

		Factor B				
		1	2	$\ldots$	b	
	1	$\mathbf{X}_{11o}$	$\mathbf{X}_{12o}$	...	$\mathbf{X}_{1bo}$	$\mathbf{X}_{1oo}$
Factor A	2	$\mathbf{X}_{21o}$	$\mathbf{X}_{22o}$	...	$\mathbf{X}_{2bo}$	$\mathbf{X}_{2oo}$
	$\ldots$	$\ldots$	$\ldots$	$\ldots$	$\ldots$	$\ldots$
	a	$\mathbf{X}_{a1o}$	$\mathbf{X}_{a2o}$	...	$\mathbf{X}_{abo}$	$\mathbf{X}_{aoo}$
		$\mathbf{X}_{o1o}$	$\mathbf{X}_{o2o}$	...	$\mathbf{X}_{obo}$	$\mathbf{X}_{ooo}$

Table 2.2: Schematic overview of a two-way ANOVA design.

Before going into mathematical details principal assumptions have to be made:

- The data from which the samples were obtained must be normally distributed. The more complex the ANOVA the less important this claim becomes.

- The samples must be independent of each other.

Through this work sample sizes are constant.

$$
\begin{aligned}
\mathbf{X}_{ijk} &= \mu + \alpha_i + \beta_j + \gamma_{ij} + \epsilon_{ijk} & (2.53) \\
i &= 1, 2, \ldots, a \\
j &= 1, 2, \ldots, b \\
k &= 1, 2, \ldots, c
\end{aligned}
$$

Let factor A have a levels and factor B have b levels in a factorial experiment. The general layout can be written as in Eq. 2.53 with α_i being the effect common to all $j = 1, \ldots, b$ that is identified with i. This effect of factor A is assumed to contain both deterministic and random components $a_i = \alpha_i + \delta_i$ with δ being Gaussian random variable with zero mean. The deviation from the overall mean μ identified by j and common to all $i = 1, \ldots, a$ is denoted by β_j. The mixed effect γ_{ij} and the remaining deviations ϵ_{ijk} are as well assumed to be random, independent, identically distributed, and Gaussian with mean zero. For a more detailed discussion on the background of the assumptions made and possible departures from it within an application to a GCM ensemble please refer to Zwiers (1996).

Table 2.2 points up the configuration of a two-way ANOVA including mixed effects. Each cell contains a sample of equal size k. The "o" denotes the arithmetic mean over the subscript. The means over all $j = 1, \ldots, b$ and $k = 1, \ldots, c$ are summarised in the very right column and can intuitively be regarded as just treated by "Factor A" as the effect of "Factor B" vanishes when averaging. The same happened to the bottom line in the table with the Factors being switched. This configuration enables to partition the total variation of $\mathbf{X}_{ijk}$ into three statistically independent components that isolate the variability associated with factor A / factor B and mixed effect as much as possible. The total sums of squares TSS is the sum of factor A sums of squares SSA, factor B sums of squares SSB and mixed effect sums of squares SSI (2.58).

$$TSS = \sum_{i=1}^{a} \sum_{j=1}^{b} (\mathbf{X}_{ijo} - \mathbf{X}_{ooo})^2 \tag{2.54}$$

$$SSA = b \sum_{i=1}^{a} (\mathbf{X}_{ioo} - \mathbf{X}_{ooo})^2 \tag{2.55}$$

$$SSB = a \sum_{i=1}^{b} (\mathbf{X}_{ojo} - \mathbf{X}_{ooo})^2 \tag{2.56}$$

$$SSI = \sum_{i=1}^{a} \sum_{j=1}^{b} (\mathbf{X}_{ijo} - \mathbf{X}_{ioo} - \mathbf{X}_{ojo} + \mathbf{X}_{ooo})^2 \tag{2.57}$$

$$\Rightarrow TSS = SSA + SSB + SSI \tag{2.58}$$

If the conceptual design has been realised, three hypotheses can be tested by the appropriate F-statistic. Expressing the hypothesis H_A yields:

$$H_{0_A} : \alpha_i = 0, \ \forall i \text{ and } \sigma_\delta^2 = 0 \tag{2.59}$$

The expression is equivalent to the hypothesis that there is no effect of factor A on $\mathbf{X}_{ijk}$. H_A is tested by comparing the F-ratio:

$$F_A = \frac{SSA}{a-1} \bigg/ \frac{SSI}{(a-1)(b-1)} \tag{2.60}$$

with critical values of the F-distribution with (a-1) and (a-1)(b-1) degrees of freedom (DOF). Another diagnostic closely linked to F_A is the proportion of the total variance which results from the effect of factor A. This diagnostic is

sometimes referred to as "explained variance":

$$P_A = \frac{SSA - \frac{SSI}{b-1}}{TSS} \tag{2.61}$$

The testing procedure of factor B, which is implemented as a fixed effect in this model, then is simply done by formulating the null hypothesis H_B:

$$H_{0_B} : \beta_j = 0, \ \forall j \tag{2.62}$$

that there is no effect of factor B on the indicator variable $\mathbf{X}_{ijk}$. The F-ratio and proportion are then calculated analogously to factor A.

$$F_B = \frac{SSB}{b-1} / \frac{SSI}{(a-1)(b-1)} \tag{2.63}$$

with comparison to critical values of the F-distribution with $(b-1)$ and $(a-1)(b-1)$ degrees of freedom (DOF).

$$P_B = \frac{SSB - \frac{SSI}{a-1}}{TSS} \tag{2.64}$$

The third test, which can be performed, treats the "mixed effect". The according null hypothesis that there is no "mixed effect" means that after effects of factor A and B have been taken into account only random variations remain:

$$H_{0_I} : \sigma_\gamma^2 = 0. \tag{2.65}$$

The null hypothesis H_{0_I} is tested by comparing

$$F_I = \frac{SSI}{(a-1)(b-1)} / \mathrm{Var}(\epsilon_{ijk}) \tag{2.66}$$

to values of the reference F-distribution with $(a-1)(b-1)$ and $2ab$ DOF. Zwiers (1996) showed that the test changes when daily data are available or serial correlation occurs in a group (dependent data regarding index k).

One-Way ANOVA

For most applications in meteorology a one-way ANOVA is sufficient. Thinking of an ensemble simulation a one-way ANOVA can analyse which part of the variance is common to all realisations, i.e. can be treated as externally driven, and which part is special to a certain realisation, i.e. can be treated as internally

driven (Storch and Zwiers, 1999). Such an application reduces the model from the previous section (see Eq. 2.53) to a more simple one:

$$\mathbf{X}_{ik} = \mu + \alpha_i + \epsilon_{ik} \tag{2.67}$$

Like for the more complex two-way ANOVA the total sum of squares can be partitioned:

$$TSS = SSA + SSE \tag{2.68}$$

with:

$$TSS = \sum_{i=1}^{a}\sum_{k=1}^{c}(\mathbf{X}_{ik} - \mathbf{X}_{oo})^2 \tag{2.69}$$

$$SSA = c\sum_{i=1}^{a}(\mathbf{X}_{io} - \mathbf{X}_{oo})^2 \tag{2.70}$$

$$SSE = \sum_{i=1}^{a}\sum_{k=1}^{c}(\mathbf{X}_{ik} - \mathbf{X}_{ok})^2. \tag{2.71}$$

Since only one fixed effect is considered the only hypothesis which can be tested is that there is no effect of factor A on $\mathbf{X}_{ik}$:

$$H_{0_A} : \alpha_i = 0, \ \forall i \tag{2.72}$$

A suitable statistic to test H_A might be:

$$F_A = \frac{SSA/(a-1)}{SSE/(a(c-1))} \tag{2.73}$$

against F(a-1,a(c-1)). Storch and Zwiers (1999) derived unbiased estimators for the F-ratio F_A and the explained proportion of variance P_A in order to avoid the problem of overconfidence as in regression analysis. The unbiased estimators are:

$$P_A = \sqrt{\frac{SSA - \frac{a-1}{a(c-1)}SSE}{TSS}} \tag{2.74}$$

$$F_A = \frac{1 + \frac{a(c-1)}{a-1}P_A^2}{1 - P_A^2}. \tag{2.75}$$

2.2 Frequency Analysis

2.2.1 Fourier Transformation

Periodic processes are important and common in nature or in engineering. Many examples can be found such as pulsation, planetary motion, audio frequency, colours etc. A mathematical description for these processes was already provided by Jean Baptiste Joseph Fourier (1768-1830). He expressed his basic concept in one sentence saying: "*Every periodic function can be decomposed into a sum of sine and cosine*". A broad spectrum of applications was facilitated in the 1960s when computers were able to perform Fourier analyses. Particularly the Fast Fourier Transform (FFT) a sophisticated — or more precisely spoken an efficient — algorithm to compute the Discrete Fourier Transform (DFT) is of importance to a wide variety of applications, from digital signal processing and solving partial differential equations to algorithms for quick multiplication of large integers. Nowadays many compressing file formats use the algorithm (e.g. MP3 audio files, MPEG video files or JPEG picture files). This method and the general idea of an FFT was popularised by a publication of Cooley and Tukey (1965).

The Fourier transform is a specific form of the Fourier analysis. It transforms one function into another, which is called as representation in the frequency domain of the original function (where the original function is often a function in the time domain). The denotation "Fourier transform" has two meanings. On the one hand it describes the frequency domain representation of a function. On the other hand it can refer to the process that transforms one function into another:

$$F(\nu) = \int_{-\infty}^{\infty} f(t)e^{-2\pi i\nu t}dt \tag{2.76}$$

The Fourier transform is the function $F(\nu)$ in Eq. 2.76 and is invertible, with the inverse Fourier transform

$$f(t) = \int_{-\infty}^{\infty} F(\nu)e^{2\pi i\nu t}d\nu. \tag{2.77}$$

In general, $F(\nu)$ is complex even for real $f(t)$. The Fourier transform exists, if $f(t)$ complies with the Dirichlet conditions on every finite interval. The Dirichlet conditions demands that on each of the finite intervals $f(t)$ is monotonous and continuous. For t_0 being a point of discontinuity of $f(t)$, the limit values $f(t_0 + 0)$ and $f(t_0 - 0)$ do exist (Bronstein and Semendjajew, 1991).

Now consider the general case of a discrete function, $f(t) \to f(t_k)$ by letting $f_k \equiv f(t_k)$, where $t_k \equiv k\Delta t$, with $k = 0, 1, \ldots, N-1$. Applying the Fourier transform to the discrete codomain gives the DFT:

$$\hat{F}_n = \sum_{k=0}^{N-1} f_k e^{-2\pi i n k/N}, \tag{2.78}$$

where the inverse is:

$$\hat{f}_k = \frac{1}{N} \sum_{k=0}^{N-1} F_n e^{-2\pi i n k/N} \tag{2.79}$$

Note that both series of coefficients $f_0, \ldots, f_N$ and $F_0, \ldots, F_N$ are complex numbers. DFTs are extremely useful because they reveal periodicities in input data as well as the relative strengths of any periodic components. The Euler decomposition accounts for a representation of real numbers, it transforms the complex exponential function into trigonometric parts:

$$e^{ix} = cos(x) + i\, sin(x) \tag{2.80}$$

2.2.2 The Power Spectrum

The energy spectral density describes how the energy (or variance) of a signal or a time series is distributed with frequency. If $f(t)$ is a finite-energy (square integrable) signal like in the previous chapter, the spectral density $\Phi(\nu(n))$ of the signal is the square of the magnitude of the continuous Fourier transform of the signal. For the discrete case a close to unbiased estimator of the spectral density is:

$$\hat{\Phi}(\nu(n)) = |\sum_{k=0}^{N-1} f_k e^{-2\pi i n k/N}|^2 = F_n F_n^* \tag{2.81}$$

However, unbiasedness is only one attribute of a good estimator. Consistency is also a very desirable attribute. Unfortunately, the estimator (Eq. 2.81) lacks this property. An estimator is *consistent* if its *mean squared error* (MSE) (see Eq. 2.83) goes to zero with increasing sample size.

$$\lim_{n \to \infty} MSE(\hat{\alpha}; \alpha) = 0 \tag{2.82}$$

$$MSE(\hat{\alpha}; \alpha) = \mathrm{E}\left((\hat{\alpha} - \alpha)^2\right) \tag{2.83}$$

The variance of the estimator $\hat{\Phi}(\nu)$ does not go to zero with increasing sample size in any case. For instance, for a white noise process it can be shown that there is a limiting value for $\lim_{n \to \infty} MSE(\hat{\alpha}; \alpha)$ different from zero (Jenkins and

Watts, 1968). In such a case doubling the sample size does not result in a smoother estimate of the spectrum, it results in almost independent spectral estimates at twice as many frequencies. That's why it is more beneficial to derive spectral estimates from several frequencies lying in a certain window. In this work spectral estimates will be derived from several realisations of the estimate or from a LOESS smoother. Both methods deal with the problem of inconsistent estimates.

2.2.3 Wavelet Transformation

In the previous two sections a skillful tool to transform data from time to spectral domain was presented. The power spectrum represents the mean variability for a specific frequency over the whole time span meaning that it is appropriate for stationary processes. Geophysical time series are often based on non-stationary processes which are not comprehended in the Fourier transform. Non-stationary processes are much better represented in time-frequency domain. The wavelet transformation provides a mapping procedure to this domain. Prevalently a certain spectral component occurring at any instant can be of particular interest. In these cases it is beneficial to know the time intervals in which these spectral components occur. The wavelet transform is capable of procuring the time and frequency information simultaneously, hence giving a time-frequency representation of the signal. The wavelet power spectrum consists of an additional dimension giving energy in dependence of time and frequency $E(\nu, t)$ instead of just the time information $E(t)$ as for the simple power spectrum.

The detailed description of the wavelet analysis follows the work of Torrence and Compo (1998) who performed a wavelet analysis on the ENSO3.4 index. The wavelet transform (WT) can be used to analyse time series that contain non-stationary power at many different frequencies. Let x_k be a time series with equal time spacing Δt and time steps $k = 0, \ldots, N - 1$. Now assume that one has a wavelet function $\Psi_0(\eta)$ depending on a nondimensional time parameter η. To pursue the requested goals the wavelet function must have zero mean and be localised in both time and frequency domain. For this work the Morlet wavelet was used that fulfils these demands. It consists of a plain wave which is modulated by a Gaussian:

$$\Psi_0(\eta) = \pi^{-\frac{1}{4}} e^{i\omega_0 \eta} e^{-\frac{\eta^2}{2}} \tag{2.84}$$

The nondimensional frequency ω_0 is set to six in the following. An estimator of the continuous wavelet transform of a discrete sequence x_k is given as the

convolution of x_n with a scaled and translated version of $\Psi_0(\eta)$:

$$\hat{W}_k(s) = \sum_{k'=0}^{N-1} x'_k \Psi^* \left(\frac{(k'-k)\Delta t}{s} \right) \qquad (2.85)$$

The *-sign indicates the complex conjugate. A graph showing the amplitude and scale can be achieved by varying the wavelet scale s and translating along the localised time index k. The wavelet power spectra then reflects per definition $(\hat{W}_k(s))^2$.

For the purpose of comparability the wavelet transforms (see Eq. 2.85) are normalised for each scale s in order to have unit energy:

$$\Psi \left(\frac{(k'-k)\Delta t}{s} \right) = \left(\frac{\Delta t}{s} \right)^{1/2} \Psi_0 \left(\frac{(k'-k)\Delta t}{s} \right) \qquad (2.86)$$

The basic Morlet wavelet Ψ_0 is normalised to have unit energy like this.

It can be shown that the mean wavelet power spectrum over the whole time span is well estimated by the Fourier power spectrum (Torrence and Compo, 1998; Stuck, 2002). This behaviour is used for the purpose of significance testing. The corresponding null hypothesis H_0 can be formulated as follows:

$$H_0 : |W_k(s)|^2 = P_n \qquad (2.87)$$

As for the Fourier power spectrum a background lag-1 autoregressive Markovian process is assumed. The discretised and normalised Fourier spectrum of such a process uniquely depends on the first coefficient of the auto-correlation function α_1 and theoretically is:

$$P_n = \frac{1 - \alpha_1}{1 + \alpha_1^2 - 2\alpha_1 cos(2\pi n/T)} \qquad (2.88)$$

The number of the Fourier frequency index is indicated by $n = 0, \ldots, T/2$ with T being the number of all time steps. The Fourier spectrum of a Gaussian random variable is a Gaussian as well which means that the complex Fourier spectrum is χ_2^2-distributed with two degrees of freedom. The assumption, that the wavelet spectra are χ_2^2-distributed as well leads to the following relation:

$$\frac{|W_k(s)|^2}{\sigma^2} > \frac{1}{DOF} P_n \chi_{DOF,\alpha}^2 \qquad (2.89)$$

The distribution is calculated for every Fourier frequency index n. The degrees

of freedom are two in case of the complex Morlet wavelet function $DOF_{MW} = 2$. The null hypothesis (2.87) is rejected if relation 2.89 is valid.

Chapter 3

Atmospheric Standalone Simulations

General circulation models are able to simulate mass movements and mass concentrations on a global scale in a realistic way. Due to enormous mass displacements and motions relative to the rotating Earth the atmosphere and oceanic hydrosphere have an important impact on ERPs. Simulations of an atmospheric standalone GCM have been conducted for this work. This work was part of a joint project from oceanography, geodesy and meteorology. The oceanographical group from University Hamburg has set up a coupled atmosphere-ocean climate model to explicitly investigate load deformation, rotational deformation, tidal deformation and effects on ERPs. To realise these objectives a key focus was on the coupled model and the implementation of the tidal potential which is not part of standard coupled models.

To obtain more precise insights of the angular momentum and moment of inertia fluctuations, the additional atmospheric standalone runs have been carried out. The coupled and the standalone runs were driven by the same solar variability and greenhouse gas concentrations. The standalone run offers the possibility to clearly distinguish between oceanic and atmospheric effects as both subsystems are not directly coupled. As the standalone runs are additionally driven by observed <u>S</u>ea <u>S</u>urface <u>T</u>emperatures (SSTs) and <u>S</u>ea <u>I</u>ce <u>C</u>oncentrations (SICs) these runs can be regarded as "perfect ocean" runs. A fictitious example points up the benefits of an additional standalone run. Let X be an atmospheric variable describing a parameter of Earth rotation. X is independently deduced from both - the coupled model's and standalone model's output. Let $X_{coupled}$ have a significantly higher (or lower) variability than $X_{standalone}$. Besides model errors there only exists one possible source of this "extra variability". It is the

coupling procedure itself which possibly adds additional variance to atmospheric variables (Friederichs and Hense, 1999). Therefore in this research both versions are comparatively used in chapter 6.

3.1   ECHAM5

This work concentrates on the ability of global GCMs to reproduce global atmospheric angular momentum and global atmospheric moment of inertia variations associated with changes in the Earth's rotation. The version of the atmospheric GCM in the coupled and standalone model is ECHAM5.3.02 (Röckner et al., 2003). The ECHAM model chain was originally derived from the ECMWF (Simons et al., 1989) numerical weather prediction model and further developed at the Max Planck Institute for Meteorology (MPI-M) in HAMburg. In 2003 ECHAM5 displaced ECHAM4 as current atmospheric GCM. ECHAM5's dynamic core calculates the following prognostic variables:

- $\xi = (\nabla \times \vec{v})_r$ - vorticity

- $div(\vec{v}) = \nabla \cdot \vec{v}$ - divergence

- $ln(p_{surf})$ - logarithm of surface pressure

- T - temperature

- q_i - mixing ratios of the different water species

Within ECHAM5 the prognostic equations for temperature, surface pressure, divergence and vorticity are represented in the horizontal by a truncated series of spherical harmonics; for the water components (vapour, liquid, solid) a flux form semi-Lagrangian scheme (Lin and Rood, 1996) is applied on a Gaussian grid (Mesinger and Arakawa, 1976).

The basic prognostic equations are derived from fundamental physical laws - the continuity equation (Eq. 3.1) represents mass balance for water and dry air (with density ρ and wind vector $\vec{v}$), the Navier-Stokes equation (with pressure p, gravitational potential Φ, uniform angular velocity of the Earth $\vec{\Omega}$ and friction force $\vec{F_R}$) momentum balance (Eq. 3.2) and the first law of thermodynamics (with specific heat at constant pressure c_p, heating due to radiation, phase change, friction Q_R, Q_L, Q_F and specific enthalpies h_k) energy balance (Eq. 3.3).

$$\frac{\partial \rho}{\partial t} + (\nabla(\rho\vec{v})) = 0 \tag{3.1}$$

$$\frac{d\vec{v}}{dt} = -\frac{1}{\rho}\nabla p - \nabla\Phi - 2(\vec{\Omega}\times\vec{v}) + \vec{F_R} \tag{3.2}$$

$$c_p\frac{dT}{dt} = \frac{1}{\rho}\frac{dp}{dt} + Q_R + Q_L + Q_F - \sum_k h_k\frac{\dot{m}_{ki}}{m} \tag{3.3}$$

$$p_d V_{d+v} = m_d R_d T \tag{3.4}$$

$$p_v V_{d+v} = m_v R_v T \tag{3.5}$$

$$\Rightarrow p = \frac{m_d R_d T + m_v R_v T}{V_{d+v}} \tag{3.6}$$

Equation 3.4 and 3.5 are the equation of state for dry air and water vapour respectively with the specific gas constants R_d and R_v. After considering p_d and p_v as partial pressures and applying Dalton's law (Eq. 3.6) is formed. By making several assumptions and introducing the combined equation of state these equations form a set of coupled partial differential equations. The major assumptions made are:

- dry air and water vapour are ideal gases

- hydrostatic approximation is valid: $\frac{\partial p}{\partial z} = -\rho g$

- mass flux convection scheme for sub-grid scale cloud ensemble is applicable

The prognostic variables divergence $div(\vec{v}) = \nabla \cdot \vec{v}$ and vorticity $\xi = (\nabla \times \vec{v})_r$ are obtained from the Navier-Stokes equation, temperature T from the first law of thermodynamics and surface pressure p_{surf} from the continuity equation by making the hydrostatic approximation. The equations to calculate the mixing ratios for the different water species q_i can be directly derived from the specific equation of state and the continuity equation.

As mentioned, the prognostic equations include all water phases (vapour, liquid, ice). The implementation of cloud microphysics is adopted from ECHAM4 (Roeckner et al., 1996). The microphysics scheme includes phase changes between water components and precipitation processes (autoconversion, accretion, aggregation). Evaporation/sublimation of rain/snow and melting of snow are considered as well as sedimentation of cloud ice. Further information regarding this topic can be gathered from a paper published by Lohmann and Roeckner

(1996).

The convection scheme within ECHAM5 is based on steady state equations for mass, heat, moisture, cloud water and momentum for an ensemble of updrafts and downdrafts including turbulent and organised entrainment and detrainment. A mass flux scheme is realised for shallow, mid-level and deep convection following Tiedtke (1989) with modifications for deep convection according to Nordeng (1994). Cloud water detrainment — mainly in the upper part of the convective updrafts — is used as source term in the stratiform cloud water equations. In case of deep convection, an adjustment-type closure is applied with convective activity expressed in terms of Convective Available Potential Energy (CAPE).

The shortwave radiation scheme according to Fouquart and Bonnel (1980) makes use of the Eddington approximation for the integration over zenith and azimuth angles and the delta-Eddington approximation for the reflectivity of a layer. It includes absorption by water vapour, ozone, and well-mixed gases as well as Rayleigh scattering. The scheme handles four spectral bands, one for visible+ultraviolet (UV) range, and three for the near infrared. Single scattering properties for clouds are calculated on the basis of Mie's idealised size distributions for cloud droplets and ice crystals.

The longwave Rapid and accurate Radiative Transfer Model (RRTM) scheme is based on the correlated-k method (Mlawer et al., 1997). This scheme calculates the longwave radiative transfer in ECHAM5 by using derived absorption coefficients from a line-by-line water vapour continuum model developed by Clough et al. (1989). 16 spectral bands are calculated separately. Absorption by water vapour, ozone and well-mixed gases is considered as well as for CO_2, O_3, CH_4, N_2O, CFC-11, CFC-12, and aerosols.

Many subgrid processes are parameterised. For instance eddy viscosity and diffusivity are parameterised in terms of turbulent kinetic energy and length scales involving the mixing length and stability functions for momentum and heat (Brinkop and Roeckner, 1995). For the concerns of this work another parameterisation is fundamental. The gravity wave drag scheme by Lott and Miller (1997) takes into account two main interactions between the atmospheric flow and subgrid-scale orography. These are:

- momentum transfer from the Earth to the atmosphere accomplished by orographic gravity waves and

- the drag exerted by the subgrid scale mountains when the air flow is blocked at low levels.

3.2 Standalone Atmosphere 20th Century 20C Simulation

The standalone simulations cover the 1880 to 2006 period. The model used is ECHAM5.3.02 (Röckner et al., 2003) in its standard troposphere version. An ensemble of five runs has been created by disturbing the initial conditions. The latter were extracted from a short preindustrial control run with five-year intervals lasting from 1855 to 1880 (see Fig. 3.1).
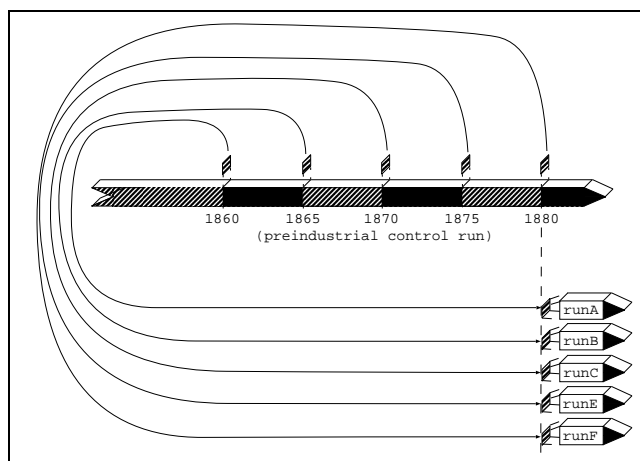

Figure 3.1: Schematic overview of the initialisation procedure.

To obtain realistic states of the atmosphere a broad set of forcing factors was used. It includes greenhouse gas concentrations, an aerosol climatology (Tanre et al., 1984) including volcanic background aerosols, solar variability (Fröhlich and Lean, 1998) and sea surface temperature data as well as sea ice concentration data from the Hadley Centre's reconstruction (Rayner et al., 2006).
The aerosol climatology is a three dimensional field depending on time. In the model both the direct (radiation) and first indirect effect (condensation nucleus) are accounted for (Kristjánsson et al., 2005). Volcanic aerosols have a fixed spatial distribution.

The spatial resolution of the model in this study is T63 in the horizontal and 31 layers in the vertical with the 10 hPa level defining the top of the model atmosphere. In comparison the corresponding grid of a T21 resolution is not able to
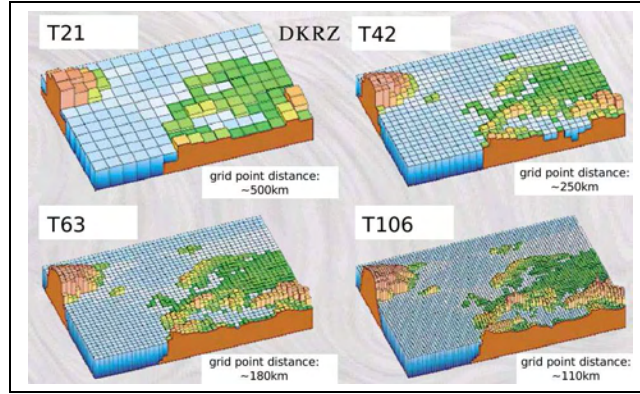
Figure 3.2: Schematic illustration of land sea distribution and orography (exaggerated) for different grid resolutions in ECHAM5 (DKRZ).

constitute Iceland, Svalbard, Italy or the British Isles (see Fig. 3.2). Mountains are flattened due to coarse resolution. A T63 resolution represents a global grid consisting of 192x96 grid points. The distance between two neighbouring grid points is $\sim 1.875°$.

The time step is $\Delta t = 20min.$. The model output is stored every six model hours and contains all necessary informations to derive all variables of the ECHAM5 GCM.

3.2.1 The Horizontal Representation

The representation of atmospheric flow fields by means of spherical functions dates back to Haurwitz (1940).

As stated, basic prognostic variables of the model are ξ, $div(\vec{v})$, $ln(p_{surf})$, T, and q_i. While q_i are represented on a global grid, the other variables as well as the orography/surface geopotential (ϕ_{surf}) are represented as a truncated series of spherical harmonics X_n^m in the horizontal with $\kappa = cos(\varphi)$:

$$X(\lambda, \kappa, \eta, t) = \sum_{m=-M}^{M} \sum_{n=m}^{N(M)} X_n^m(\eta, t) P_n^m(\kappa) e^{im\lambda} \qquad (3.7)$$

The X stands for any variable, m is the zonal wave number and n the meridional

index. The P_n^m are the *Associated Legendre functions of the first kind*, $\forall \; (m \geq 0)$:

$$P_n^m(\kappa) \;=\; \sqrt{(2n+1)\frac{(n-m)!}{(n+m)!}}\frac{1}{2^n n!}(1-\kappa^2)^{m/2}\frac{d^{(n+m)}}{d\kappa^{(n+m)}}(\kappa^2+1) \;, \quad (3.8)$$

$$P_n^{-m}(\kappa) \;=\; P_n^m(\kappa) \;, \tag{3.9}$$

$$\delta_{ns} \;=\; \frac{1}{2}\int_{-1}^{1} P_n^m(\kappa)P_s^m(\kappa)d\kappa \;. \tag{3.10}$$

The *Kronecker delta function* δ_{ns} returns $\delta_{ns} = 1$, $\forall \; (n = s)$ and $\delta_{ns} = 0$, $\forall \; (n \neq s)$. The complex valued spectral coefficients X_n^m of the field are calculated by

$$X_n^m(\eta,t) = \frac{1}{4\pi}\int_{-1}^{1}\int_{0}^{2\pi} X(\lambda,\kappa,\eta,t)P_n^m(\kappa)e^{-im\lambda} \; d\lambda d\kappa \tag{3.11}$$

The Fourier coefficients X_m of the discrete variable X along a certain latitude with zonal wave number m then reduce to (compare 2.78 and 3.7):

$$X_m(\kappa,\eta,t) = \sum_{n=m}^{N(m)} X_n^m(\eta,t)P_n^m(\kappa) \;. \tag{3.12}$$

The summation limit $N(m)$ determines the *truncation* of the Fourier series, it is a measure for the spectral resolution of a model. The standard truncations used in ECHAM5 are at wave numbers 21, 31, 42, 63, 85, 106, or 159. The spectral resolution of the model is then denoted by the term T21, T31, T42 ... .

At this point it is referred to literature. The concept of spherical harmonics is described in more detail in textbooks about dynamical modelling (e.g. Krishnamurti et al., 1988; Zdunkowski and Bott, 2003). ECHAM5 specific issues and the dynamical core of the model represented in spherical harmonics can be found in the model description (Röckner et al., 2003).

3.2.2   The Hybrid Vertical Representation

The ECHAM5 model uses an orography-following vertical coordinate. The lower boundary strongly effects the dynamic flow of the lowest levels in the model. Although it is possible to state the lower boundary conditions in the presence of orography by adapting the orthogonal Cartesian system, the formulation of simple flow patterns becomes rather unwieldy. It is far superior to handle the

orography by replacing the Cartesian vertical coordinate z with a more sophisticated vertical coordinate η. η is defined in such a manner that the model levels are affected by the orography (Zdunkowski and Bott, 2003), as shown on the schematic Figure 3.3 below.
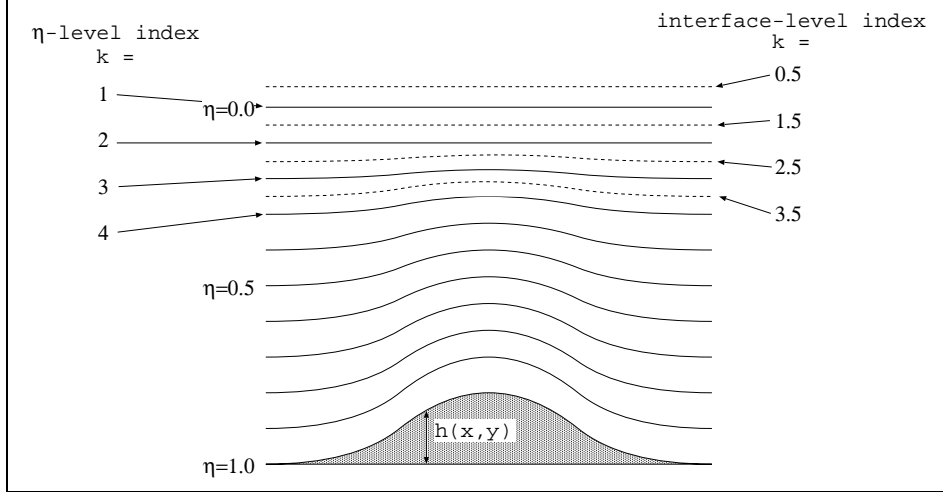

Figure 3.3: Schematic illustration of η and interface levels.

The relation between the vertical coordinate $p = p(\lambda, \varphi, z)$ and the orography-following vertical coordinate $\eta = \eta(\lambda, \varphi, p(z), p_{surf}(\lambda, \varphi))$ is given by the definition of η (see Eq. 3.13 to 3.15).

$$p_{k+1/2} = a_{k+1/2} + b_{k+1/2}p_{surf} \tag{3.13}$$

$$p_k = \frac{1}{2}(p_{k+1/2} + p_{k-1/2}) \tag{3.14}$$

$$\eta_{k+1/2} = a_{k+1/2}p_0 + b_{k+1/2} \tag{3.15}$$

The explicit relationship between p and p_{surf} defined for model half levels implicitly determines a vertical coordinate η. As Eq. 3.14 denotes η-levels are exactly situated between the two neighbouring interface levels (Simmons and Burridge, 1981). The index k denotes the number of the level starting from the top $k = 1$ to the lowest level $k = k_{max}$. The reference sea-level pressure p_0 is used for the definition of η, it is defined by $p_0 = 101325 Pa$. a_k and b_k are fixed parameters defining the position of the interface levels - and therefore also hybrid levels - depending on the surface pressure $p_{surf} = p_{surf}(x, y, t)$. Fortunately the horizontal winds $\vec{v}_{horizontal} = \vec{v}_{horizontal}(\lambda, \varphi, t)$ are parallel to pressure planes that's why calculation of AAM becomes straightforward. The fix values for a_k and b_k in a 31 layer setting within ECHAM5 and in 19 layer setting within

ECHAM4 can be found in Appendix E.

3.2.3 Preparation of SST and SIC Data

To avoid a systematic underestimation of variance when linearly interpolating from monthly means which is the temporal resolution of the Hadley Centre's reconstruction to daily values - as the model expects as input - a filter has been applied to the SST and SIC data (Taylor et al., 2000). Fig. 3.4 is a fictitious illustration of the Taylor filter applied to monthly mean SST data for a Northern Hemisphere grid point. It is indicated that variance is added to the data to face the problem of underestimation, the filtered SSTs are also called "pseudo SSTs". When calculating monthly mean values from the daily values gained from linear interpolation of "pseudo SSTs" one would reobtain the original Hadley Centre values. A boundary condition of the filter is the conservation of monthly mean values. Thus the method of applying the filter to the data is far more superior instead of directly interpolating the Hadley Centre's reconstructions.
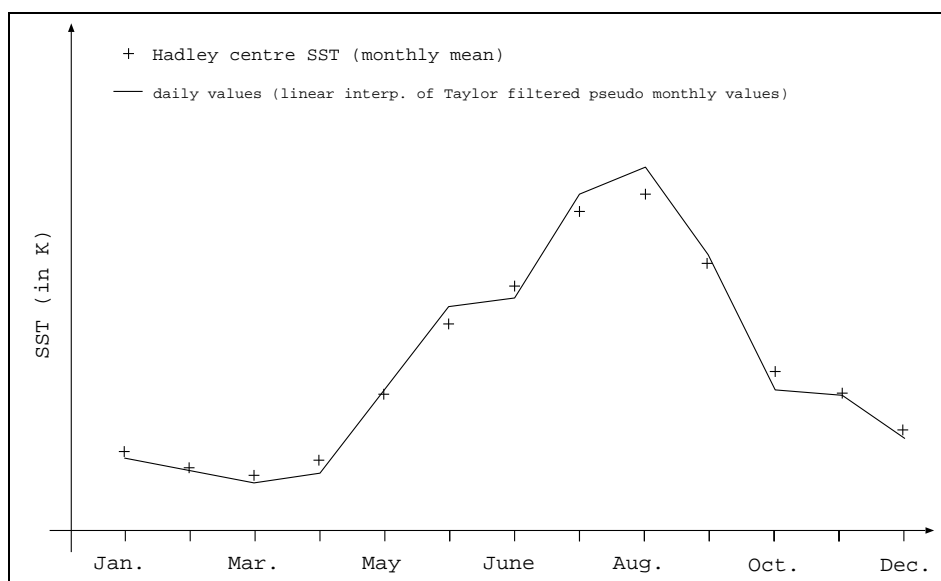

Figure 3.4: Schematic annual cycle of a Northern Hemisphere grid point.

Fig. 3.5 shows the difference/correction between "pseudo SSTs" and the original Hadley Centre data for one timestep. Regions with high temporal variance generate the highest magnitudes in difference - namely Northwest Atlantic and Northwest Pacific as well as regions just beside the ice border.

March is frequently the coldest month for many sites of the Northern Hemisphere. As the second order derivative therefore tends to be positive in March for the Northern Hemisphere and negative for the Southern Hemisphere there is a dependence on latitude concerning the algebraic sign of the correction. In most areas the correction is below $0.2K$.
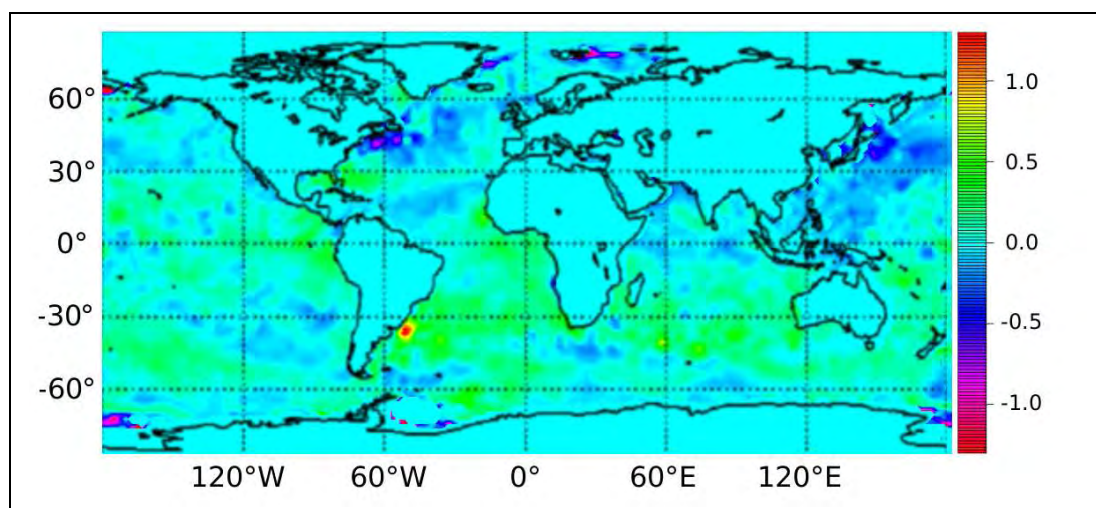

Figure 3.5: Top: difference between Taylor filtered "pseudo SSTs" and Hadley Centre data for March 2003 (in K)

The map in Fig. 3.5 displays a strong positive correction in the Southwest Atlantic near the Uruguayan coast.

3.3 Results

In this chapter the model output of the ECHAM5 ensemble simulation will be analysed. This work is focused on the angular momentum budget of the atmospheric GCM, anyhow other meteorological parameters within the model's output should have "realistic" values. "Unrealistic" states in global temperature or pressure distribution would induce unrealistic AAMs implying that the simulations are useless for the purpose of this study.

Strong departures from observed temperature would be a good indicator of inconsistencies in the energy budget as temperature is directly linked to energy by the first law of thermodynamics describing energy balance. The global mean 2m temperature over land is compared to observed or reconstructed values from the Climate Research Unit (CRU) (Jones et al., 1999; Rayner et al., 2003) (Fig. 3.6). Over sea a large amount of the variance can be explained by the

underlying observed SST which is prescribed as boundary condition. Therefore, a good agreement of observed and simulated values for these grid points is not necessarily obtained due to a good model skill. Thus it is superior to compare land data for validation purpose.

Seasonal variations were removed by a LOESS filter. The agreement between the ensemble mean and the observed global 2m temperature anomaly time series is very reasonable. Although the inter-quantile range (IQR) (blue band) is fairly small and rarely greater than 0.1 K which implies a high model certainty, the observed temperatures lie within the IQR for most of the time. High frequency fluctuations are well captured, this hints at a good SST excitation as the SST forcing is the most effective external driver to induce variability on annual and interannual time scales. Low frequent patterns also agree well with solar and greenhouse gas forcing as main external drivers. The current warming which started in the 1970s matches the observation in time and amplitude. Since 2000 to present the temperature anomaly of the ECHAM simulation is mostly lower than that of the CRU.
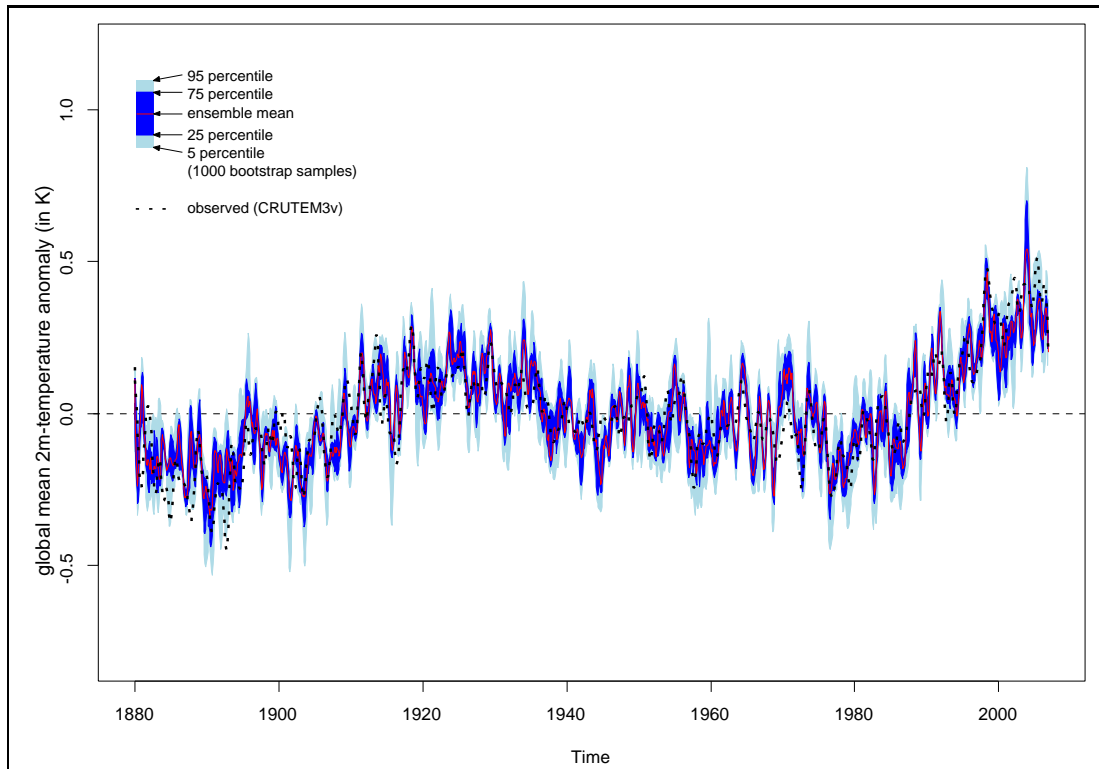

Figure 3.6: Simulated ECHAM5 ensemble mean (blue shadings, red line) and observed global land 2m temperature anomalies (dashed black line) - 12 month bandwidth LOESS smoothed.

When investigating the spatial distribution of certain parameters, reanalysis data form the only reference being available for several decades. Mean Sea Level Pressure (MSLP) and 2m temperature are known to have a rather good quality within the ERA40 data set and are used for a brief comparative analysis.

As reference epoch the entire ERA40 period from 1958 to 2001 is respected. Means over all Januaries and Julies are calculated as well as standard deviations for every grid point and compared to the arithmetic mean of all ensemble members (the ensemble mean) and the mean standard deviation. The reanalysis data is available with a T159 spectral resolution corresponding to a 480x240 gaussian grid. The grid resolution is finer by factor 2.5 resulting in a number of grid points which is 6.25 times higher. For comparability reasons the ERA40 data has been interpolated to the ECHAM5 grid.
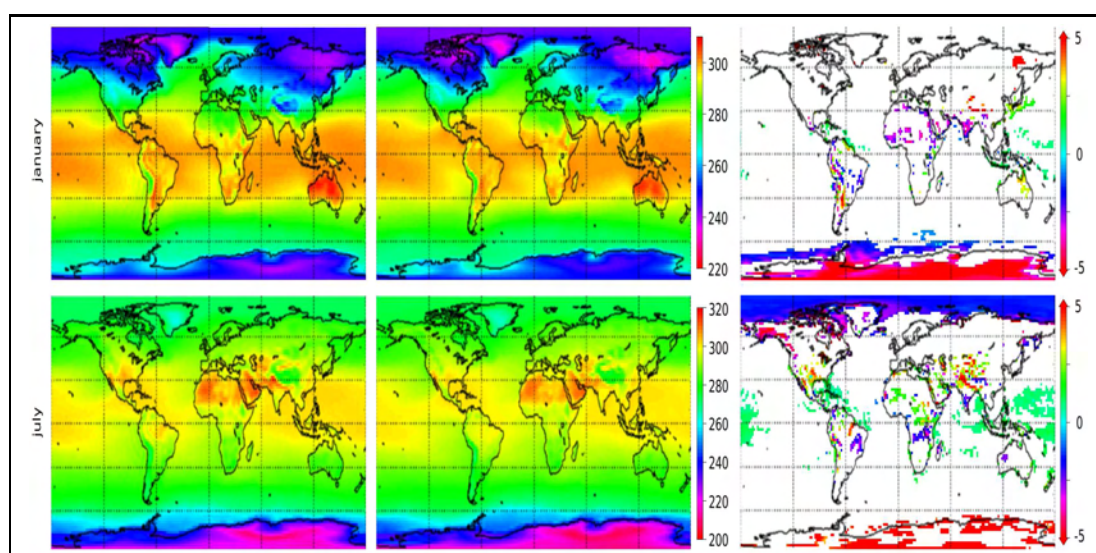

Figure 3.7: Top row: January mean 2m temperature 1958 to 2001 (in K); bottom row: July mean 2m temperature 1958 to 2001 (in K),
first column: ECHAM5 ensemble mean; second column: ERA40 and third column: difference between ECHAM5 ensemble mean and ERA40 (ECHAM5-ERA40) tested by a discriminant analysis on five percent significance level (unsignificant differences are whitened).

The third column in Fig. 3.7 shows the difference between the ECHAM5 ensemble mean and the ERA40 reanalysis data. In general the number of grid points showing a significant difference in January mean temperature is small. In July some grid points over sea in the inner tropics are overestimated significantly by ECHAM5. Of course over sea the underlying SST forcing determines the 2m

temperature significantly. Therefore a high consonance is expected. Over land
the situation is diverse. Systematic significant differences are present in very high
latitudes during summer, particularly over sea ice covered regions ECHAM5 un-
derestimates temperature. Perhaps the snow/ice albedo is set too high within
the model. Over Antarctica the difference exceeds five Kelvin at some locations.
During winter ECHAM5 tends to overestimation of the 2m temperature in these
regions.

Generally the global patterns are consistent with each other. For instance
the East Siberian cold pole or the heat of the Australian outback are well pro-
nounced for January. A west-east temperature gradient over midlatitude winter
continents is as well implied in the model pointing at a realistic general circula-
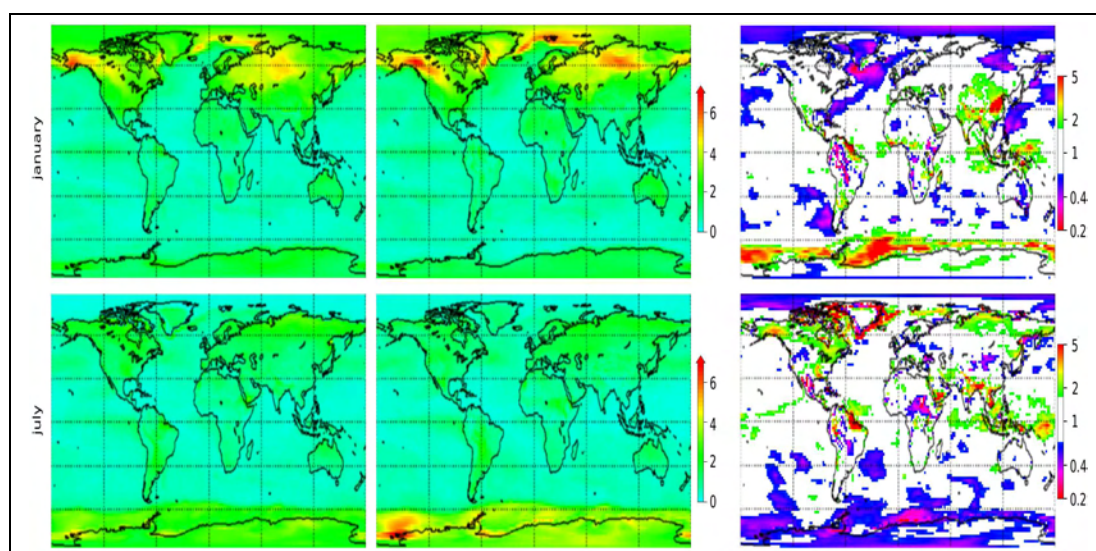tion.

Figure 3.8: Top row: January standard deviation of 2m temperature 1958 to
2001 (in K); bottom row: July standard deviation of 2m temperature 1958 to
2001 (in K),
first column: ECHAM5 (mean over all members); second column: ERA40 and
third column: difference between ECHAM5 and ERA40 (ECHAM5-ERA40)
tested by F-test on five percent significance level (unsignificant differences are
whitened).

A closer look at the temperature variability is obtained by the standard de-
viation of the January and July temperature for every grid point (Fig. 3.8). As
the variability of the ensemble mean is reduced by averaging the mean stan-
dard deviation of all ensemble members is displayed. The variability of ocean

grid points is comparatively small in ECHAM5 and ERA40. The highest amplitudes in standard deviations are found at winterly continental areas and along the sea ice border. The physical background can be explained by sensible heat fluxes. Over the open sea the sensible heat flux from the surface to the atmosphere is very strong in arctic winter and traps the 2m temperature close to the freezing point. Whereas over sea ice the sensitive heat flux is reduced dramatically and temperatures drop well below zero. Therefore the standard deviation of sea concentrations and the one of 2m temperature correlate well in this region.

The differences (third column of Fig. 3.8) between ECHAM5 and ERA40 standard deviations are small for the majority of grid points. Preferentially over sea a significant systematic underestimation for winter and overestimation for summer at high latitudes can be seen. Nevertheless the variability of the ERA40 data is very well captured by the model resulting in small differences of the standard deviation for most of the sites.
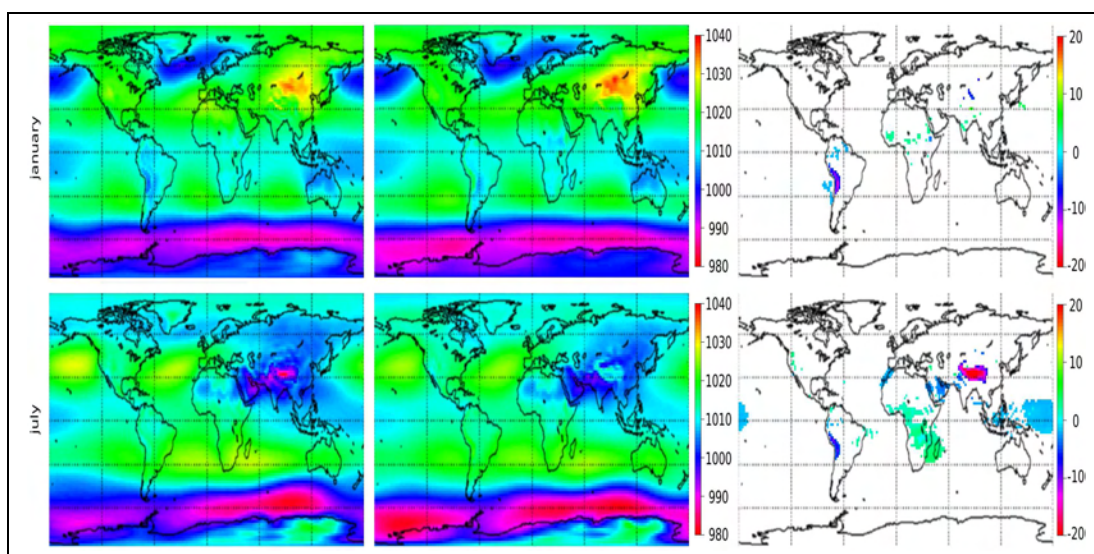

Figure 3.9: Top row: January mean MSLP 1958 to 2001 (in hPa); bottom row: July mean MSLP 1958 to 2001 (in hPa),
first column: ECHAM5 ensemble mean; second column: ERA40 and third column: difference between ECHAM5 ensemble mean and ERA40 (ECHAM5-ERA40) tested by a discriminant analysis on five percent significance level (unsignificant differences are whitened).

Typical pressure patterns are well comprehended within the simulation (see Fig. 3.9). The Icelandic winter low or the Azores high are two prominent examples. The Southern Hemisphere subpolar low pressure belt is very intense in
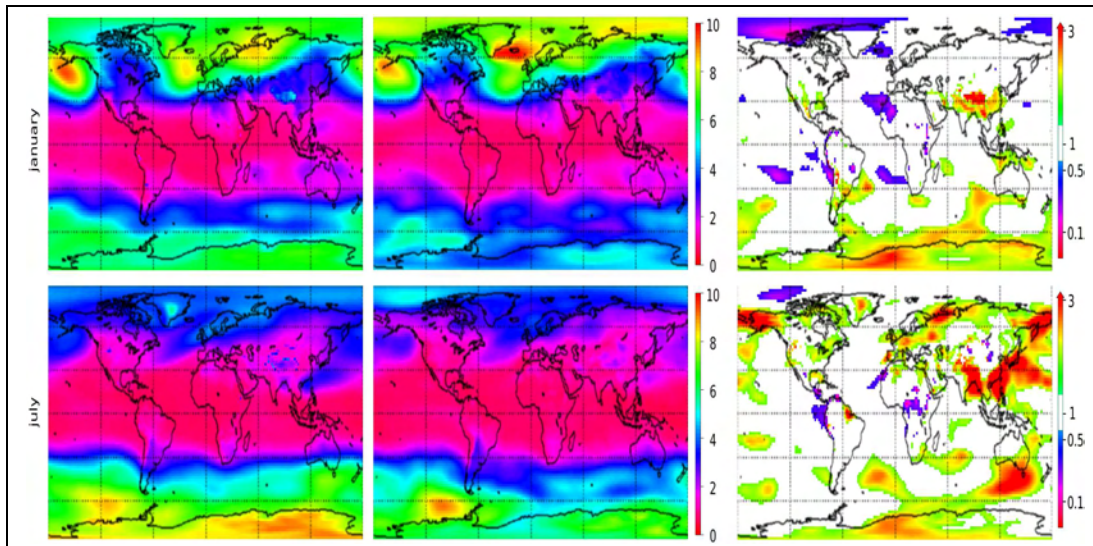
January and July and also well captured.

Figure 3.10: Top row: January standard deviation of MSLP 1958 to 2001 (in hPa); bottom row: July standard deviation of MSLP 1958 to 2001 (in hPa), first column: ECHAM5 (mean over all five members); second column: ERA40 and third column: difference between ECHAM5 and ERA40 (ECHAM5-ERA40) tested by F-test on five percent significance level (unsignificant differences are whitened).

A closer look to the ENSO region does not reveal any significant deviations. The Tahiti Darwin pressure gradient which is the basis for the Southern Oscillation Index (SOI) looks quite similar in ECHAM5 and ERA40. Obviously there is no bias in the SOI of the ECHAM5 model. Apparently orography still has a huge impact on the MSLP in the ECHAM5 model. Some unrealistic values are retrieved over elevated regions assuming a negative bias — Tibet and the Andes are the most noticeable in July. Surface pressure is a prognostic variable in the model whereas MSLP is derived from surface pressure, orography, humidity and temperature. Apparently, the pressure extrapolation to MSLP values is different in ECHAM and ERA leading to a significantly positive bias in ECHAM. Besides these artefacts, the only significant differences to the ERA40 data are found in July at Central and Southern Africa and at the tropical West Pacific.

For the MSLP, the standard deviations were calculated as well (see Fig. 3.10). In January the region of the Aleutian low and the Icelandic low have the highest variability in MSLP. In winter significant underestimation of pressure standard deviation is located over the Arctic ocean. At high latitudes of the Southern

Hemisphere MSLP variance is systematically overestimated. Other regions agree reasonably well. In July the overestimation of the Antarctic MSLP variability is even more pronounced in ECHAM5 but on the other hand departures are rather small for the rest of the world.

To conclude this chapter and this short model analysis, it is stated, that the deviations seen are predominantly of local nature. The global integrals hardly show any deviations (see Fig. 3.6). The quality of the model as far as it is assessed by the analysis here is absolutely adequate pertaining to the purpose of global angular momentum analysis.

Chapter 4

Coupled Atmosphere Ocean Simulations

In the previous chapter the atmospheric standalone GCM was introduced. For the purpose of a scenario analysis two ocean-atmosphere coupled models are used. A1B scenario runs from two different models will be presented. The A1B scenario is a SRES scenario (Nakicenovic and Swart, 2000) which describes a future world of rapid economic growth and global population that peaks in mid-century and slowly declines thereafter while new efficient technologies will then be introduced. CO_2, CH_4, N_2O, NO_x, CO and SO_2 concentrations are derived from this economic and demographic scenario.

4.1   ECOCTH

ECOCTH stands for ECHAM-Ocean-Circulation-Tide-Hydrology model. The atmospheric part of this model is quite similar to the atmospheric standalone one. The identical ECHAM version 5.3.02 is implemented, but differences exist in boundary conditions. In ECOCTH a dynamic coupling to the MPI-OM ocean model (Marsland et al., 2003) including tides is realised. The tidal module is based on the OMCT model (Thomas, 2002). The OASIS coupler has been adopted by Xueen Chen and Malte Müller from the Institute of Oceanography University Hamburg.

The atmospheric forcing does not comprehend aerosols, but volcanic effects are respected in the variation of the solar irradiation. The horizontal, vertical and temporal resolution is equivalent to the standalone runs. An ensemble of three members covers a period from 1860 to 2060.

4.2 ECHO-G

The A1B scenario run for a time span of 200 years (2000 to 2200) was performed by the free coupled atmosphere-ocean-sea ice model ECHO-G (Legutke and Voss (1999); Min et al. (2005, 2006)). SST and SIC are internal model variables and not prescribed as boundary conditions. The model consists of the ECHAM4 (Roeckner et al., 1996) atmosphere GCM and the HOPE-G (Wolff et al., 1997) ocean model. Both models are predecessors of ECHAM5 and MPI-OM respectively. These model runs were part of the 4th Assessment Report (AR) of the Intergovernmental Panel on Climate Change (IPCC, 2007). The atmospheric resolution of these ECHO-G simulations is set to T30 in the horizontal (corresponding to a grid spacing of $\sim 3.75°$) and 19 layers in the vertical. The oceanic resolution is T42 ($\sim 2.8°$) with a meridional refinement up to $0.5°$ in the tropics and 20 vertical layers. Like for the ECOCTH three ensemble members only differing in the state of initialisation are present.

Chapter 5

Standalone Simulation of Earth Rotation Parameters

The simulation of the atmospheric effect on <u>E</u>arth <u>R</u>otation <u>P</u>arameters (ERP) is one major goal of this work. In general there are two methods for the derivation of the atmospheric effect on ERPs in literature these are sometimes called the geophysical fluid approaches. Both methods can be obtained by making the following assumptions:

- the Earth is a solid body

- external torques are negligible

As we know both assumptions are not perfectly true. Here, these simplifying assumptions are justified, because firstly the inner fluid core of the Earth is only known to have an effect on the interdecadal time scale. Secondly external torques from sun and moon entail long term centurial trends, both time scales are not part of the research which is done in this chapter. Other external torques such as planetary ones have a very small not measureable effect.

The separation in frequency space technique is prevalently used in investigations of the Earth's rotation. This technique has the advantage that it allows for distinguishing between effects of different physical mechanisms. One can not clearly separate several effects in the time domain. Therefore structure analyses in the frequency domain play a vital role.

Picking up the stated methods in the beginning of this section leads to the differentiation of the torque approach and the angular momentum conserving approach. As mentioned, the derivation of both methods has the same origin.

The torque approach calculates torques from the subsystems which apply directly
to the solid Earth. For the atmosphere one has to estimate the direction and
size of friction due to wind in the lowest atmosphere level for every point on the
solid Earth's surface. This type of torque induced by windstress is called friction
torque. Another type of torque is the mountain torque which accounts for the fact
that a torque is applied if an inclined plane is exposed to atmospheric pressure.
In recent years the torque approach had a decreasing relevance because globally
integrated torque effects on Earth's rotation were very inaccurate accompanied
by high uncertainty. The main problems in dealing with atmospheric torques
derived from atmospheric models are:

- the windspeeds in the very lowest level are the most uncertain ones

- windspeeds in the very lowest level are profoundly parameterised

- friction torques depend on surface roughness which over land is only rudi-
  mentary described by the models

- mountain torques depend on the orography in the model being not well
  represented

To conclude this paragraph it is adverted that the torque approach was not at
all used in this work. Instead the approach of angular momentum conservation
will be introduced following Barnes et al. (1983).

Temporal variations of Earth rotation are related to angular momentum fluc-
tuations in the various system components of the Earth. The Earth's reaction
on the redistribution of masses and motions follows from the solution of the Li-
ouville differential equation which describes the balance of angular momentum
in a rotating reference frame.

$$\vec{L} \;=\; \frac{d}{dt}\big(\underline{\mathbf{I}}\vec{\omega} + \vec{h}\big) \;+\; \vec{\omega} \times \big(\underline{\mathbf{I}}\vec{\omega} + \vec{h}\big) \tag{5.1}$$

Here $\underline{\mathbf{I}}$ denotes the combined tensor of inertia of the solid Earth <u>and</u> its sub-
systems, $\vec{h}$ stands for the angular momenta with respect to the reference frame
(so-called relative angular momenta) and $\vec{L}$ on the left hand side denotes exter-
nal torques applied to the whole system and will be neglected in the following.
The Earth's angular velocity is given by $\vec{\omega}$. The Liouville differential equation
is a coupled system of non linear first order differential equations which is not
explicitly solvable. In the following the equations will be solved by a linearisation

approach.

Variations of Earth rotation are computed with respect to a uniformly rotating geocentric reference frame with its z-axis, about which it rotates, pointing approximately to the direction of the maximum moment of inertia. The angular velocity of the uniform rotation is one revolution per sidereal day: $\Omega = 2\pi/86164\text{s}^{-1}$. Due to geophysical processes and gravitational torques this uniform rotation is slightly disturbed and the Earth rotation vector deviates slightly from a state of uniform rotation. Perturbations in $\underline{\mathbf{I}}(t) = \tilde{\underline{\mathbf{I}}} + \Delta\underline{\mathbf{I}}(t)$ and $\vec{h}(t) = \tilde{\vec{h}} + \Delta\vec{h}$ produce small deviations in $\vec{\omega}(t) = \tilde{\vec{\omega}} + \Delta\vec{\omega}(t)$. The perturbations $\Delta\vec{h}(t)$ and $\Delta\underline{\mathbf{I}}(t)$ are induced by variations in the subsystems. The small deviations in this case can be studied by linearising.

$$\tilde{\vec{\omega}} + \Delta\vec{\omega}(t) \; = \; \Omega \cdot \begin{pmatrix} m_1(t) \\ m_2(t) \\ 1 + m_3(t) \end{pmatrix}, \qquad m_i \ll 1\,. \tag{5.2}$$

As presented by Munk and MacDonald (1960) the dimensionless quantities m_i denote small disturbances of the uniform rotation. Fluctuations of the absolute value of angular velocity of the Earth are equivalent to changes of length-of-day (ΔLOD). They follow from temporal variations of the absolute value of the Earth rotation vector $|\vec{\omega}(t)|$, which are computed by

$$\left|\tilde{\vec{\omega}} + \Delta\vec{\omega}(t)\right| \; = \; \Omega \sqrt{m_1(t)^2 + m_2(t)^2 + (1 + m_3(t))^2} \tag{5.3}$$

$$\approx \; \Omega\,(1 + m_3(t))\,. \tag{5.4}$$

$\Omega = |\tilde{\vec{\omega}}|$ is the mean angular velocity of the Earth. The error of ΔLOD due to the approximation (Eq. 5.4) is in the order of 10^{-16}s and thereby is negligible. The relation between the variations $|\Delta\vec{\omega}(t)|$ and length-of-day changes follows from the definition of ΔLOD as the duration of one revolution of the Earth reduced by one nominal sidereal length-of-day $\text{LOD}_0 = 86164s$:

$$\Delta\text{LOD(t)} = \frac{2\,\pi}{\left|\tilde{\vec{\omega}} + \Delta\vec{\omega}(t)\right|} - \text{LOD}_0 \tag{5.5}$$

Keeping terms in first order and neglecting external torques the linearisation of Equation 5.1 yields for the third component:

$$\Omega C_m m_3 + \Omega \Delta I_{zz} + \Delta h_z = 0 \tag{5.6}$$

$C_m = \tilde{\underline{\mathbf{I}}}_{zz} \approx 7.04 \cdot 10^{37}\ kg\ m^2$ is the polar moment of inertia of the Earth.
Only considering the atmosphere as a geophysical fluid qualifies for the following
assumptions in Eq. 5.7 and Eq. 5.8 respectively.

$$\Delta h_z = \Delta h_z^{AAMmotion} \tag{5.7}$$

$$\Omega \Delta I_{zz} = \Delta h_z^{AAMmatter} \tag{5.8}$$

$$m_3(t) = -\frac{\Delta h_z^{AAM}}{\Omega C_m} = -\frac{\Delta h_z^{AAMmotion}(t) + l\Delta h_z^{AAMmatter}}{\Omega C_m} \tag{5.9}$$

$$l = 0.7 \tag{5.10}$$

$$\Delta \text{LOD} = \frac{\text{LOD}_0}{C_m \Omega}(h_z^{AAMmotion}(t) + lh_z^{AAMmatter}) \tag{5.11}$$

Polar motion is related to the temporal variation of $m_1(t)$ and $m_2(t)$. Equations
5.9 and 5.11 show the dependence of $\Delta\text{LOD}(t)$ on $m_3(t)$. The weighting factor
or Love number l for the matter term (Eq. 5.9) accounts for the reaction of
the crust and mantle to imposed surface loads. As stated above the Earth is
supposed to be solid but not rigid which means that it is able to compensate
load effects or to deform itself.

Not only the Earth's crust or mantle deforms as it is imposed to atmospheric
pressure, but also the ocean is affected. As this work focuses on the atmosphere,
the compensating effect of the ocean is not considered. This is referred to as
non-inverse barometry (non-IB) assumption. As a consequence the matter term
of both atmosphere and ocean has to be considered to derive physically correct
ERPs. For time scales of more than some days the IB assumption is realistic
(Gaspar and Ponte, 1997).

As mentioned it is well known that the largest part of observed variations
of ΔLOD on time scales from months to a few years is caused by axial relative
atmospheric angular momentum h_z^{AAM} due to zonal wind and atmospheric mass
variations.

$$
\begin{aligned}
h_z^{AAM}(t) \;&=\; \int_{V_{atm}} \rho(\vec{r},t)r^2(\vec{r}\times\vec{v}(t))_z dV && (5.12)\\[4pt]
&=\; h_z^{AAM\,motion}(t) + h_z^{AAM\,matter}(t) && (5.13)\\[4pt]
&=\; \int_{V_{atm}} \rho(\vec{r},t)r^2(\vec{r}\times\vec{v_r}(t))_z dV + \Omega\, I_{zz}^{atm}(t) && (5.14)\\[4pt]
&=\; \frac{r^3}{g}\int_{\eta=0}^{\eta=1}\int_{\lambda=0}^{2\pi}\int_{\varphi=-\pi/2}^{+\pi/2} && (5.15)\\
&\quad\; p_{surf}(\lambda,\varphi,t)\,u(\eta,\lambda,\varphi,t)\,cos^2\varphi\,\;d\varphi d\lambda d\eta\\
&\quad\; +\Omega\frac{r^4}{g}\int_{\lambda=0}^{2\pi}\int_{\varphi=-\pi/2}^{+\pi/2} p_{surf}(\lambda,\varphi,t)\,cos^3\varphi\;d\varphi d\lambda
\end{aligned}
$$

Equation 5.12 shows the global integration over the whole atmosphere. Equations 5.13 and 5.14 were achieved by splitting the rotational motion of an air parcel into a part relative to a rotating reference frame of the Earth $\vec{v}_r(t)$ and another part with $\vec{v}_r(t) = 0 \;\Rightarrow\; u(\eta,\lambda,\varphi,t) = 0$ in a fix star reference frame. Zonal windspeed $u(\eta,\lambda,\varphi,t)$ and surface pressure $p_{surf}(\lambda,\varphi,t)$ are obtained from the model's output. η is the standardised vertical coordinate of the atmospheric GCM. Boundaries are $\eta = 0$ for the top of the atmosphere and $\eta = 1$ for the Earth's surface (see section 3.2.2).

Derivations of the equatorial (x- and y-) component are quite similar, but as a matter of fact contain one transformation of the coordinate system which involves further trigonometrical terms. For a detailed step by step derivation see Appendix D.

5.1   Interannual ΔLOD Variations

The underlying red noise spectrum in Fig. 5.1 was estimated by calculating the first coefficient α_1 of the auto-correlation function and estimating the variance. This was done for every member of the whole bootstrap sample, thereinafter the median of spectral density for every specific frequency was drawn. This technique ensures an excellent signal to noise ratio compared to a single realisation. Therefore a smoothing procedure was not applied to the spectrum because it seemed dispensable. In the following section named "Seasonal ΔLOD Variations" (5.2) the same Figure was calculated for seasonal frequencies.
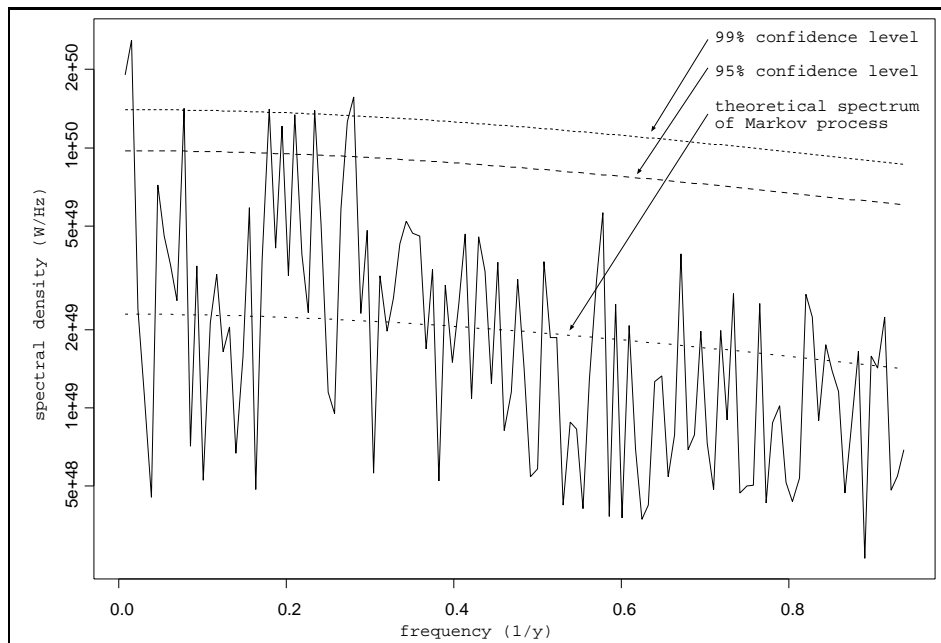
Figure 5.1: Power spectrum of ECHAM5 simulated axial AAM (matter/non-IB+motion) for 1880 to 2006 period - unfiltered median of 1000 bootstrap samples.

Fig. 5.1 shows significant fluctuations at 12 year periods for the one percent level. These signals can be linked to the sunspot or solar cycle, although it is established to have slightly shorter periods of about 11 years. Other signals are detected in a band covering periods from 3.5 to 5.5 years. These phenomena with their typical broad band structure are related to ENSO.

5.1.1   El Niño Southern Oscillation

Whereas interdecadal or slower variations in ΔLOD are definitely driven by nonatmospheric processes, the atmosphere plays the most important role in the interannual domain (Rosen (1993); del Rio et al. (2000); Stuck (2002); Gross et al. (2004)). Apparently the AAM is particularly sensitive to the interannual variations of SSTs in the tropical Pacific. These fluctuations are a good indicator of the El Niño Southern oscillation. ENSO describes a complex coupled circulation system of the atmosphere and ocean in the tropical Pacific. While El Niño is a positive phase of the ocean in first sense the Southern oscillation represents atmospheric coherences (Philander, 1990). Both phenomena have to be treated jointly as they are strongly coupled in both directions.

Today the most frequently used index for characterising the current ENSO

state in atmospheric science is the so called NINO3.4 index. The NINO3.4 index
is defined as a five month mean of SST anomalies inside a rectangle in the Central
Pacific (5N°-5S°; 120W°-170W°). The evidential AAM-ENSO relation was al-
ready discovered by Rosen et al. (1984). Further investigations on this topic were
done by numerous authors (Chao (1984, 1988, 1989); Hide and Dickey (1991)) all
using observed ∆LOD data and atmospheric reanalysis data. Model approaches
became popular in the late 1990s as the quality of the models allowed for thor-
ough studies on these effects (e.g. Hide et al. (1997); Naito et al. (2000); Stuck
(2002)).

ENSO has an impact on many processes in the global climate system. For
many globally integrated meteorological variables it is the main mode on in-
terannual time scales. E.g. fingerpints of ENSO can be found in global mean
temperature, global mean precipitation and global mean zonal wind. Therefore
a fingerprint in AAM is anticipated.

The exact mechanism of how El Niño events are generated is still a current
research topic (Diaz and Markgraf, 2000). The fact is that Kelvin waves prop-
agate eastward in the upcoming of an event. They lift the sea level and lower
the thermocline. Due to Coriolis forces the eastward stream above the thermo-
cline and the westward stream below intensify. This leads to a strong decrease
in vertical mixing which enables the layer above the thermocline to warm up
abnormally. In the opposite event of La Niña the atmospheric trade winds are
stronger and impose an westward windstress to the ocean which allows cold deep
water to rise at the South American west coast due to mass conservation. Equa-
torial easterlies disperse cold water westwards in an equatorial belt.

The wavelet spectrum in Figure 5.2 illustrates typical characteristics of ENSO
in frequency domain. First of all it should be noted that the quality of the data
was rather poor before the late 1960s when only SST measurements from ships
were at hand. The introduction of satellite measurements and particularly the
launch of the Tropical Atmosphere Ocean array (TAO network) in 1980 dra-
matically increased the quality of the data. The TAO network consists of 40
to 50 buoys measuring SST, current, Sea Surface Height (SSH) and other pa-
rameters continuously. The data quality inhomogeneity caused by the launch
of this campaign leads to more pronounced and more intense structures in the
wavelet spectrum after 1980. One important characteristic of ENSO is its ir-
regular oscillation which results in a complex structure in the wavelet spectrum.
Peaks of energy can be found in a broad band with periods ranging from 2 to
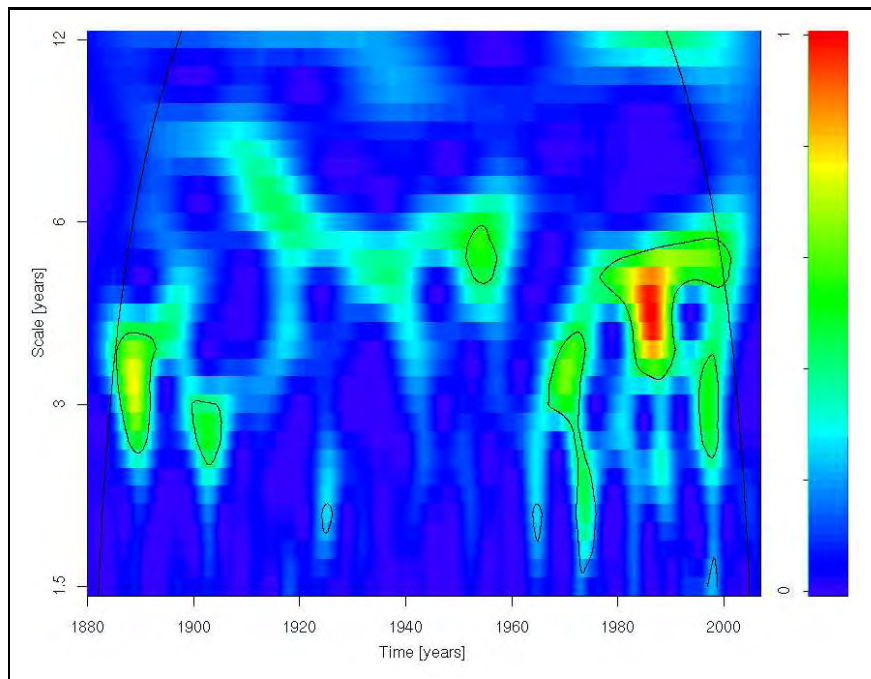
Figure 5.2: Wavelet power spectrum of NINO3.4 index based on Hadley centre
SST data, black contour line indicates five percent significance.

5.5 years. Also, ENSO is not homogeneously distributed in time and sometimes
signals even vanish. There are indications that strong ENSO phases enhance the
seasonal and semiannual variability which is embodied by several "connection
paths" in the wavelet spectrum between ENSO and seasonal signals (Gross et al.
(1996); Lehmann et al. (2008)).

The time series plot (Fig. 5.3) covers the 1962 to 2006 period. In 1962 the
EOP 05 C04 data set from the IERS begins. This data set provides error es-
timates for daily values. The error bars have been computed by $\sigma_{obsLOD} = \sum_{i=1}^{N=1461} \frac{\sigma_i}{\sqrt{N}}$. 1461 days correspond to four years which matches the central pe-
riod of the frequency band of the figure. It is obvious that the error bars decrease
considerably in time as the accuracy of the measurements has improved vastly
since the early 1960s. Likewise from 1984 on they were disregarded since their
extent became smaller than the line size. For clarity reasons error bars were only
added every three years or when the size of the error had changed. Launching
new measurement devices increased the quality of the data stepwise. In 1980
VLBI (see chapter 1.4.1) measurements were introduced, causing a leap in data
quality. The IERS states an error of $\sigma_{LOD}^{1979} = \pm0.7\ ms$ for daily mean values
in 1979 and an error of $\sigma_{LOD}^{1980} = \pm0.15\ ms$ in 1980. Likewise, the introduction
of a new VLBI network reduced the daily mean error from $\sigma_{LOD}^{1980} = \pm0.15\ ms$
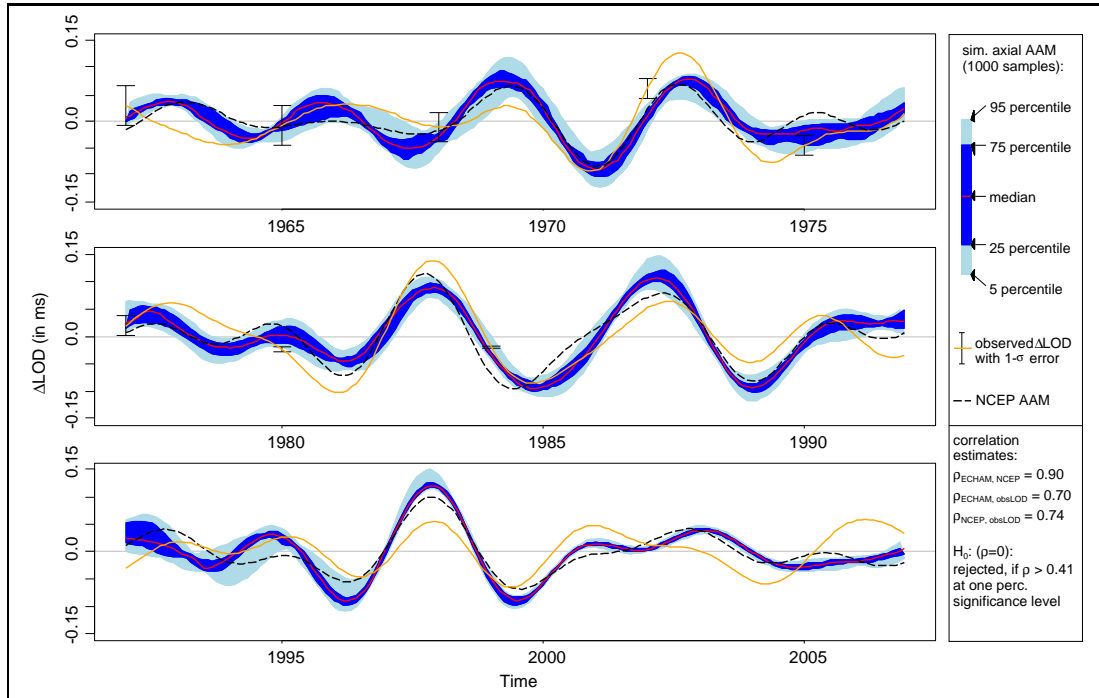
Figure 5.3: Observed ΔLOD (orange line), NCEP$_{AAM}$ (dashed black) and
ECHAM5 (blue shading, red line median) axial combined AAM (mass+motion)
in a 2.5 to 5.5 year frequency band.

to round about $\sigma_{LOD}^{1984} = \pm 0.025 \ ms$ in 1984. Nowadays VLBI measurements
contribute 94 percent to the observed ΔLOD signal (Pâquet et al., 1997).

The uncertainty of the model, represented by the spread of blue bands, varies
strongly. E.g. the 1990 to 1995 period is characterised by large uncertainties,
while the 2000 to 2005 period shows small uncertainties. Obviously the size of
uncertainty depends on the boundary conditions imposed.

The simulated ECHAM5 AAMs are in very good agreement with the observed
C04 ΔLOD time series. The oscillations are exceedingly well reflected resulting
in a correlation of $\rho_{ECHAM,obsLOD} = 0.70$. In this case the correlation is close to
that of the reanalysis data with the geodetic observations $\rho_{NCEP,obsLOD} = 0.74$.
Both correlations are well above the 99 percent confidence level because they
exceed a correlation of $\rho_{\alpha=0.01}^{critical} = 0.41$ by far. These correlations were calculated
in the time domain, which means that they are the correlations of two auto-
correlated samples. The statistical tests have to consider this fact, and therefore
the equivalent sample size replaces the actual sample size for the test procedure.

73

The degrees of freedom DOF which is a fundamental variable for the statistical test follows directly from the equivalent sample size definition (see Eq. 2.21).

$$
\begin{aligned}
\hat{DOF}_{ENSO-band} &= 2\lfloor n' \rfloor - 2 & (5.16) \\
&= 19 * 2 - 2 & (5.17) \\
&= 36 & (5.18)
\end{aligned}
$$

For a detailed deduction of the confidence levels of the correlation coefficient see chapter 2.1.10 "Hypothesis testing".
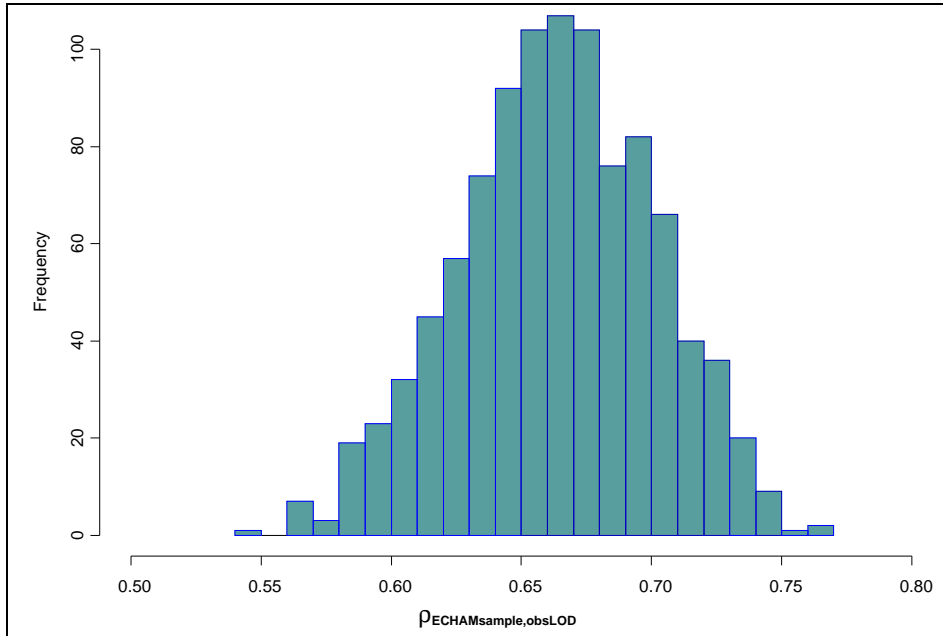

Figure 5.4: Histogram of correlation coefficient between simulated ECHAM5 AAM samples (matter/non-IB+motion) and observed ΔLOD (2.5 to 5.5 year band pass filtered).

The histogram of correlation coefficients $\rho_{ECHAM,obsLOD}$ for every bootstrap sample shows a distribution close to a Gaussian. Interestingly the spectral correlation of the $\underline{AAM\ median}$ $\rho_{ECHAM,obsLOD} = 0.70$ is much higher than the mean correlation $\overline{\rho_{ECHAM,obsLOD}^{samples}} = 0.66$ of all bootstrap samples. The nature of the median implies more information than a single realisation, therefore this result is not very astonishing. In general the median contains less noise then a single realisation.

The correlation coefficient map in Figure 5.5 backs the fact that there is a strong statistical relation between 2m temperatures in the tropical Central Pacific
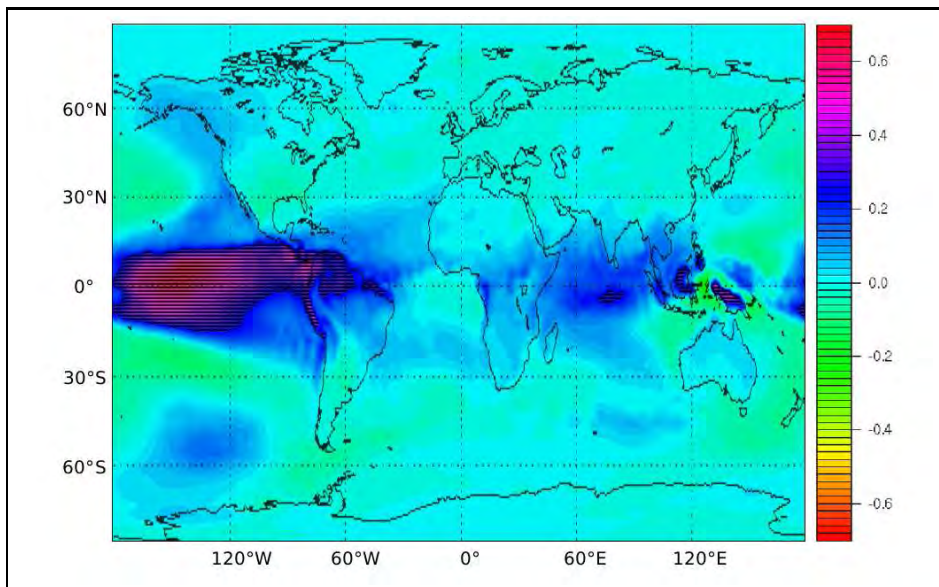
Figure 5.5: Correlation coefficient $\rho_{AAM_z^{ECHAM},simTemp2m}$ between grid point 2m temperature (ECHAM5 ensemble mean) and simulated axial AAM (median) time series for the 1880 to 2006 period (2.5 to 5.5 year band pass filtered); shaded areas display a significant correlation on the one percent level ($\rho_{\alpha=0.01}^{critical} > 0.259$) respecting auto-correlation.

region and axial AAM. The hotspot of correlations above $\rho_{AAM_z^{ECHAM},2mTemp(\lambda,\varphi)} > 0.6$ matches the NINO3.4 region quite well. The underlying time series cover a period from 1880 to 2006. Compared to the analysis of observed ΔLOD reconstruction (Fig. 5.3) the sample size has increased strongly leading to a smaller critical correlation on the one percent level.

Of course the 2m temperature over sea is mainly forced by the underlying SST. Other patterns on the map are often related to spatial auto-correlation with ENSO. A small area in the Central Indian Ocean shows a significant correlation. Whether there is a teleconnection to ENSO or this is rather a peak of another climatic mode is questionable. Another region of remarkable correlation is the west coast of Alaska and Northern Canada. In this case a teleconnection to ENSO is much better understood (Straus and Shukla, 2002) and it is called Pacific-North American (PNA) pattern. The Aleutian low is intensified and is found to the east of its normal position in association with El Niño. Therefore the warm air sector of the Aleutian low is preferentially located at the west coast of Alaska and Northern Canada. A clear dependence on orography is obvious with a tendency to higher correlations in elevated regions. Fingerprints of the Andes (up to 6,962m in reality), Borneo (up to 4,095m) and Papua New Guinea

(up to 4,509m) can be seen. Probably the 2m temperature in these elevated regions contains less noise as it is not affected by the boundary layer, which means that the temperature variations are to a bigger extent influenced by large scale circulation.

5.1.2 Quasi-Biennial Oscillation

Berson launched observational balloons above Lake Victoria in 1908 in Africa. He found westerly winds at about 15 km (120 hPa). Thereinafter these westerly winds were called Berson's westerlies. The Quasi-Biennial Oscillation (QBO) was originally discovered in 1960 by Reed et al. (1961). One year later it was affirmed by Veryard and Ebdon (1961) as they independently discovered the same phenomenon, all showing that the wind above the equator oscillates in East-West direction. It was pointed out that the wind in the stratosphere changed direction on average every 27/28 months and that the alternating easterly and westerly wind regimes descend with time. These are the essential properties of the QBO.
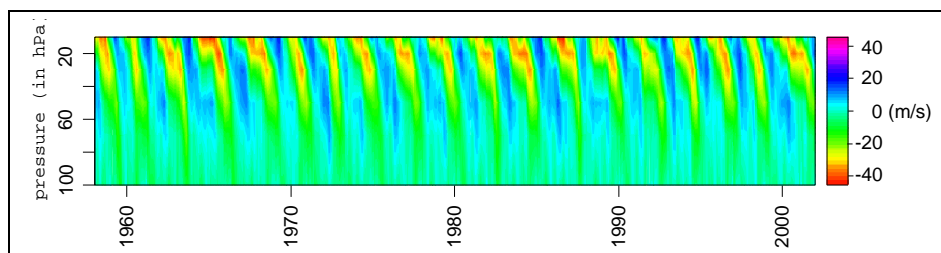
Figure 5.6: Time-height section of equatorial (3°N to 3°S) monthly mean zonal winds from ERA40 reanalysis data.

A lot of key features of the QBO are nicely displayed by time-height sections of monthly mean zonal wind at the equator. From Fig. 5.6, which is based on ERA40 reanalysis data one can gather these features. The QBO appears in an equatorial band ($\sim$ 10°N to $\sim$ 10°S) between 10hPa and 100hPa. The defining characteristics are:

- The wind regimes propagate down as time progresses.

- The propagation speed is roughly 1 $km/month$ and decreases in magnitude as height decreases.

- The period of the oscillation is 22 to 34 months with a mean of around 27/28 months.

- The wind regimes arise at 10 hPa and descend to 100 hPa where they vanish.

- The maximum amplitude of 40 to 50 m/s is reached approximately at the 20 hPa level. Nevertheless there is considerable variability in amplitude.

- Easterlies are stronger than westerlies in general.

- Westerly winds last longer than easterly winds at higher sections while the opposite is seen at lower sections.

- In the 30 to 50 hPa region the transition between westerly and easterly regimes is commonly delayed.

Although the main characteristics of the QBO were well revealed in the 1960s there was no commonly accepted physical explanation for it. First approaches tried to explain the QBO on postulating biennial cycles either in the diabatic forcing in the stratosphere or in the various elements of tropospheric circulation, aside from the fact that there was already evidence that the oscillation is not precisely biennial.

The physical mechanism driving the QBO is a current research area (Labitzke, 1998). One process which accounts for the main QBO aspects was found in the vertical momentum transfer through gravity waves. It is now thought that equatorially trapped Kelvin waves provide the westerly momentum and mixed Rossby-gravity waves provide easterly momentum to produce the QBO oscillation. The upward propagation of these waves deposits momentum just below the maximum of zonal windspeed. Therefore wind regimes propagate downward in time.

Giorgetta et al. (2006) defined a critical vertical resolution of 1km in the stratosphere to simulate the QBO reasonably. This vertical resolution is only present in the stratospheric version of the ECHAM5 model which in this version has 80 vertical layers in total. The standard tropospheric version used for the standalone and coupled studies only has a number of 31 vertical layers. This is not at all sufficient to account for simulating QBO sources. Fig. 5.7 shows the spectrum of equatorial zonal wind at the 10hPa level representing the top layer of the model. There is one major signal with a semiannual period. The confidence levels were calculated by making the null hypothesis that the underlying process is a Markovian. This hypothesis is rejected at the 95 and 99 percent confidence level for half year periods. For a realistically simulated QBO one should see
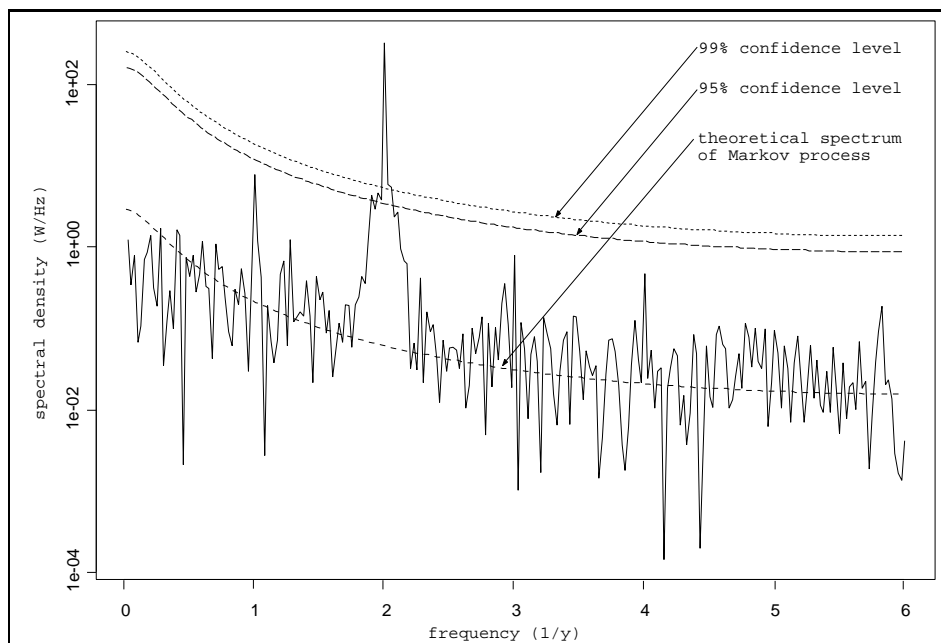
Figure 5.7: Power spectrum of simulated ECHAM5 ensemble mean equatorial (3°N to 3°S) zonal wind at 10hPa.

strong signals in a band around the 27 month period which is not the case at all. These facts lead to the reasoning that the atmospheric GCM fails to simulate the QBO.

To investigate the impact of the QBO effect on the LOD, a structure analysis of observed ΔLOD values and ERA40 reanalysis wind fields is carried out. Typical QBO characteristics as those mentioned above can well be seen in the ERA40 data, but observational data in the equatorial stratosphere are pretty rare. The observational coverage of the QBO region was much worse in the early part of the ERA40 time span. In the 1950s and 1960s there were only three time series of radio soundings on hand (for Singapore 1°N/104°E, Canton Island 3°S/172°W and Gan/Maledive Islands, 1°S/73°E). These time series (especially the Canton Island and Gan one) are of low quality as there are many interruptions. The quality of the ERA40 data decreases at the upper QBO region as observations become significantly rarer. A boost in quality was achieved when satellite observations became available in 1978/79. Punge and Giorgetta (2007) found strong systematic differences between the first and second half of the ERA40 time span at the higher stratosphere also affecting the amplitude of the QBO: "*The identified change of the assimilated wind profiles over time in ERA40 requires a careful use of equatorial upper stratospheric winds from the reanalysis for validation pur-*

78

*poses. [...] It is likely that the latter part of the reanalysis suits better for such
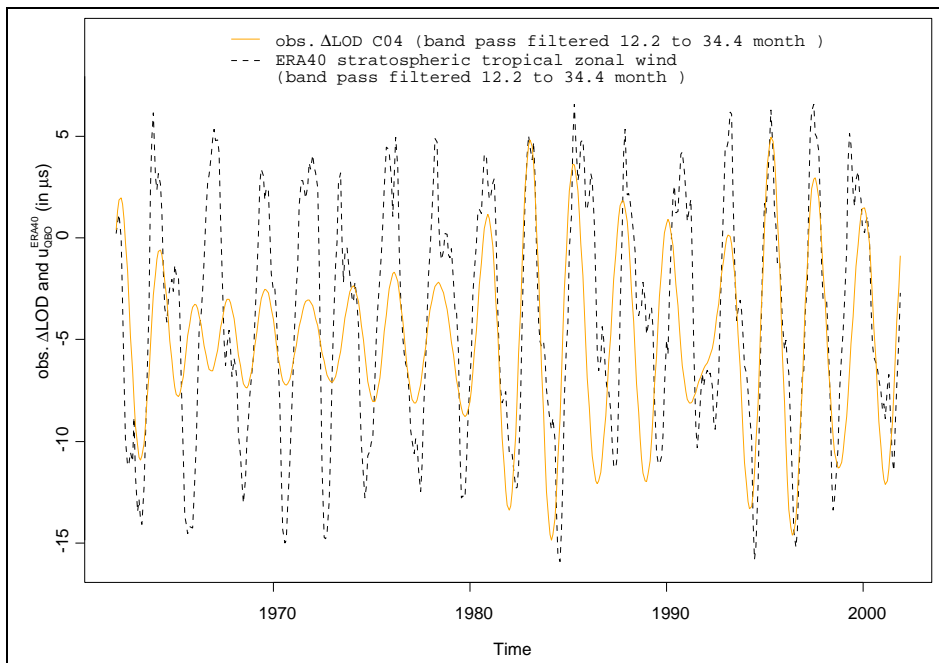purposes."*

Figure 5.8: Time series of monthly mean observed ΔLOD (solid orange line) and
$\overline{u_{QBO}^{ERA40}}$ (dashed black line), a band pass filter was applied with cut-off frequencies
of 21.8 and 34.3 months.

Indeed, the QBO influence derived from ERA40 wind field data on observed
ΔLOD becomes much stronger for the second half of the ERA40 time span. The
horizontal resolution of ERA40 data is T159 representing a global gaussian grid
consisting of 480x240 grid points. The distance of two neighbouring grid points
is approximately 0.75°. The zonal mean wind in the QBO region is calculated
for every timestep as follows.

$$\overline{u_{QBO}^{ERA40}} = \frac{\int_{p=100hPa}^{p=10hPa} \int_{\varphi=-3°}^{\varphi=3°} \int_{\lambda=0°}^{\lambda=360°} u^{ERA40}(\lambda, \varphi, p)d\lambda d\varphi dp}{\Delta p = 90hPa} \tag{5.19}$$

The ERA40 data are available for the 100,70,50,30,20 and 10hPa pressure
levels and for eight grid points in North South direction between 3°N and 3°S.
Fig. 5.8 shows time series of observed LOD variations and ERA40 mean zonal
wind in the QBO region. The ΔLOD time series is influenced by many effects.
A lot of these effects have characteristic frequencies or frequency bands which
do not overlay in general. Therefore band pass filtering is a very effective tech-
nique to distinguish between certain effects on ΔLOD. In this case the ΔLOD

time series was band pass filtered by reconstructing the time series with only
considering Fourier coefficients 14 to 22. This stands for cut off frequencies of
21.8 and 34.3 months which is suitable to capture the quasi-biennial band. The
solid orange line in Fig. 5.8 represents this reconstructed time series. Its scale is
on the right, the scale of the ERA40 zonal winds is transformed to LOD varia-
tions as well to make both series comparable. The observed ΔLOD has bigger
amplitudes from the early 1980s on. A reason for this cannot be given easily.
Perhaps enhancements in the accuracy of LOD measurements which were vastly
achieved at that time were able to detect this signal more clearly. One has to
keep in mind that amplitudes in the quasi-biennial band are comparably low and
reach roughly five percent of the seasonal amplitude.
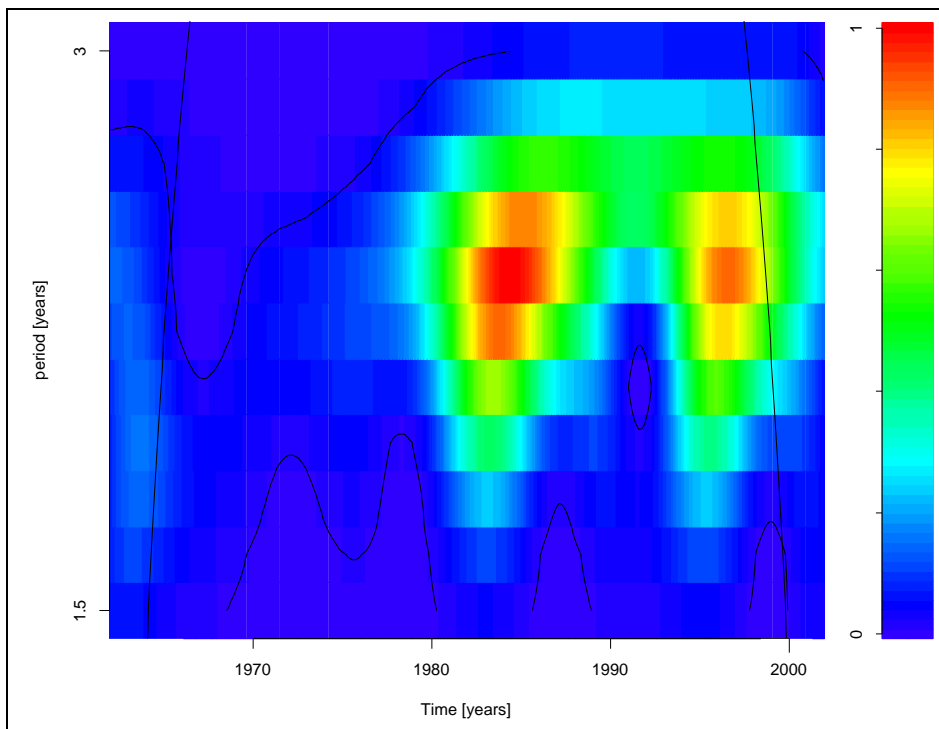
Figure 5.9: Observed wavelet power spectrum of ΔLOD, black contour line in-
dicates five percent significance.

In Fig. 5.9 the wavelet power spectrum of observed ΔLOD reveals this phe-
nomenon adequately. In the early 1980s a branch to higher energies and lower
frequencies is displayed. The integral over time peaks at a period of 28.2 months
which matches the observed mean period of the QBO quite well. The corre-
lation of the variables from Fig. 5.8 is $\rho_{obsLODbiennial}^{u_{QBO}^{ERA40}} = 0.49$ for the 1962 to
1981 period and reaches $\rho_{obsLODbiennial}^{u_{QBO}^{ERA40}} = 0.69$ for the 1982 to 2001 period. It

seems not very likely that the QBO effect on ΔLOD changes that much on interdecadal time scales. Obviously this rise in correlation is due to changes in the observation techniques — particularly the stratospheric ones. The strongest signals coincide with strong ENSO events like 1982/83 and 1997/98. It is heavily debated whether there is a link between ENSO and QBO variability (van Loon and Labitzke (1987); Yasunari (1989); Angell (1992); Gray et al. (1992); Xu (1992); Baldwin and O'Sullivan (1995); Baldwin et al. (2001); Chattopadhyay and Bhatla (2002); Zheng et al. (2007); Salby and Callaghan (2007)). Van Loon and Labitzke detected a coincidence of ENSO and QBO phases. QBO easterly regimes are mainly observed during ENSO warm periods. However Xu (1992) found no direct significant statistical relationship between the two climate modes. The connection seems to be far more complex suggesting nonlinear or multivariate complexity. On a particular aspect Maruyama and Tsuneoka (1998) could demonstrate a distinct connection. They were the first to show that ENSO warm events evidently enhance the rate of QBO westerly descent also giving a plausible physical mechanism to explain the connection. Apparently this effect does not result in any linear correlation.

5.2 Seasonal ΔLOD Variations

The mean seasonal cycle of simulated ECHAM5 axial AAM for the 1962 to 2006 period is calculated and compared to a least squares fitted harmonic annual and semiannual oscillation (see Fig. 5.10). The AAM of the month January is the most sensitive and shows the largest uncertainties. In the bottom panel of Fig. 5.10 the difference between the simulated ECHAM5 axial AAM and its annual and semiannual constituents is illustrated. In general the seasonal cycle is rather well explained by its annual and semiannual constituents (see top panel of Fig. 5.10). Significant deviations are found in May and June, obviously the strong decrease at this time of the year is non-harmonic to a certain degree. Therefore a Fourier Tranformation has to generate high frequent oscillations to describe this strong decrease in the time domain.

Similar to the power spectra in the previous section the underlying red noise spectrum in Fig. 5.11 was as well estimated by calculating the first coefficient α_1 of the auto-correlation function and estimating the variance for the two plots in the upper panel. The signal to noise ratio increased enormously in the top left AAM spectrogram compared to a single realisation because the median of all bootstrap samples contains less noise than a single realisation. This effect is highlighted by additionally added single realisations (solid grey lines). It should be noted that for the single members the terannual, quadrannual, quintannual
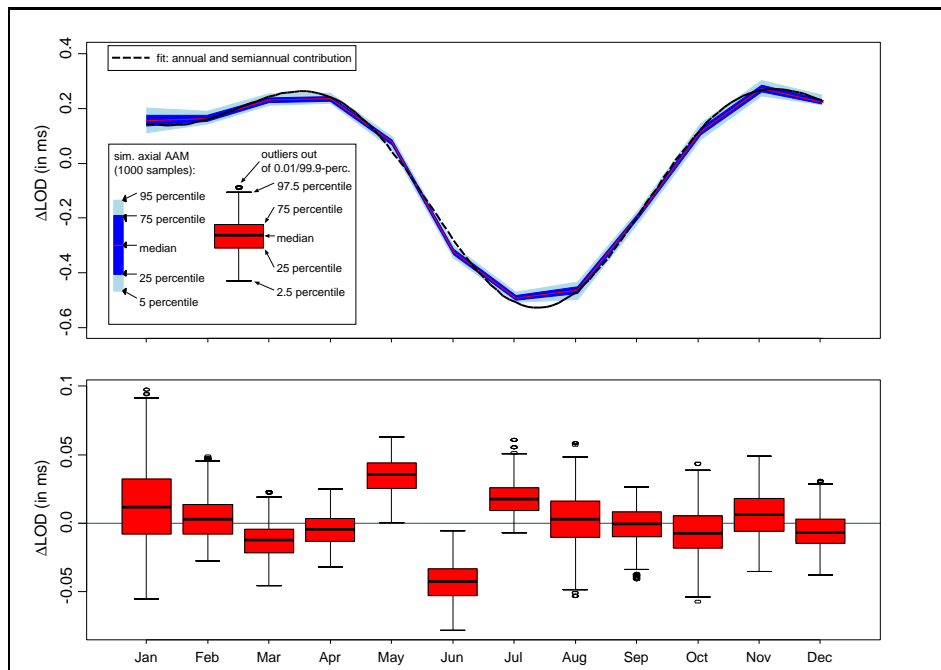
Figure 5.10: Top: mean seasonal cycle of ECHAM5 axial AAM (matter/non-
IB+motion) for 1962 to 2006 period (1000 samples),
bottom: deviations of mean seasonal cycle from harmonic annual and semiannual
contribution.

and 2 month signals vanish due to an overlapping by noise.

The huge sample size afforded statistically significant signals at frequencies of
$f = \frac{N}{1y}$ with $N = 1, 2, 3, 4, 5....$ This work was able to confirm the occurrence of
signals at these frequencies in an atmospheric GCM with a reliability exceeding
reanalysis studies by far. The experimental design of the study is responsible
for this. Nevertheless high spectral densities at frequencies $f = \frac{N}{1y}$ do not point
at certain physical mechanisms, the annual and semiannual cycle is obviously
not perfectly trigonometric as demonstrated in the previous Figure (5.10) which
means that terms at $f = \frac{N}{1y}$ are needed to describe these cycles in a Fourier
series.

On the top right panel in Fig. 5.11 the power spectrum of the observed ΔLOD
C04 time series is depicted. The corresponding red noise spectra were gained by
estimating both the first coefficient α_1 of the auto-correlation function and the
variance.

The bottom panel shows the squared coherence of both spectra. The calcula-
tions were carried out for every bootstrap member, but for reasons of clarity only
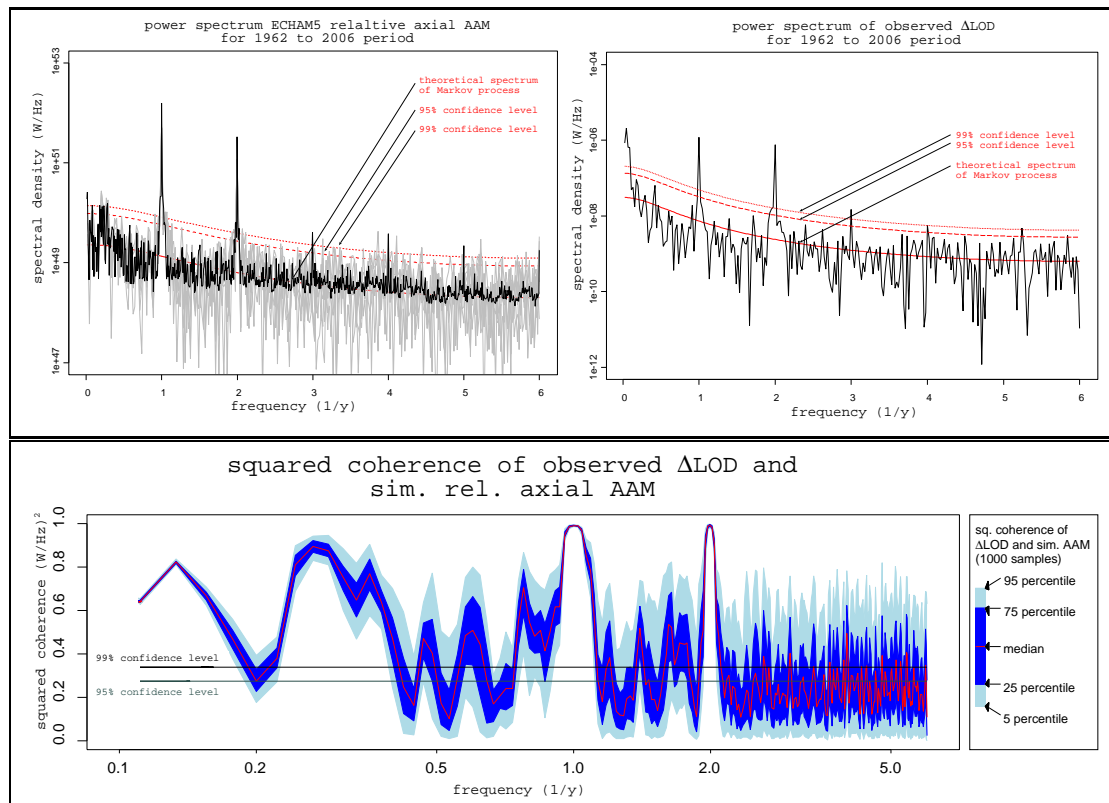
Figure 5.11: Top left: spectrum of ECHAM5 axial AAM (matter/non-IB+motion) for 1962 to 2006 period, unfiltered median of 1000 bootstrap samples (black) and corresponding red noise spectra, six randomly chosen realisations (grey), top right: spectrum of observed ΔLOD C04 time series for 1962 to 2006 period,
bottom: squared coherence of observed ΔLOD and ECHAM5 axial AAM for 1000 bootstrap samples - LOESS smoothed with a bandwidth of five discrete frequencies.

the 5-,25-,50-,75- and 95-percentiles are displayed. The confidence levels were estimated by a formula introduced by Panofsky and Brier (1958) also known as Goodman's formula:

$$\beta^{cl} = \sqrt{1 - \alpha^{1/(DOF-1)}} \tag{5.20}$$

The confidence level $\beta^{cl} = \beta^{cl}(\alpha, DOF)$ depend on the probability of error α and the number of degrees of freedom DOF. Here once again the formula 2.21 for estimating the equivalent sample size was used taking auto-correlation into account.

Significant signals appear at annual, semiannual and interannual (2.5 y to

83

5 y) periods. Nevertheless noise dominates the subsemiannual section but containing significant terannual, quadrannual and quintannual signals with respect to the median of all samples.

5.2.1   Annual ΔLOD Variations

The annual and semiannual oscillations of ΔLOD were well examined by Höpfner (1998) and Gross et al. (2004) using atmospheric reanalysis data. This section aims to compare results from the ECHAM5 simulations for the annual and semi-annual period to those of observed ΔLOD and atmospheric reanalysis derived ΔLOD as done by the two authors mentioned above.
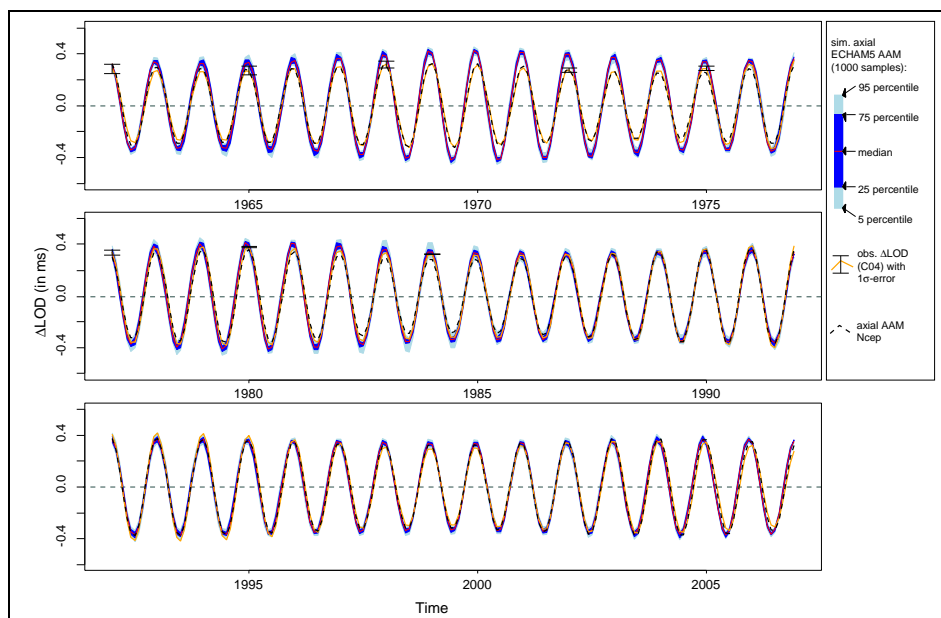
Figure 5.12: Annual variations in observed ΔLOD (orange, black error bars $\pm 1\sigma$), NCEP axial AAM (matter/nonIB+motion) (dashed black) and axial AAM (matter/nonIB+motion) from ECHAM5 simulations (blue shadings, red line) - Fourier bandpass filter applied (cut-off frequencies 10.8 and 13.5 month by only considering Fourier coefficients $c_{40}, \ldots, c_{50}$).

In Fig. 5.12 a bandpass filtered time series of observed ΔLOD, reanalysis axial AAM and axial AAM from the ECHAM5 simulation is displayed. The amplitude of the seasonal cycle is quite well captured, although it tends to slightly higher magnitudes in the simulations around the year 1970. The effect of atmospheric pressure is implied, this effect is countervailing the wind effect by about 10 percent. Whereas the compensating effect of the ocean to imposed atmospheric

pressure is not considered (non-IB assumption).

Stuck (2002) analysed the angular momentum budget of the ECHAM3 (Kli-marechenzentrum, 1993) model in his PhD thesis. The model was run in a T21 resolution and had comparable boundary conditions to the standalone runs carried out in this work. A T21 resolution means a distance of $\sim 5.6°$ between two neighbouring grid points, this is three times coarser than the T63 resolution of the standalone model. Therefore the model's grid point number is nine times smaller. Stuck found out that the ECHAM3 GCM explained less than 50 percent of the observed seasonal amplitude in ΔLOD. The inner physical core of the model hasn't changed much since version 3. This leads to the reasoning that the amplitude of the seasonal cycle in the axial AAM is sensitive to the resolution of the GCM.

Differences in amplitude and phase were calculated by fitting a trigonometric model (least squares method) of the shape as follows:

$$
\begin{align}
y(t) &= x_1 + x_2 cos(\omega t - x_3) \tag{5.21}\\
\omega &= \frac{2\pi}{1y} \tag{5.22}
\end{align}
$$

In the following $x_1 = 0$ was set to zero which is a valid assumption since Fourier coefficient $c_0 = 0$ is not respected in the time series of Fig. 5.12.

Due to the design of the model x_3 directly points at the maximum of the cycle. The estimated phase shift (see table 5.1) $\hat{\Delta\phi} = \hat{x}_3^{ECHAM5} - \hat{x}_3^{obsLOD} = -5.23 \ days$ is rather small and the simulated axial AAM time series is slightly preceding. All in all the phase of the seasonal cycle is very well replicated. One has to keep in mind that the data have a temporal resolution of one month.

The estimated amplitude ratio $\frac{\hat{x}_2^{ECHAM5}}{\hat{x}_2^{obsLOD}} \simeq \frac{367.0\mu s}{334.2\mu s} \simeq 1.098$ indicates that the annual cycle of the axial AAM is overestimated by the atmospheric model. Contrasting these results to previous versions of the ECHAM model chain is very encouraging on the other hand. NCEP reanalysis AAMs capture the annual amplitude very well, as the estimated amplitude ratio indicates $\frac{\hat{x}_2^{NCEP}}{\hat{x}_2^{obsLOD}} \simeq \frac{329.1\mu s}{334.2\mu s} \simeq$ 0.985. The results of Gross et al. (2004) who found an underestimation of roughly four percent in the NCEP AAMs are not fully substantiated. In his study the same data sets were used (NCEP1 and C04), the only differences to their study are probably in the tidal correction procedure and in the bandpass filtering where

	amplitude $(x_2^{ann}/\mu s)$	phase (x_3/day)	correlation with obs. ΔLOD $\rho_{obs\hat{L}OD}$
obs. ΔLOD	334.2	2.99	1
NCEP	329.1	-0.92	0.996
ECHAM5	367.0	-2.24	0.982

Table 5.1: Properties of the seasonal cycle in obs. ΔLOD, NCEP and ECHAM5, confidence levels for the correlation respecting auto-correlation are $\rho_{\alpha=0.05}^{critical} = 0.121$ and $\rho_{\alpha=0.01}^{critical} = 0.158$.

in this study a broad frequency band (10.8 to 13.5 months) was allowed to pass instead of looking at specific frequencies.

It is noticeable that the ECHAM5 results are stronger correlated to the NCEP results $\rho_{ECHAM5,NCEP} = 0.986$ than to the observed ΔLOD.

5.2.2 Semiannual ΔLOD Variations

Fig. 5.10 and 5.11 suggest that semiannual oscillations are an important mode within observed ΔLOD variations. Like, for the annual ΔLOD fluctuations the semiannual ones are primarily caused by semiannual changes in the angular momentum of the zonal winds (Rosen and Salstein (1985, 1991); Naito and Kikuchi (1990, 1991); Dickey et al. (1993); Rosen (1993); Höpfner (1998); del Rio et al. (2000); Cleveland (2000); Gross et al. (2004)). Gross found out that the combined ocean and atmosphere (both matter and motion terms) effect for this period only differs by less than 1.7 percent in amplitude from that of the single atmospheric motion term using atmospheric products version 1 from the NCEP/NCAR reanalysis project and oceanic data from the Estimating the Circulation and Climate of the Ocean (ECCO) consortium (Stammer et al., 2002). This means that the relative axial angular momentum contributes a even higher proportion to the observed signal in this spectral band contrasted with the annual band. Nevertheless the combined effect only reached an amplitude of $236.2\mu s$ in his study which is about 17 percent smaller than the observed amplitude. He discussed that there are two possible sources for this discrepancy. One is a possible inaccuracy in the reanalysis data itself and another one is the neglect of other effects which were not accounted for. For instance zonal winds above the 10 hPa level were not considered. But only a small part of the difference between the observed ΔLOD can be explained by these zonal winds as this part of the atmosphere roughly contains one percent of the global mass integral. The

hydrology is known to have a measurable effect on seasonal time scales as well
(Walter, 2007).
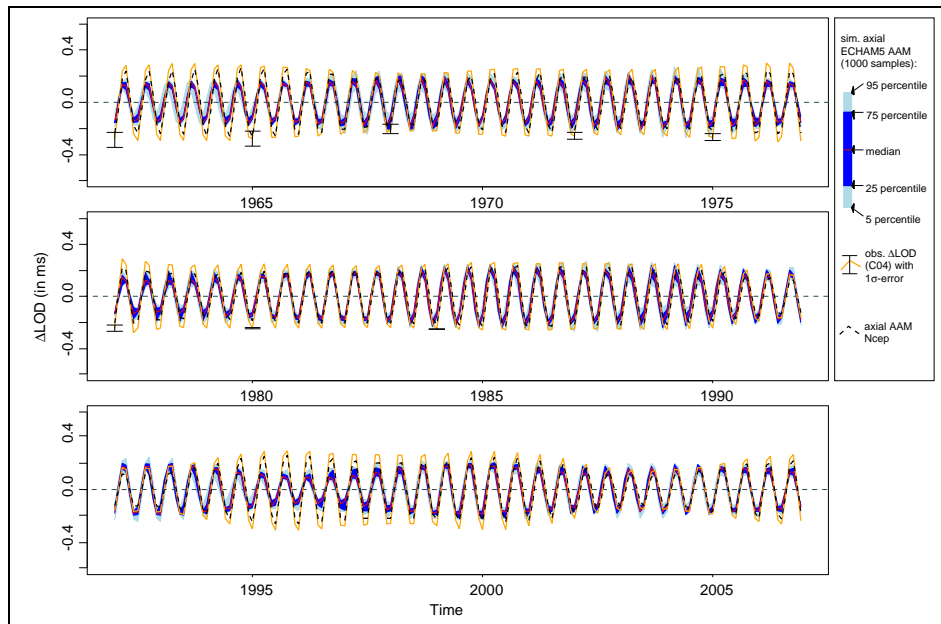
Figure 5.13: Semiannual variations in observed ΔLOD (orange, black error bars
$\pm 1\sigma$), NCEP axial AAM (matter/nonIB+motion) (dashed black) and axial AAM
(matter/nonIB+motion) from ECHAM5 simulations (blue shadings, red line) -
Fourier bandpass filter applied (cut-off frequencies 5.5 and 6.6 month by only
considering Fourier coefficients $c_{81}, \ldots, c_{99}$).

In Fig. 5.13 a bandpass filtered time series of observed ΔLOD and axial AAM
from the ECHAM5 simulation is displayed. The errors of the observed ΔLOD
time series are larger by factor $\sqrt{2}$ as only about half the number of observations
are respected for each time step compared to the annual case. The amplitude
of the observed half year fluctuations is quite large and reaches more than two
thirds of the annual one. One has to distinguish clearly between these two modes
for two major reasons. First of all they don't have the same origin. The global
semiannual mode is primarily driven by semiannual oscillations in the Southern
Hemisphere jet stream, whereas the annual mode is mainly due to an overcom-
pensation of the Southern Hemisphere annual modes in zonal winds by those of
the Northern Hemisphere with maxima in the middle troposphere. This over-
compensation can be explained by a more distinct annual cycle in the Northern
Hemisphere because of the difference in the hemispheric land sea distribution.
Secondly the December January maximum in the annual cycle matches a mini-
mum in the semiannual cycle. This causes two maxima in the combined idealistic

	amplitude ($x_2^{semiann}/\mu s$)	phase (x_3/day)	correlation with obs. ΔLOD $\rho_{obs\hat{LOD}}$
obs. ΔLOD	270	96.2	1
NCEP	218	93.5	0.993
ECHAM5	178	87.1	0.94

Table 5.2: Properties of the semiannual cycle in obs. ΔLOD, NCEP and ECHAM5, confidence levels for the correlation respecting auto-correlation are $\rho_{\alpha=0.05}^{critical} = 0.12$ and $\rho_{\alpha=0.01}^{critical} = 0.157$.

seasonal cycle one in November and the other one in March.

As in the previous section a simple statistical model was fit to the data to estimate characteristic parameters of the oscillation.

$$y(t) = x_1 + x_2^{semiann} cos(\omega t - x_3) \tag{5.23}$$
$$\omega = \frac{2\pi}{\frac{1}{2}y} \tag{5.24}$$

For the semiannual fits the estimated phase shift $\hat{\Delta\phi} = \hat{x}_3^{ECHAM5} - \hat{x}_3^{obsLOD} = -9.1\,days$ is much bigger, with the ECHAM5 time series preceding again (compare table 5.2). Obviously the semiannual variations are more difficult to comprehend in a model sense. Gross descried that a larger part in the semiannual fluctuations is unexplained compared to the annual ones. Stuck could even hardly assign any robust subseasonal variability in the ECHAM3 model. The Gross statement is backed by the results of this particular study as the model fails to describe the whole semiannual variability. This becomes clear by looking at the amplitude ratios. The amplitude ratio of the simulated ECHAM5 AAM and the observed ΔLOD is $\frac{\hat{x}_2^{ECHAM5}}{\hat{x}_2^{obsLOD}} \simeq \frac{178\mu s}{270\mu s} \simeq 0.659$. This result is not very astonishing since the reanalysis data have disclosed the same problems, even though reaching at least more than 80 percent of the observed amplitude in the Gross study which matches the investigations of this work: $\frac{\hat{x}_2^{NCEP}}{\hat{x}_2^{obsLOD}} \simeq \frac{218\mu s}{270\mu s} \simeq 0.807$.

To find out where this lag of variability comes from, different parts of the atmosphere were compared to NCEP reanalysis data in terms of their semiannual zonal wind oscillations. The motivation for this procedure is to reveal regions where the variability is underestimated. The assumption made is that the reanalysis are closer to reality which is valid in this case.
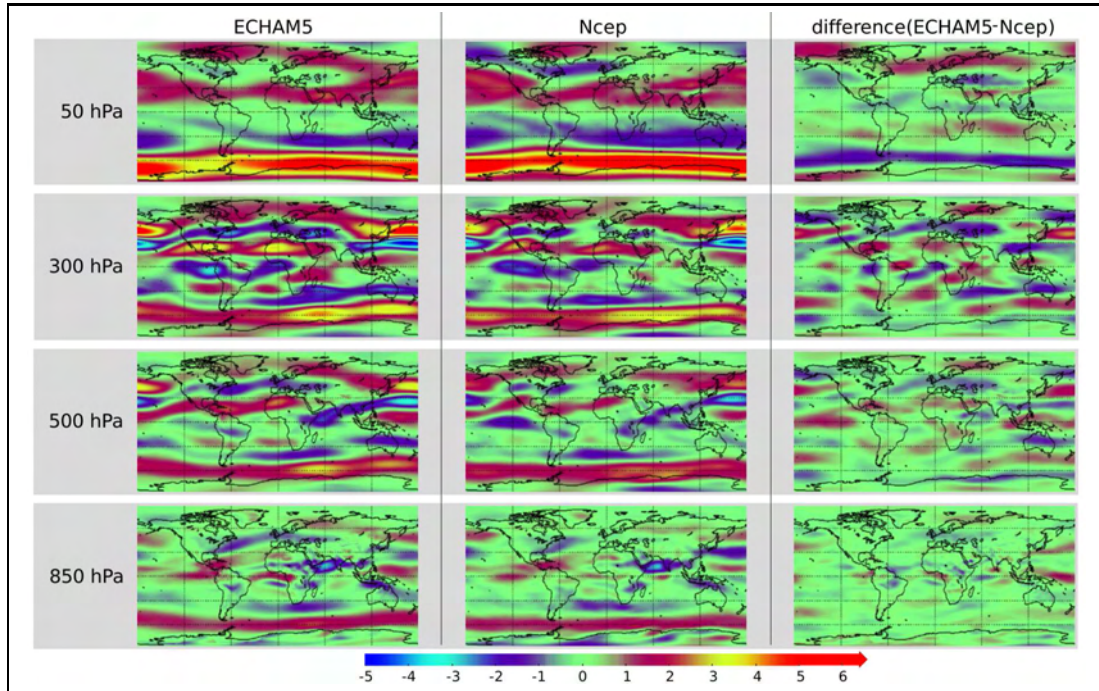
Figure 5.14: Semiannual amplitude $x_2^{semiann}$ in zonal windspeed ECHAM5 simulation ensemble mean (left column), NCEP reanalysis (middle column) and difference ECHAM5-NCEP (right column).

The amplitudes in Fig. 5.14 were calculated by fitting the model (see Eq. 5.23) to the given data. For every single grid point $x_2^{semiann}$ was determined for the reference epoch 1962 to 2006. To cover the whole vertical four representative layers were chosen. The 850hPa level is representing the lower troposphere, the 500hPa level the middle troposphere, the 300hPa level the upper troposphere and the 50hPa level the stratosphere. The patterns in Fig. 5.14 are rather complex and those of the simulations are in a very good agreement with those of the reanalysis data indicating that the semiannuality is generally well comprehended by the model but simply underestimated. Amplitudes in the upper troposphere and stratosphere are high with the strongest semiannuality in the Southern Hemisphere jet stream. The differences between NCEP and ECHAM5 simulation are in the third column. Unfortunately this kind of analysis hardly reveals the lag of semiannual variability in the ECHAM5 simulations. The global integral $\int\int x_2(\lambda, \varphi)cos^2(\varphi)d\lambda d\varphi$ has to be considered. A possible source of underestimation is the Southern Hemisphere jet stream in the stratosphere. In the top right panel a difference of up to 2.5 m/s in the semiannual amplitude of the zonal wind between NCEP and ECHAM5 illustrates a bigger disagreement. As shown for the QBO the stratosphere is only rudimentally described by the

	ANOVA table				
	sums of squares	degrees of freedom	mean squared sums	f-Value	P
factor A	$SSA =$ $2.29 \cdot 10^{-7} s^2$	$DOF_A = a - 1 =$ 89	$SSA/DOF_A =$ $0.26 \cdot 10^{-8} s^2$	$F_A =$ 1.64	$P_A =$ 11.2%
rest	$SSE =$ $5.67 \cdot 10^{-7} s^2$	$DOF_E = a(c - 1) =$ 360	$SSE/DOF_E =$ $0.16 \cdot 10^{-8} s^2$		
total	$SST =$ $7.96 \cdot 10^{-7} s^2$	$DOF_T = ac - 1$ 449			

Table 5.3: ANOVA table of semiannual amplitudes from five ensemble runs for
the 1962 to 2006 period.

ECHAM5 model. Glowienka-Hense (1999) demonstrated that only a small proportion of the semiannual oscillation (SAO) of the Southern Hemisphere MSLP
can be explained by prescribed boundary conditions. A significant boundary
effect on SAO was only seen in the tropics and parts of the subtropics, thus
the SAO results from internal variability to a large extent. Therefore a perfect
agreement in time between the simulations and observations can not be expected.

A one-way ANOVA (as introduced in section 2.1.14) is performed to analyse
the variance of the semiannual cycle. For this purpose the amplitude $x_2^{semiann}$ of
every semiannual cycle is considered for the 1962 to 2006 period and for every
ensemble member. Referring to the notation in section 2.1.14 the ANOVA model
can be expressed by

$$\mathbf{X}_{ik} = \mu + \alpha_i + \epsilon_{ik} . \tag{5.25}$$

Index $i = 1, \ldots, a$; $a = 90$ terms the number of the semiannual cycle from
1962 on and index $k = 1, \ldots, c$; $c = 5$ denotes the number of the ensemble member run. Such an ANOVA design allows to partitionate the variance in a part
which is common to all runs — treated as externally driven by boundary conditions — and a part which is "special" to a certain run — treated as internally
driven.

Table 5.3 shows the results from the ANOVA of semiannual amplitudes. The
explained proportion of variance explained by boundary conditions P_A is very
small. Only 11.2 percent of the total variance can be explained by imposed
boundary conditions, the rest of the variance emerges from internal mechanisms.
Therefore a good agreement in time between the model and the observations
concerning the semiannual amplitude can not be expected. This is subject of the

	ann. amplitude $(x_2^{ann}(t))$	semiann. ampl. $(x_2^{semiann}(t))$
obs. ΔLOD $(\hat{\rho}_{obsLOD,solconst})$	0.569	-0.631
NCEP $(\hat{\rho}_{NCEP,solconst})$	0.666	-0.618
ECHAM5 $\hat{\rho}_{ECHAM5,solconst}$	0.172	0.235

Table 5.4: Estimated correlation of annual/semiannual amplitudes of observed ΔLOD, NCEP and ECHAM5 with solar constant; confidence levels for the annual case are $\rho_{\alpha=0.1}^{critical} = 0.621$ $\rho_{\alpha=0.05}^{critical} = 0.707$ and for the semiannual case $\rho_{\alpha=0.1}^{critical} = 0.549$ and $\rho_{\alpha=0.05}^{critical} = 0.632$ respectively.

following section.

5.2.3 Interannual Variability of Seasonal and Semiannual Amplitudes in AAM

Referring to Fig. 5.12 and Fig. 5.13 a pronounced interannual or decadal variability in the annual and semiannual amplitude particularly in the observed values is revealed. The speculation that this interannual variability is to some proportion caused by according fluctuations in the solar constant is investigated in the following.

The magnitudes of the semiannual and annual amplitudes have been plotted in Fig. 5.15 besides the annual/semiannual means of the solar constant. As already determined the annual amplitudes are bigger compared to the semiannual ones. NCEP and ECHAM5 are overestimating the amplitudes in the annual case but underestimating the semiannual case. A table of estimated correlation coefficients of ΔLOD with the solar constant time series based on the underlying data of Fig. 5.15 is presented (see table 5.4).

Quite high positive correlations with annual means of the solar constant are determined in the annual amplitude time series of the obs. ΔLOD and NCEP AAM - with the NCEP being significant at the 90 percent confidence level. The number of eight equivalent realisations for the annual case is very small. The statistical relation could not at all be reproduced by the ECHAM5 model due to internal variability.

The semiannual amplitudes of ΔLOD and NCEP AAM are highly anticorrelated with the semiannual means of the solar constant. This fact again points at different origins of the two oscillations. Both anticorrelations are significant at

the 90 percent confidence level and not significant at the 95 percent level. The
number of equivalent realisations was estimated by ten.

The sun drives the thermal balance of our planet and determines the seasonal
weather cycles. A possible physical mechanism to drive the ΔLOD oscillations
would be an intensified seasonality in all meteorological parameters by a strength-
ened irradiation. This would be very plausible in a physical sense. On the other
hand this explanation fails to describe the anticorrelation for the semiannual
oscillations. This is a new research point brought up by this work which needs
further consideration. A more robust affirmation of a statistical relationship can
be achieved when the high quality C04 and NCEP datasets cover a bigger time
span. A deeper look into the past is not worthwhile in these studies since partic-
ularly the low quality of any time series before 1962 would decrease confidence in
the results. State-of-the art models are not capable to originate any interannual
variability in annual/semiannual amplitudes which show significant correlations
to those of the observations, because as shown in the previous section the size of
the semiannual amplitude is mainly determined by internal processes.

A lot of authors studied the direct statistical relation between the solar con-
stant and AAM. Robust signals could be obtained explaining some of the inter-
decadal variability in the observed ΔLOD time series (e.g. in recent years: del
Rio et al. (2000, 2003); Han et al. (2002)) where a local maximum at 11 year
periods can be seen in the power spectrum.

5.3 ANOVA of Simulated Axial AAM

In the previous chapter a thorough frequency analysis of simulated axial AAM
was performed. The basic assumption made was that the axial AAM time series
data consist of signals and red noise. Signals were treated as a superposition
of harmonic oscillations with characterising amplitudes, frequencies and phases.
Some hidden signals were revealed by reducing noise such as in the case of teran-
nual and quadrannual oscillations. Some of the signals have been identified and
assigned to physical processes.

Now a somehow different approach will be introduced. The goal of this study
is to first of all clearly identify internal and external variability within simulated
axial AAM. As demonstrated the variance of the motion part is dominating the
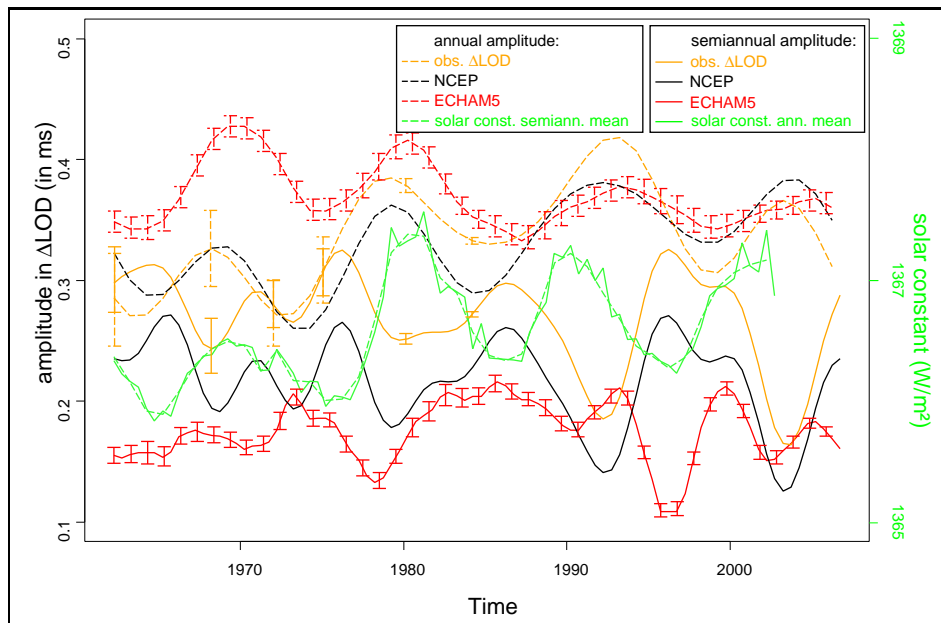
Figure 5.15: Time series of annual (dashed) and semiannual (solid) amplitude in observed ΔLOD (orange), NCEP (black) and ECHAM5 ensemble mean (red), solar constant annual (solid green) and semiannual mean (dashed green), amplitudes were calculated by least square fitting Eq. 5.23 to semiannual/annual subsets respectively, error bars illustrate $\pm 1\sigma$.

one of the matter part. The ANOVA study is confined to the motion term, therefore only the relative axial AAM will be treated. So the question has to be answered what ratio of the overall variance in the simulated relative axial AAM can be explained by external boundary conditions of the model runs? Secondly long term interdecadal trends in the simulated relative axial AAM should be revealed - also by applying an ANOVA technique - and the question to what extent they originate from different boundary conditions will be solved.

To reveal the spatial distribution of simulated axial AAM densities every grid point's AAM density is considered. The AAM density at a particular grid point is determined by the vertical integral illustrated in Fig. 5.16. Note that the global integral to calculate the relative atmospheric angular momentum $h_z^{AAMmotion}$ contains a squared cosine-factor $cos^2(\varphi)$, one reflecting the distance to the rotation axis and the other the size of the grid box area. For the AAM density only one cosine-factor is considered for the distance to the rotation axis and not that one taking into account the size of the grid box area. This means that $\rho^{AAM}(\lambda, \varphi)$ of grid points close to the equator still contributes a bigger share to the globally integrated AAM due to a larger grid box area which they represent. Contrary
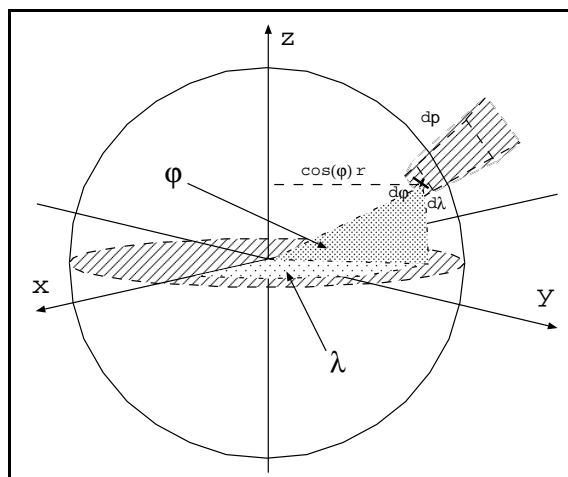
Figure 5.16: Schematic representation of the AAM density per grid box area.
$\rho^{AAM}(\lambda, \varphi) = \int_{p=0}^{p_0=1013.25hPa} \frac{u(p,\lambda,\varphi,t)}{p_0(\lambda,\varphi,t)} \, cos(\varphi) \, dp.$

to the globally integrated $h_z^{AAMmotion}$ values, the integration is carried out on
pressure levels which allows for a higher comparability since the orography has a
minor effect on the local AAM density $\rho^{AAM}(\lambda, \varphi)$. Referring to chapter 2.1.14
the AAM density $\rho^{AAM}(\lambda, \varphi)$ is the indicator variable in the following. In recent
years ANOVA methods became more popular in the field of meteorology and
climatology. An important reason is the ability of conducting many experiments
by increased computational power. Those experiments may differ for instance in
initial conditions, parameter settings, boundary conditions or computer architec-
ture. After the construction of a skillful experimental design ANOVA provides
a powerful tool for analysing sources of variance.

5.3.1 Analysing Internally and Externally Driven AAM Variability Through a one-way ANOVA

The conceptual design of the ANOVA is mostly drawn on the works of Zwiers
(1996) and Storch and Zwiers (1999). Keeping the necessary assumption for
performing an ANOVA of a constant mean in mind a very early part of the sim-
ulation period was chosen (1893-1912). Under these more or less preindustrial
circumstances an externally induced trend is less likely compared to present con-
ditions. The division into separated seasons is also done concerning the annual
and semiannual cycle of axial AAM:

- DJ - December/January mean coinciding with the annual maximum and
  semiannual minimum

- MA - March/April mean coinciding with the semiannual maximum

- JJ - June/July mean coinciding with the annual minimum and semiannual
  minimum

- SO - September/October mean coinciding with the semiannual maximum

The 11th, 12th and 13th coefficient of the auto-correlation function of the
global axial AAM monthly mean time series have shown close to zero values,
thus the requirement of temporal independence is well satisfied.

Figure 5.17 illustrates the proportion of total variance P_a explained by im-
posed boundary conditions. P_a is often called by the simple term "explained
variance", it is avoided in this context as it comes from linear regression which
is a different approach than ANOVA. The rest of the variance can be seen as in-
ternal variance caused by weather noise. The dark red contour lines indicate the
mean AAM density $\rho^{AAM}(\lambda, \varphi)$. The strongest AAM densities are found at mid
latitudes in winter. Due to the $cos(\varphi)$ factor in the AAM density $\rho^{AAM}(\lambda, \varphi)$ re-
specting the distance to the Earth rotation axis, high latitudes do not contribute
a large AAM proportion to the global AAM. The effect of the combined solar,
aerosol, greenhouse gas and SST/SIC forcing has been tested. It is impossible
to differentiate between effects originating from a particular kind of forcing (e.g.
greenhouse gas) due to the design of the model experiment which is reflected
in the ANOVA. Only a design where experiments of every possible forcing com-
bination were conducted would allow to clearly differentiate between particular
forcing factors. Unfortunately the CPU consumption of such an experiment
would overrun the licenced CPU time by far.

The most prominent feature in these four diagrams is the broad band of very
large P_a values in the tropics where boundary forcing is expected to dominate
because natural interannual variability from internal chaotic variability is known
to be weak. In this domain up to 70 percent of the simulated interannual vari-
ability can be explained by forcing factors. Interestingly not only the Central
Pacific region but also the tropical Atlantic region indicates strong peaks in the
spatial distribution. Notably in June/July the proportion reaches values of up
to $P_a = 0.7$ in a band from the tropical West African coast to the Northeast
Brazilian coast. At large, over land values are lower which is due to a less effec-
tive SST forcing. The pronounced variability in the SST forcing in the ENSO 3.4
region vastly exceeds the variability in the tropical Atlantic. Figure 5.5 didn't
show any significant correlations between the 2m temperature and globally in-
tegrated axial AAM for this region. Since aerosols are not very likely to have a

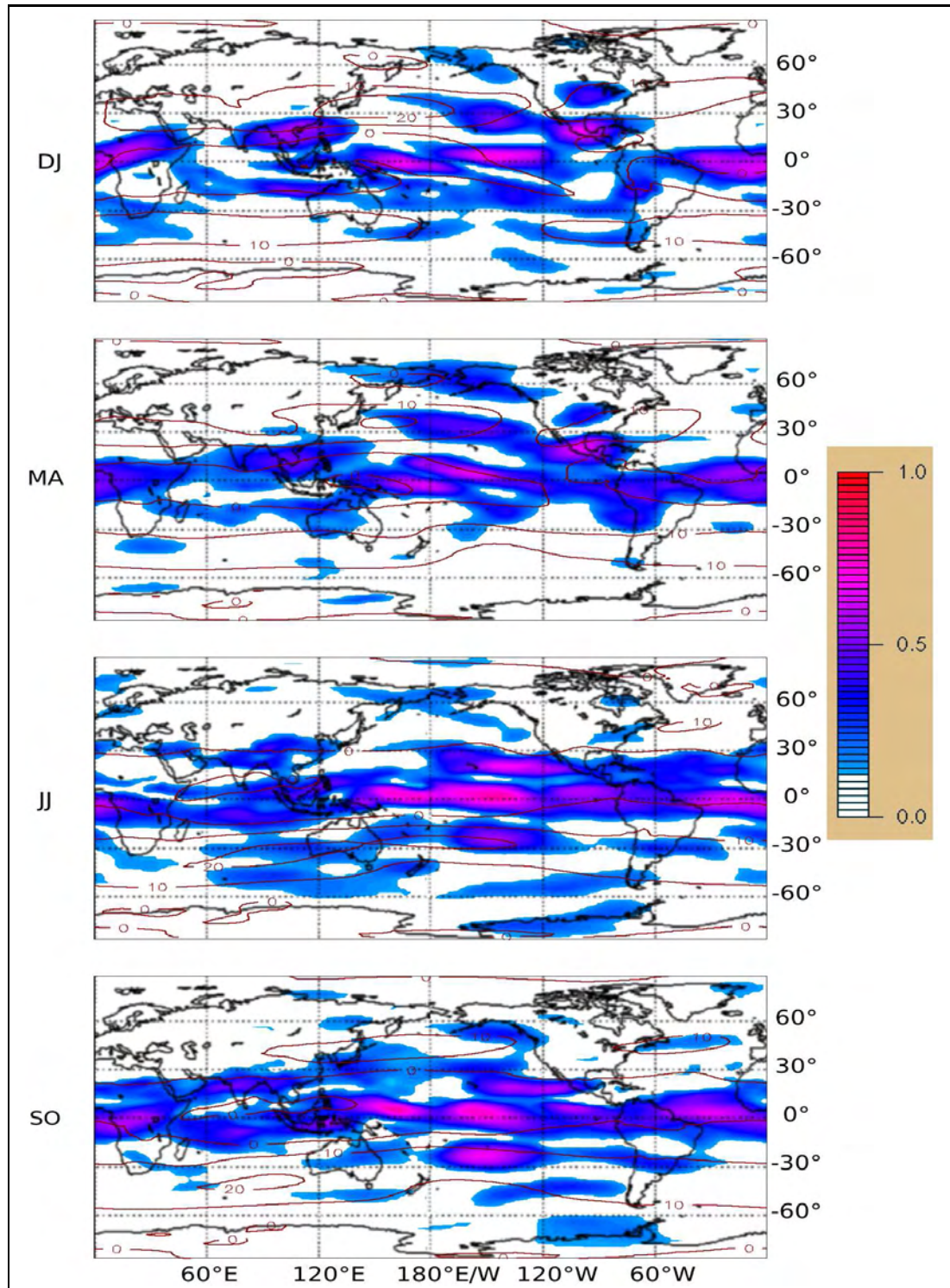Figure 5.17: Proportion of total variance P_a of AAM density $\rho^{AAM}(\lambda, \varphi)$ explained by imposed boundary conditions for the 1893 to 1912 period; the F-test resulted in a critical proportion of 0.1211 at the five percent significance level (lower values were whitened in the map). Contour lines (dark red) indicate mean AAM density $\rho^{AAM}(\lambda, \varphi)$ for the 1893 to 1912 period.

huge impact on the local AAM density and SST variability is fairly low in the
tropical Atlantic, it seems that the local AAM density is very sensitive to the
SST forcing in place.

Apparently there additionally exist two weaker bands of intense proportions
around the globe one north and one south of the equator band. The Pacific
domain is covered with a kind of wave structure in north-south direction. At
some locations the patterns are organised to a weak third band.

Differences in the proportion of total variance P_a explained by imposed bound-
ary conditions can be seen from season to season. The June/July and Octo-
ber/November diagrams tend to slightly higher values compared to the other two
diagrams. At this point the statistical significance of possible seasonal differences
is not tested, that's why the seasonal aspect should not be misinterpreted.

5.3.2 Analysing Internal and External Sources of Possible Long-term Trends in AAM Through a Two-way ANOVA

Now another design of an ANOVA will be presented. For the objectives of this
research a two-way ANOVA (as in chapter 2.1.14) seems well suited. As the
headline suggests long term interdecadal trends in local relative axial AAM will
be analysed. The data generation of the local AAM densities was already demon-
strated in the previous section.

The motivation for the analysis presented in this chapter follows from the fact
that a significant long term trend in the ECHAM5 axial AAM has been found
for the 1974 to 2003 period on the one percent level.

A trend estimation was done in Fig. 5.18 for the last three decades (1974 to
2003) for the ECHAM5 and NCEP data. For comparability reasons an early
period in the ECHAM5 data has been added as well. The trend estimation is
done for every ensemble member. The results from all five members are summed
up and weighted with 0.2 each. The uncertainty of such a single trend estimation
is respected in the results, because each member's trend is treated as a gaussian
random variable. The trend of the ensemble mean therefore is represented in a
simple gaussian mixture model.

The large uncertainty of the NCEP trend estimation is striking. Probably the
trend estimation's confidence is underestimated, because only the seasonal cycle
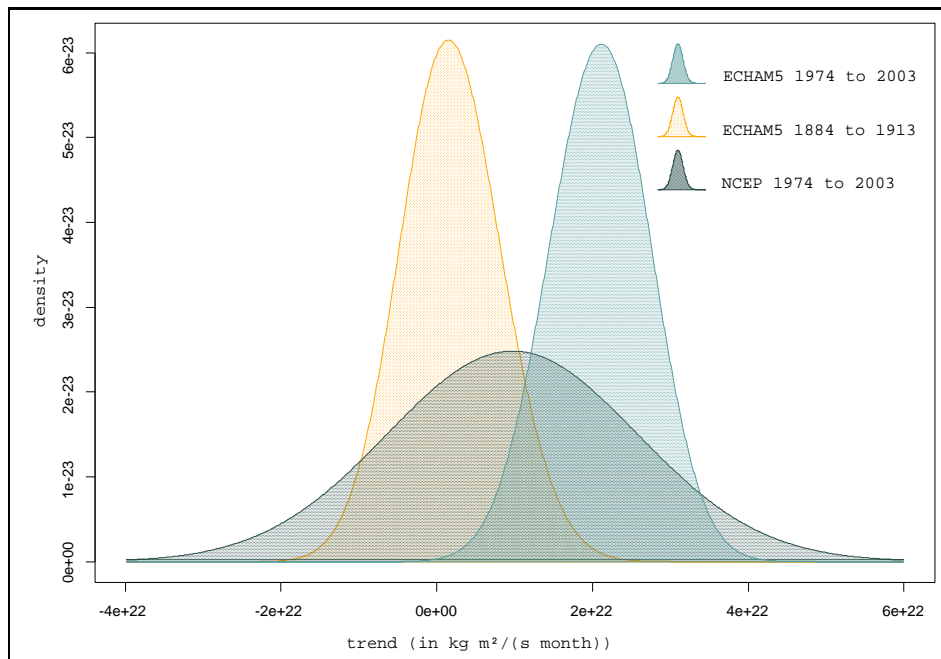
Figure 5.18: Estimated pdf of 30 year linear trends in global axial AAM.

has been removed from the time series by a LOESS fit. As already discussed the time series contain interannual oscillations (ENSO, etc.) which result in big residuals from the linear trend estimation and make the uncertainty large. For ECHAM5 five independent realisations are at hand, the uncertainty of the trend estimation is reduced remarkably.

The NCEP trend tends to positive values but is far from being different from zero on any common significance level. On the other hand ECHAM5 produces stronger trends accompanied by less uncertainty leading to a significant positive trend on the one percent level. The difference in the mean is an interesting feature as it indicates that 21st century scenario runs might generate overconfident trends in AAM.

To adapt the data to an ANOVA scheme facilitating the discovery of sources of long term interdecadal trends, the variance of decadal trends has to be considered. This data preprocessing is analogous to the analysis of interannual variance in the previous chapter, where the underlying data set consisted of one year time steps.

A trend estimation was done in Fig. 5.19 for the last three decades (1974 to 2003) and for every ensemble member. Similar to the procedure for the global
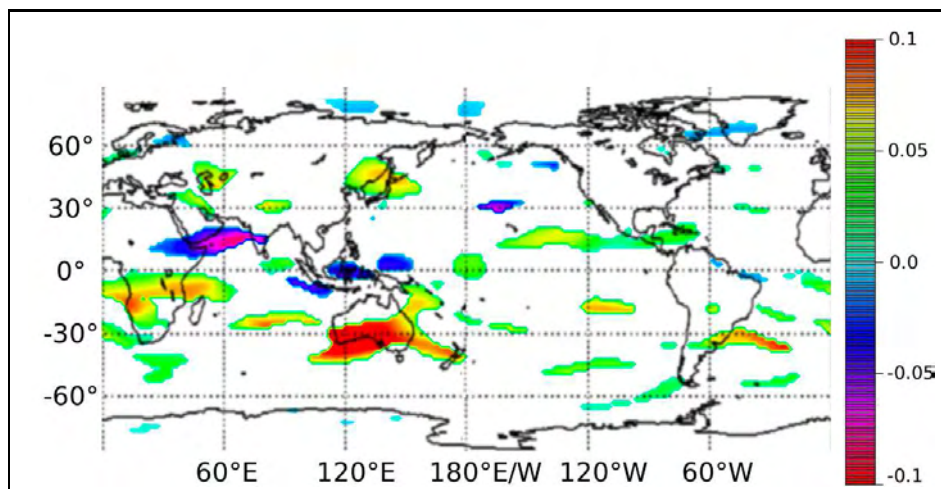
Figure 5.19: Trends of the ensemble mean's local AAM density $\rho^{AAM}(\lambda, \varphi)$ for
the 1974 to 2003 period (in $m/s\ 1/y$), only trends above the 95 percent confidence
level are displayed.

AAM shown in Figure 5.18. Only grid points where the cdf of the gaussian mix-
ture model has the same sign for the 5 and 95 percentile were regarded to be
significantly different from zero at the 95 percent confidence level.

Although there is a significant positive trend in the global AAM of the
ECHAM5 simulation during this epoch, there's hardly evidence from the spatial
point of view. The areas which show a significant trend cover a rather small
proportion of grid points, keeping in mind that the trends are tested on the
five percent significance level it could be a matter of pure chance. Atmospheric
GCM scenario runs indicate an intensification of westerlies at mid-latitudes for
the 21st century especially for the Southern Hemisphere (de Viron et al., 2002;
Winkelnkemper et al., in Press). An intensification in recent decades is not
backed by the 20c simulation carried out, as the trends don't seem to be very
robust in a statistical sense.

As already alluded the distinction between particular forcing factors is impos-
sible due to the limited extent of the model experiments, but on the other hand
solar and greenhouse gas forcing are more important for long term fluctuations
than for high frequency ones. The question arises: How effective are the imposed
boundary conditions in generating interdecadal trends?

To handle this question the data is split into 12 decades covering a period
from 1883 to 2003. For each decade the linear trend is estimated by applying a

least square fit. As indicator variable 12 independent realisations of a 10 year
linear trend are considered. The notation from chapter 2.1.14 is used here.

$$
i = \begin{cases}
1 & \text{for } \text{runA} \\
2 & \text{for } \text{runB} \\
3 & \text{for } \text{runC} \\
4 & \text{for } \text{runD} \\
5 & \text{for } \text{runE}
\end{cases}
\tag{5.26}
$$

$$
j = \begin{cases}
1 & \text{for } \text{trend of decade 1} \\
2 & \text{for } \text{trend of decade 2} \\
\ldots & \ldots \quad \ldots \\
12 & \text{for } \text{trend of decade 12}
\end{cases}
\tag{5.27}
$$

$$
k = \begin{cases}
1 & \text{for } \hat{a} - \sigma_{\hat{a}} \\
2 & \text{for } \hat{a} \\
3 & \text{for } \hat{a} + \sigma_{\hat{a}}
\end{cases}
\tag{5.28}
$$

Note that the indicator variable $\mathbf{X}_{\text{ij},k=2}(\lambda, \varphi)$ is represented by the estimated
slope of the trend line $\hat{a}$ for the local AAM density $\rho^{AAM}(\lambda, \varphi)$ and the un-
certainty of the estimation is added $(\mathbf{X}_{\text{ij},k=1}(\lambda, \varphi))$ or subtracted $(\mathbf{X}_{\text{ij},k=3}(\lambda, \varphi))$.
This concept of the ANOVA provides sufficient information for examining the
effect of two explanatory variables (simulation effect and boundary effect due
to imposed boundary conditions) on the indicator variable (local AAM density
$\rho^{AAM}(\lambda, \varphi)$).

The model used treats some effects as fixed and others as random (like in
chapter 2.1.14):

$$
\mathbf{X}_{\text{ijk}} = \mu + a_{\text{i}} + b_{\text{j}} + c_{\text{ij}} + \epsilon_{\text{ijk}}
\tag{5.29}
$$

Remember: a_i is the effect common to all years that is identified with simulation
i. Here this effect is called the "simulation effect" and assumed to contain both
deterministic and random components $a_i = \alpha_i + \gamma_i$ — with γ being a zero mean
Gaussian random variable. The simulation effect contains the chaotic dynamical
effects of the initial conditions. Natural internal variation between simulations
$i = 1, \ldots, 5$ is expected to be existent. Whether the choice of initial conditions
induces significant decadal trend variability in the simulations will be tested. At

this point the null hypothesis that there is no simulation effect can be formulated:

$$H_{0_A} : a_i = \sigma_a^2 = 0, \ \forall \ i \tag{5.30}$$

against the alternative hypothesis that there is an effect.

The boundary effect is embodied by b_j, it is a fixed effect because every simulation was forced with the same data dictated by the boundary conditions. Hence, b_j denotes the deviation from the overall mean μ which is common to all simulations $i = 1, \ldots, 5$ and identified with decade $j = 1, \ldots, 12$. It will be referred as the "boundary forced effect" or simply "boundary effect" because its source is presumed to be in the external boundary conditions. It is supposed to be entirely determistic as the prescribed conditions are common to all decades.

The second null hypothesis to be tested is that there are no boundary forced effects on the decadal trend variability present in the simulations. The translation of this null hypothesis considering the ANOVA assumptions looks as follows:

$$H_{0_B} : b_j = 0, \ \forall \ j \tag{5.31}$$

Against the alternative hypothesis that there is a boundary induced effect common to all simulations. A much simpler one-way ANOVA design would enable to test the boundary effect as well, the test of the simulation effect is additionally carried out to ensure that the initialisation procedure did not affect the long term variability in the model.

The mixed effect is as well tested. The according null hypothesis states that only random variations are present if simulation and boundary effect are respected.

In Figure 5.20 the F-ratios for both the simulation and boundary effect are illustrated. As expected the null hypothesis H_A is accepted in most cases. The few rejections are carried out on the 10 percent level which should enable 10 percent of the grid points to be rejected by chance. The 10 percent level is traditionally preferred when applying an ANOVA technique. The areas with a significant simulation effect cover even less than 10 percent of the grid points which leads to the reasoning that there is not a significant effect from the initialisation of the ensemble member on the decadal trend variability in the local axial AAM density $\rho^{AAM}(\lambda, \varphi)$ in general. The mixed effect doesn't show any clear patterns and does not contribute to the variations significantly for the vast
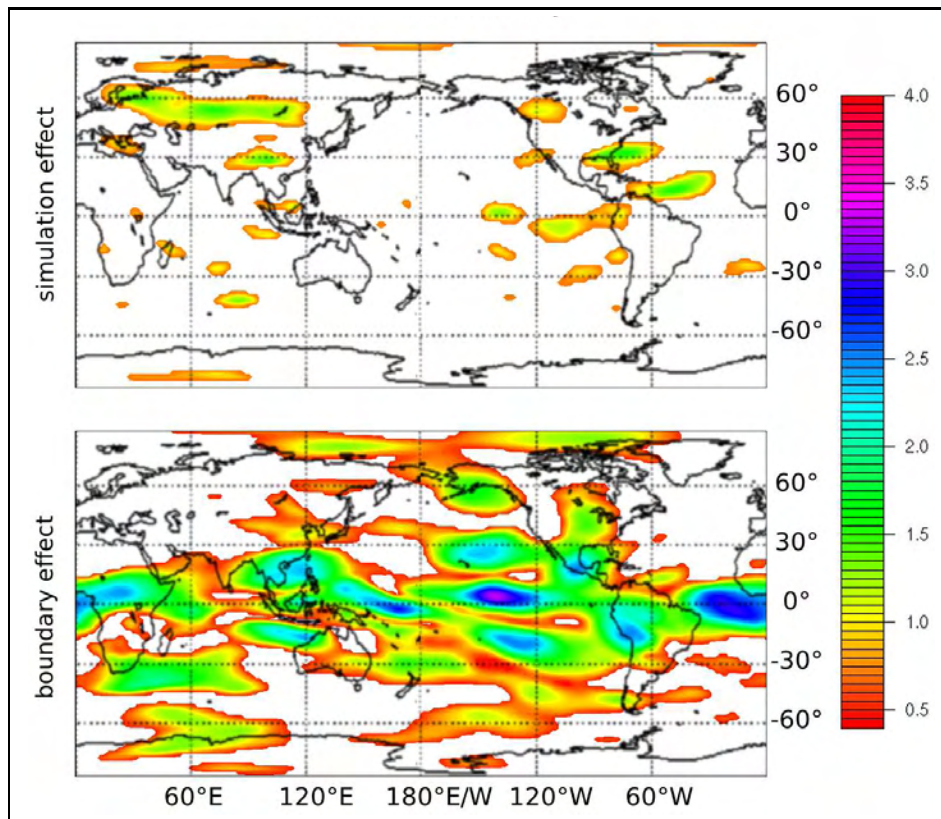
Figure 5.20: Natural logarithm of the F-ratios for the simulation (top) and
boundary effect (bottom) on variations in decadal trends of local AAM den-
sity. Values which are not significantly greater than 0 (equivalent to F-ratio
greater than 1) on the 10 percent significance level are not shaded.

majority of grid points.

For the external boundary effect things look rather different. Nearly half of
the grid points show significant boundary effects on the decadal trend variability
of the local axial AAM density $\rho^{AAM}(\lambda, \varphi)$. Once again as in the previous chap-
ter it seems that ocean grid points are affected to a bigger proportion than land
grid points which points either at an effective forcing by SST or at the fact that
temporal internal variability is reduced within the boundary layer — containing
about 15 percent of the vertical mass integral — for ocean grid points. Another
interesting feature can be found in the North Atlantic region. A lot of scientific
articles have been issued in recent years on a possible enforcement of westerlies
by a changing climate in this region. This statement is not at all backed by
the results here. It is noticeable that the only region where the boundary effect
does not significantly influence trend variability is the North Atlantic European

domain.

It is remarkable that patterns from the previous section of the boundary effect
on interannual variability (compare Fig. 5.17) and those on the variability on
decadal trends resemble. Obviously a clear dependence of the explained variance
on certain time scales does not exist. Nor a distinction of the effectiveness of
forcing factors is suggested by time scale. Presumably the SST forcing is effective
on a lot of time scales which avoids any determination of different forcing factors.

5.4   Equatorial AAM

In the previous chapters the structure of the axial AAM component within the
ECHAM5 simulations was deeply analysed. Here an analysis of the equatorial
components (χ_1, χ_2) will follow referring to appendix D. As for the z-component
the χ-functions directly reflect the AAM_x^{matter}, AAM_x^{motion}, AAM_y^{matter} and
AAM_y^{motion} terms.

$$
\begin{aligned}
AAM_x^{matter} &= (C-A)\,\chi_1^{matter} & (5.32)\\
AAM_x^{motion} &= \Omega\,(C-A)\,\chi_1^{motion} & (5.33)\\
AAM_y^{matter} &= (C-A)\,\chi_2^{matter} & (5.34)\\
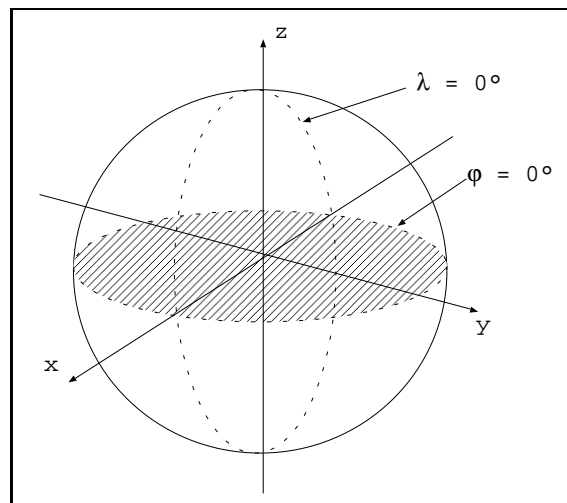AAM_y^{motion} &= \Omega\,(C-A)\,\chi_2^{motion} & (5.35)
\end{aligned}
$$

Figure 5.21: Schematic representation of coordinate systems, $\vec{x}$ and $\vec{y}$ lie in the
equator plane (shaded) and build an orthonormal basis with $\vec{z}$.

Some restrictions to the analysis of the equatorial AAM-components have
to be mentioned. The effect of these components to the solid Earth results in
polar motion (movement of Earth's rotation axis across its surface). The oceanic
(non-tidal) effects on polar motion have the same order of magnitude than the at-
mospheric ones and superimpose AAM-effects on seasonal to decadal time scales.
Concerning the seasonal time scale hydrologic effects have a strong impact on
polar motion as well. As an implication atmospheric AAM-effects can not di-
rectly be extracted from geodetic observations of polar motion as already done
within this work for the axial components after some minor assumptions. As the
geodetic reference doesn't stand by, reanalysis data form the only reference for
this chapter.

5.4.1 Equatorial AAM variability

As will be seen later both components (AAM_x and AAM_y) have a connatural
structure but they are quite different in detail. One important aspect is the
difference in land-sea distribution. The grid points which have the strongest in-
fluence on the x-component are found at the "equator" of vector $\vec{x}$. The equator
of vector $\vec{x}$ is equal to the $90°E$ and $90°W$ meridians in the geographic coordinate
system, whereas the equator of vector $\vec{y}$ is identical to the $0°$ and $180°$ meridi-
ans. Within the ECHAM5 model the land-sea ratio is 0.426 along the equator
of vector $\vec{x}$ and just 0.244 for vector $\vec{y}$. This fundamental difference makes clear
that AAM_y is to a larger proportion affected by ocean grid points compared to
AAM_x where grid points over Asia and America are weighted much higher (see
appendix D for the exact weighting terms).

Fig. 5.22 outlines the WPS in the interannual domain. The ensemble mean
of the ECHAM5 simulations shows only very diffuse signals which are situated
in the ENSO band. As a consequence only weak energies around the year 1970
and early 1990s can be assigned to ENSO in case of ECHAM5. The ENSO
phenomena is very effective in exciting oscillations in the axial component but
on the other hand hardly contributes to variations in the equatorial component.
The NCEP reference is rather similar in its overall structure. As ECHAM5, it
does not exhibit any significant energies at the five percent level.

A good agreement to the NCEP based x-component of the AAM can be seen
at periods of 10 to 12 years in the late 1970s, 1980s and 1990s accompanied by
a significant coherence in the late 1980s. Concerning phase NCEP and ECHAM

Figure 5.22: Wavelet power spectrum (WPS) of AAM_x for NCEP (top left) and
for ECHAM5 ensemble mean (bottom left), joint wavelet coherence (top right)
and phase diagram (bottom right). Five percent significance level is indicated
by a black contour line. Energies are standardised by maximum energy.

are quite synchronous in this domain and very noisy in others. Encouraged by
the agreement for periods between 8 and 12 years, it is dwelt on this topic.
A possible external source of these variations — solar variability — is added to
Fig.5.23 where band pass filtered time series of the x-component of the simulated
equatorial AAM is plotted.

A remarkable spread of the 1,000 bootstrap realisations is obvious in this
spectral band (8 to 14 years) demonstrating that equatorial components con-
tain more relative noise than the axial ones. The pronounced sunspot cycle
around 1980 — sunspot cycle number 21 — is accompanied by a pronounced
fluctuation in the equatorial AAM. Apparently the decadal fluctuations of sim-
ulated AAM_x^{ECHAM} are forced by solar variability. The correlation coefficient
for the 50th percentile of AAM_x^{ECHAM} and the solar irradiance is estimated
by $\hat{\rho}_{AAM_x^{ECHAM}, I(sun)} = 0.615$ and is highly significant on the one percent level
$\rho_{\alpha=0.01}^{critical} = 0.372$.

For Fig. 5.24 the same wavelet analysis like for Fig. 5.22 has been carried
out. The four panels cover annual and subannual periods. As for the ECHAM5
ensemble mean the annual signal in NCEP dominates. The distribution of the
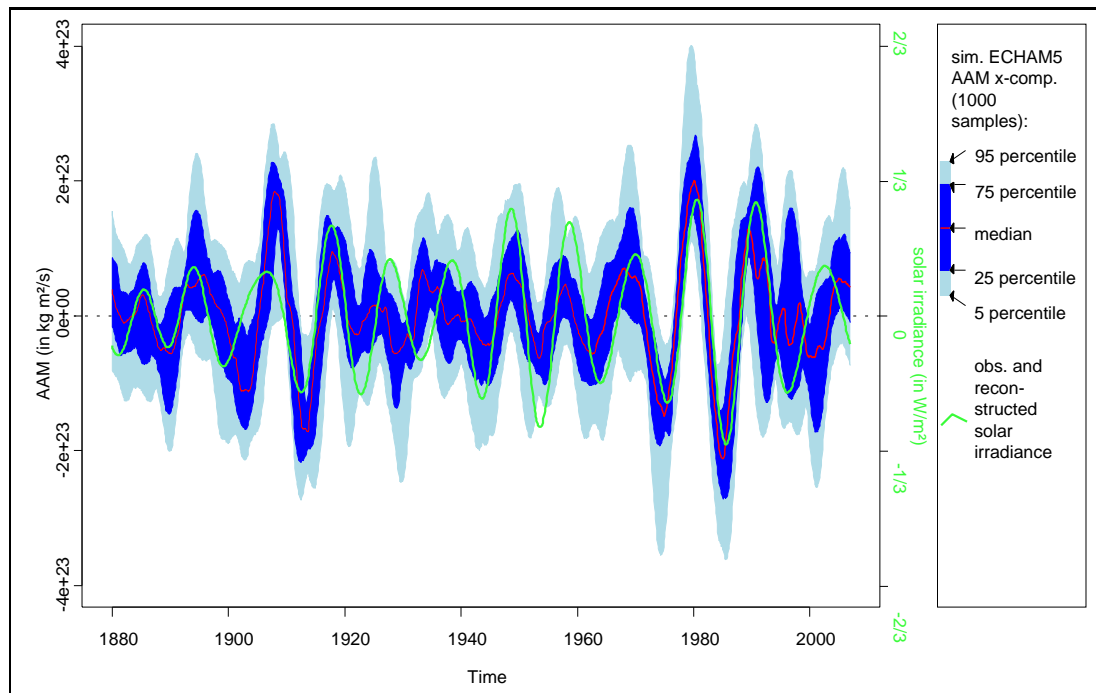
Figure 5.23: Time series of simulated AAM_x^{ECHAM} (blue shadings, red line) and
solar irradiance (green curve) as defined as boundary condition for the model
experiment (8 to 14 year band pass filtered).

energy density of the annual signal is less homogeneously distributed in time in
case of NCEP. A tendency to higher values since the year 1980 is conspicuous
supposing that the introduction of new remote sensing techniques allowed for
more accurate assimilation results. The improved accuracy from 1980 on has
optimised the signal to noise ratio leading to a stronger annual signal. Some
energies drip off to higher frequencies with shorter periods. Some significant en-
ergy spots are situated at half year periods. The structure of the annual signals
is much smoother in case of ECHAM where also some semiannual signal emerge.
The annual signal and some "drip-offs" to shorter periods are present and sig-
nificant in the wavelet coherence, a small phase shift with preceding NCEP time
series can be deduced from the phase diagram.

In general the y- or χ_2-component shows fewer signals which can be reas-
signed to certain excitation mechanisms (see Fig. 5.25). As for the x-component
the annual signal is most striking, other interannual signals are visible. In the
interannual domain no significant oscillations are found either in NCEP nor in
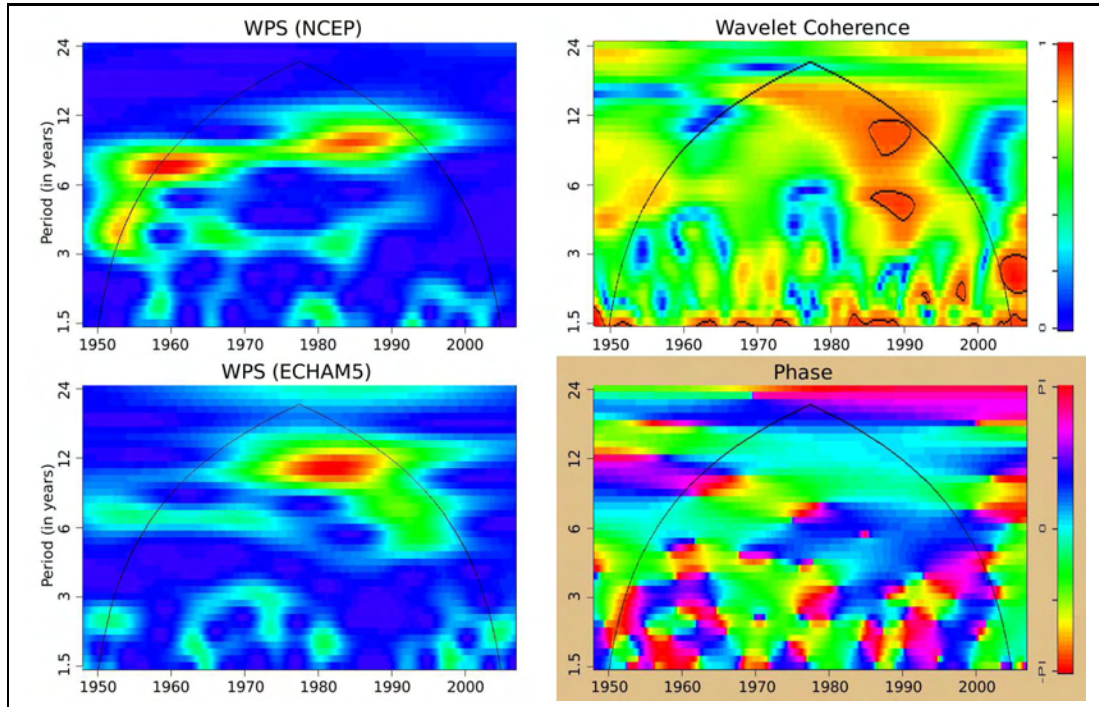ECHAM5.
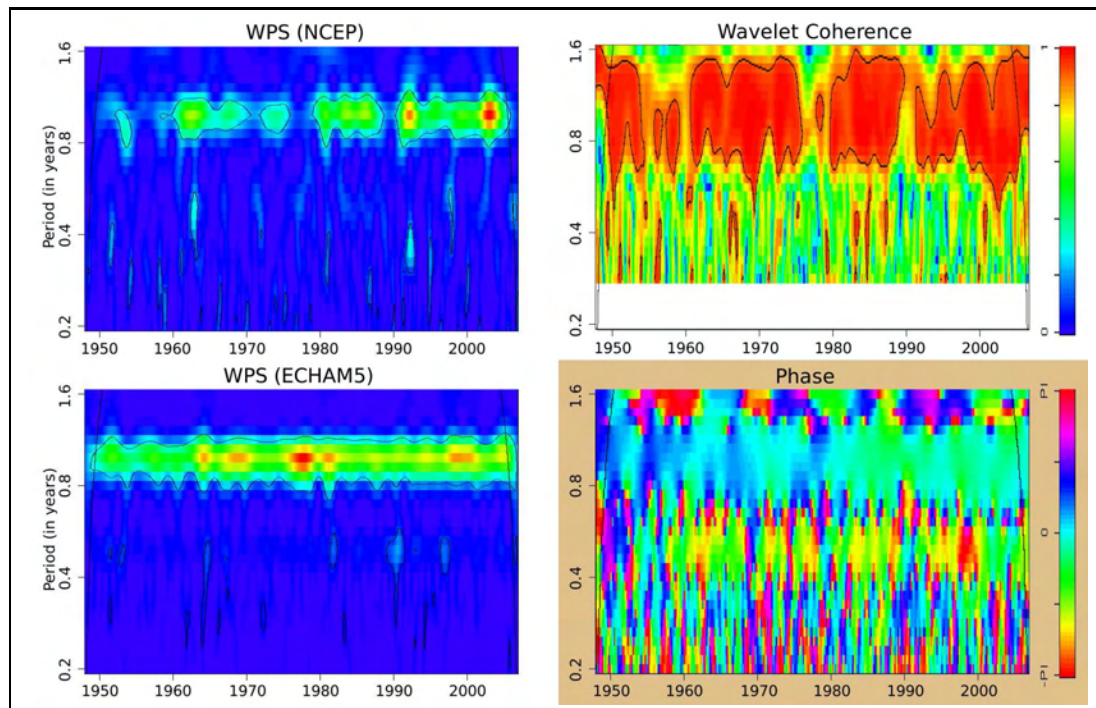
Figure 5.24: Wavelet power spectrum (WPS) of AAM_x for NCEP (top left) and
for ECHAM5 ensemble mean (bottom left), joint wavelet coherence (top right)
and phase diagram (bottom right). Five percent significance level is indicated
by a black contour line. Energies are standardised by maximum energy.

But some stronger interdecadal variability is indicated at least in the first
half of the time span which is possibly linked to the "El Viejo - La Vieja" mode
in the Central Pacific - also called "Sardine Regime - Anchovy Regime". This
mode is supposed to be a superior ENSO mode with periods of about 25 years
(Chavez et al., 2003) [2]. It is a current research topic and due to the comparably
short coverage of reliable data in the region it is heavily debated. A time span
of roughly 60 years means just a realisation of two to three complete cycles.
At this point it is alluded to that the influence on the AAM_y^{NCEP} data is far
from being statistically robust and has a speculative character which needs fur-
ther investigations. The strong coherence is outside the Cone Of Influence (COI).

Some spots show significant coherences with periods of three to four years.
At the bottom of the diagram with periods of about one and a half year the
dominating annual cycle is denoted. It is much more distinct in Fig. 5.26. In
contrast to the x-component the y-components has a continuous annual signal
throughout the whole time span in NCEP and ECHAM which induces very strong

---

[2]Chavez' fundamental Science article has been cited about 250 times since being published

permanently significant coherences. As for the x-component some significant
"drip-offs" are obvious. At significantly coherent regions, NCEP and ECHAM
are right in phase and noisy for the rest of the map.
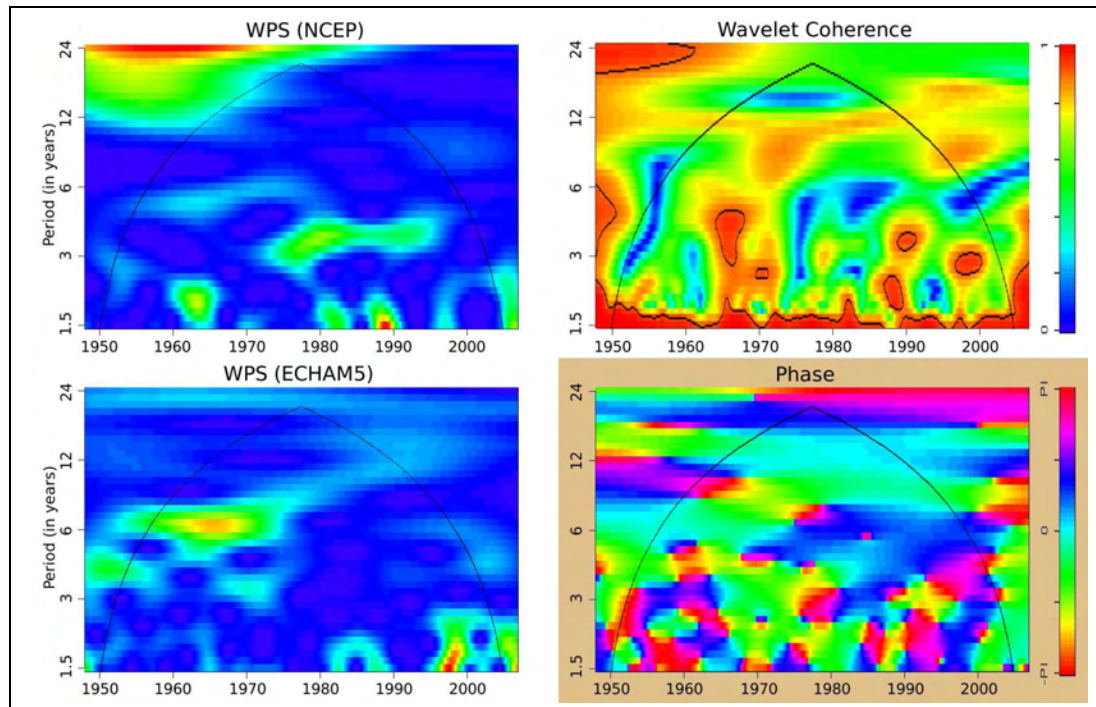
Figure 5.25: Wavelet power spectrum (WPS) of AAM_y for NCEP (top left) and
for ECHAM5 ensemble mean (bottom left), joint wavelet coherence (top right)
and phase diagram (bottom right). Five percent significance level is indicated
by a black contour line. Energies are standardised by maximum energy.

5.4.2   Seasonal Cycle of Equatorial AAM

As a consequence of the results in the previous section this section will decompose
the seasonal cycle within AAM_x^{ECHAM} in detail. As a reference an additional
data set is derived from geodetic observations. Very reliable results of polar mo-
tion observation are at hand for almost the last three decades. Both, atmosphere
and ocean contribute to polar motion by the same order of magnitude (Thomas
et al., 2005). In this analysis the oceanic contribution will be subtracted from
geodetic polar motion observation by using assimilated ocean data. Hydrologic
effects are still included in the C04 polar motion data set. The Earth is not
a perfect sphere therefore its polar moment and equatorial moment of inertia
differ which leads to a free nutation movement — the Chandler wobble. This
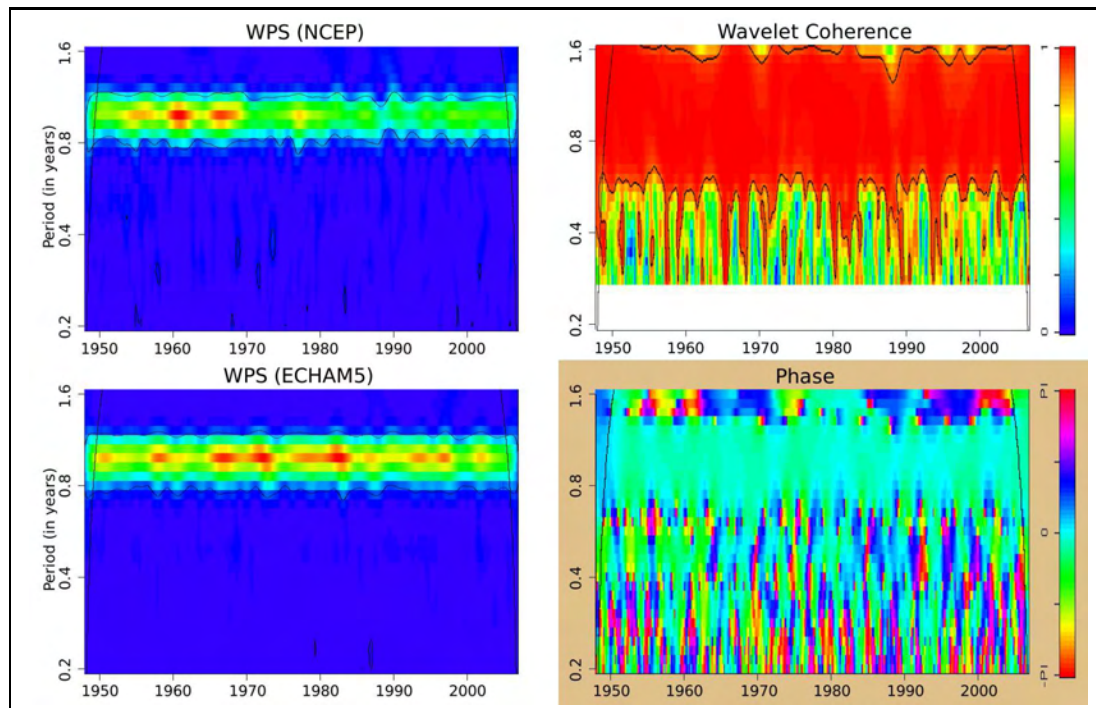
Figure 5.26: Wavelet power spectrum (WPS) of AAM_y for NCEP (top left) and
for ECHAM5 ensemble mean (bottom left), joint wavelet coherence (top right)
and phase diagram (bottom right). Five percent significance level is indicated
by a black contour line. Energies are standardised by maximum energy.

movement has a rather constant period of about 433 days.

The ECCO data set (Gross et al., 2005) provides global oceanic angular mo-
mentum (OAM) values for more than 50 years. This research concentrates on the
1993 to 2005 period where daily values are published on the IERS web site. The
ECCO data were created by applying atmospheric forcing (NCEP) to a global
ocean model (MITgcm). Atmospheric surface pressure was not applied to the
ocean model, that's why the non-IB assumption is valid here. Altimetric mea-
surements of sea surface height (SSH), measured vertical temperature profiles
and velocities (XBT data) were assimilated.

In Fig. 5.27 three time series are displayed. The combined matter and mo-
tion term effect of AAM_x on polar motion for the ECHAM simulation (median
red line) and for the NCEP reanalysis (dashed black line) is compared to the
geodetic observations (orange line). The ocean effect (matter+motion) has been
removed from the geodetic C04 time series by considering the oceanic angu-
lar momentum (OAM) of the ECCO data set. A high pass filter with a 13
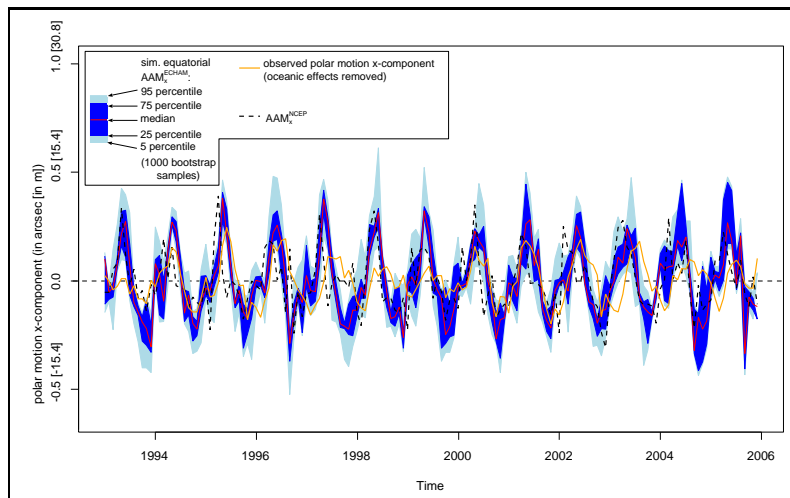
Figure 5.27: High pass filtered polar motion x-component (cut-off frequency: 13 month) for AAM_X^{ECHAM} (blue shadings and median red line), for NCEP (dashed black line) and observed C04-ECCO (orange line).

month cut-off frequency is applied to the time series to eliminate the Chandler wobble in the observations. The annual cycle is quite well explained by the ECHAM model. The estimated correlation coefficient $\hat{\rho}_{ECHAM,C04}^{\chi_1} = 0.435$ is significant on the five ($\hat{\rho}_{\alpha=0.05}^{critical} = 0.23$) and one percent level ($\hat{\rho}_{\alpha=0.01}^{critical} = 0.30$). Once again auto-correlation is respected and the corresponding null hypothesis that the correlation coefficient is not different from zero is tested by a two-sided Student's t-test. The correlation with the reanalysis is higher and estimated by $\hat{\rho}_{ECHAM,NCEP}^{\chi_1} = 0.532$.

The results of the ECHAM simulation are very encouraging keeping in mind that the equatorial components in the AAM are much smaller compared to the axial one (more than two orders of magnitude). This means the equatorial components are much more vulnerable to disturbances. In the diagram this is reflected by a quite big spread in the bootstrap samples. Relative to the amplitude of the seasonal cycle the uncertainty is much larger than in case of the axial component (see Fig. 5.12). In general the annual cycle of the ECHAM AAM_x precedes the one of the C04-ECCO data. The amplitude is overestimated by both ECHAM and NCEP. Here, the C04-ECCO polar motion still contains hydrologic effects and therefore is not a perfect reference.

For reasons of comparability the Chandler wobble (CW) is removed from the observed C04-ECCO polar motion by simply suppressing frequencies with periods greater than 13 month. Obviously the temporal resolution of one month
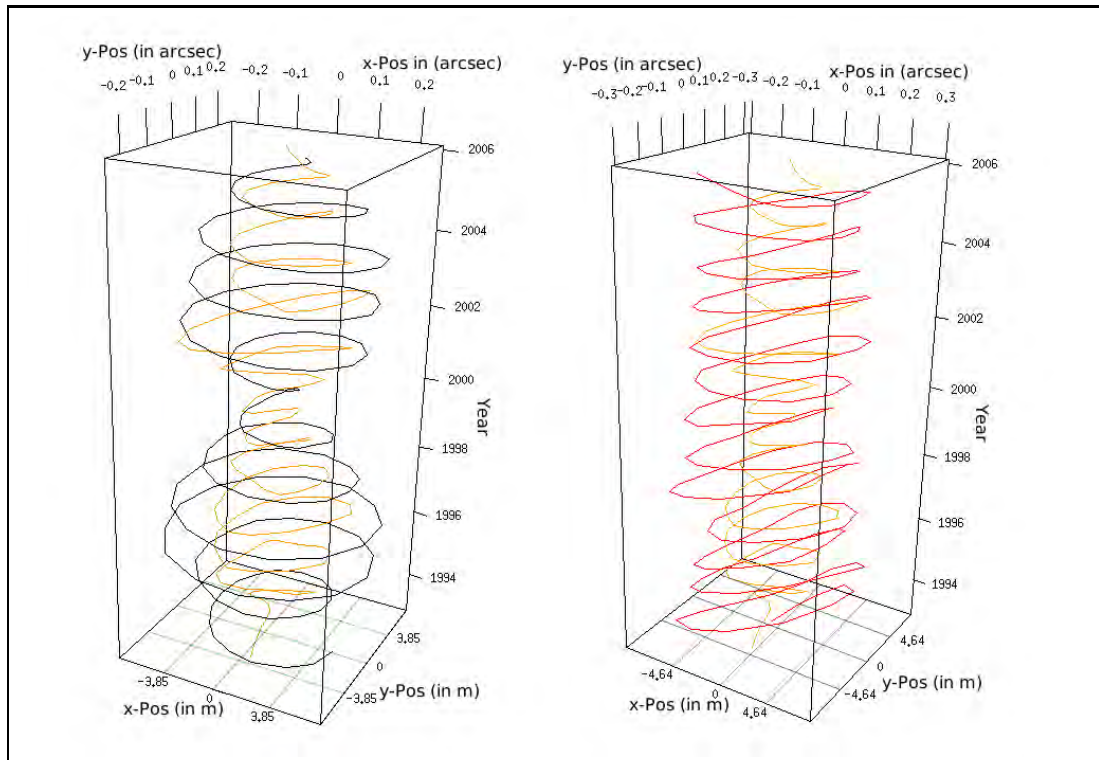
Figure 5.28: Left: observed C04 polar motion (black line) and C04 polar motion
minus ocean effects high pass filtered with a 13 month cut-off frequency (orange
line).
Right: C04 polar motion minus ocean effects high pass filtered with a 13 month
cut-off frequency (orange line) and effects on polar motion derived from ECHAM5
median (red line). Please note that the scale is different.

is critical to clearly distinguish between CW and annual cycle, therefore the re-
maining orange line (Fig. 5.28) still contains a low frequency modulation which
is due to superposition of annual and Chandler oscillation. A LOESS smoothing
is applied to reduce noise which was present as the OAM effects were removed.
The LOESS smoother considers seven data points and polynomials to the order
of two.

On the right hand side the ECHAM5 excitation of polar motion is added. It
underwent the same smoothing procedure than the observed C04-ECCO data.
The annual cycle is overestimated in both components and no low frequency
modulation can be seen. Whereas the observation describe a close to circular
motion the atmospheric excitation tends to a more elliptic shape with higher
amplitudes in the y-component. The simulated oscillation is also slightly out of
phase. Nevertheless these atmospheric excitations of polar motion point at the

fact that the remaining high pass filtered ocean corrected observed polar motion
can be explained to a large extent by atmospheric excitations. Major sources of
disagreements are:

- temporal resolution of one month not allowing for clear spectral distinction
  between CW and annual cycle

- the neglect of hydrologic effects

- simplistic assumptions of Earth's properties concerning response to applied
  external excitations

- errors in the atmospheric GCM

Chapter 6

Coupled Simulation of Earth Rotation Parameters

An experiment with the coupled ECOCTH model (see section 4.1) was conducted. Three ensemble member runs only differing in their initial conditions started in 1860. The simulation period ended in the year 2000, from then on the A1B scenario was applied to the model runs ending in the year 2060. In this chapter an AAM analysis of the ECHO-G and ECOCTH A1B scenario runs follows a brief analysis of the ECOCTH simulation period.

The global 2m temperature anomaly of the ECOCTH simulations shows very small departures from the observed time series (Fig. 6.1). The interannual variability is overestimated strongly and results from an overestimation of ENSO by about 300 percent. The nature of the ensemble mean implies that it fluctuates less intensely in time.

From the ECOCTH simulations, AAM have been calculated by the formulas already introduced. The power spectrum of the axial AAM component of NCEP, ECHAM5 standalone and ECOCTH is plotted in Fig. 6.2. The dominant annual and semiannual signals are comprehended by the ECOCTH containing slightly less energy than NCEP and ECHAM at these frequencies. An analysis in the time-frequency domain by wavelet decomposition is not advisable as the ECOCTH is a free model and thus generates SST oscillations internally and independent of time, whereas the ECHAM5 model is forced by time dependent SSTs.

In the power spectrum, strong ECOCTH overestimations are found at the ENSO region. The unrealistically strong ENSO amplitude leaves a fingerprint in the temperature time series and the axial AAM spectrum as well. It seems, as if
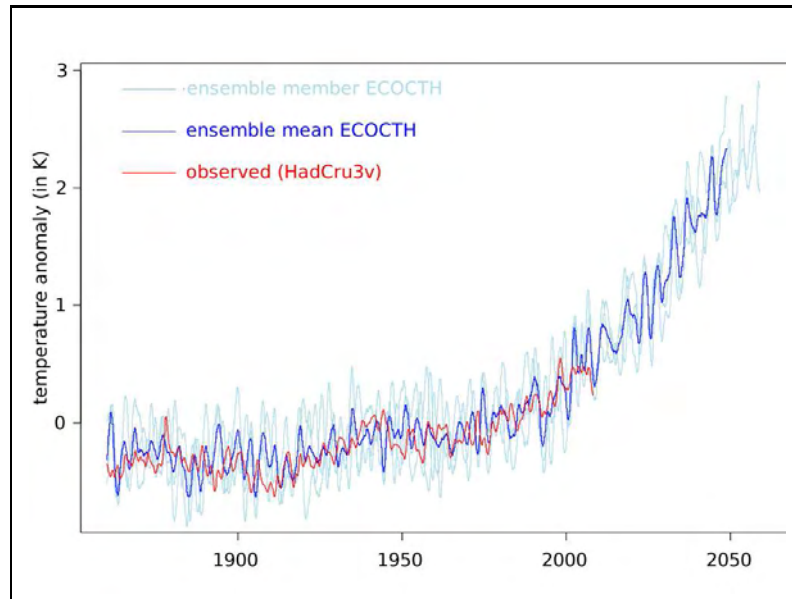
Figure 6.1: Global combined land-sea 2m temperature anomaly time series for
ECOCTH simulations - three members (light blue), ensemble mean (blue) and
observed HadCruTem3v values (red).

the deviation is limited to the frequency band mentioned and does not disturb
other parts. In a high frequency region with frequencies of four to six times a
year the free coupled model (ECOCTH - red) comprises higher energy densities
than the standalone runs (ECHAM - blue). Here, the free coupled model is closer
to the atmospheric reanalysis, demonstrating that the dynamic coupling might
enhance the atmospheric variability on these time scales effectively. Except for
the ENSO estimation no significant systematic error can be revealed at this
point within the free coupled simulations. As the model succeeds in following
major AAM and global 2m temperature structures in the past, a scenario run is
conducted to examine possible future long term trends under a climate change
scenario.

6.1 Axial AAM Long-term Trends in 21st Century Scenario Runs

Future climate conditions explicitly depend on future boundary conditions. Fu-
ture boundary conditions are uncertain and not subject of the meteorologists or
climatologists theirselves. In climate change studies the research processes as
follows: Different sets of possible future boundary conditions are derived from
economic, technical and demographic models. These scenarios are independently
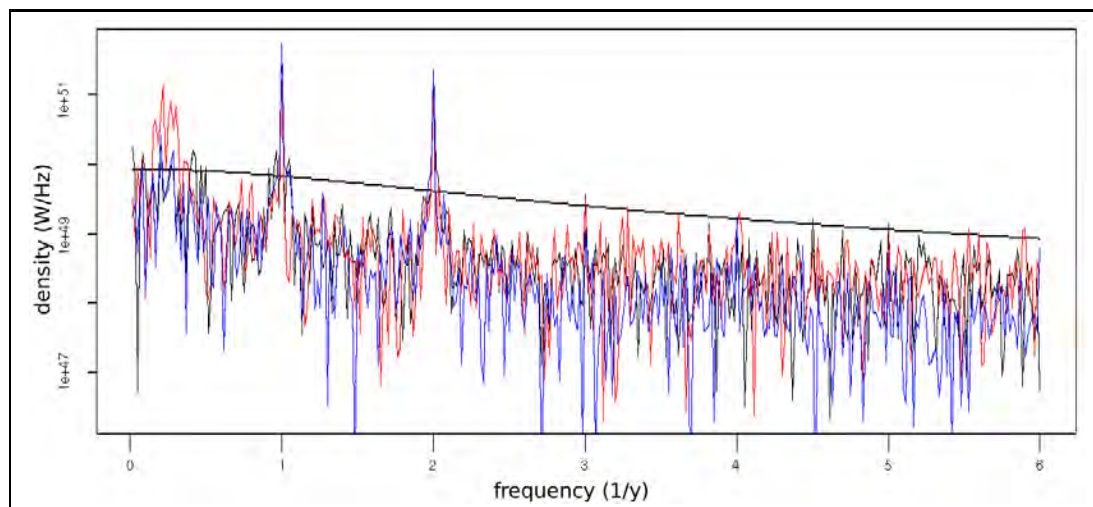
Figure 6.2:   Global axial AAM (mass/non-IB+motion) power spectrum for
ECOCTH ensemble mean (red), ECHAM5 standalone ensemble mean (blue),
NCEP (black) and 95 percent confidence level (black) for 1948 to 2006 period.

applied to climate models. The results of the climate models should not be in-
terpreted as particular climate forecast. They are rather the outcome of a model
given the specific scenario applied and climate model version used. For this work
only one scenario is used. All common scenarios do not differ much in the begin-
ning of the 21st century, therefore the results of different scenarios show a much
bigger spread in the second half of the 21st century (IPCC, 2007). To make
statements over future climate conditions in the second half of the century all
common scenarios should be respected. The AAM study in the following section
ends in the year 2060.

A lot of studies project an increasing global axial AAM for the 21st century.
Lorenz and DeWeaver (2007) investigated the zonal wind response to global
warming. They analysed the IPCC models under climate change scenarios and
obtained an amplification of zonal wind in global terms. The dynamic reason of
the increase cannot be retraced easily. Strongly increased temperatures in the
upper tropics enhance the meridional temperature gradient. In the inner tropics
the tropopause level is rising. Therefore, the tropopause slope towards the poles
is getting intensified. Stratospheric cooling and tropospheric warming increase
the meridional temperature gradient and due to the thermal wind balance, west-
erlies become stronger. The increase in kinetic energy at the tropopause level is
consistent with the rise in tropopause height because synoptic waves are trapped
in the troposphere. This does not contradict with the popular impression that
the Arctic is especially warming, as the Arctic warming is primarily confined to

the near surface levels.

In his study de Viron et al. (2002) analysed a CMIP2 (Meehl et al., 2000) model ensemble with an increase in CO_2 concentrations of one percent per year which is higher compared to the A1B-scenario ($\sim$0.6 percent per year). In the CMIP2 study, the HadCM2 model showed a 0.53 ms/century trend in ΔLOD in the AAM motion-term while other models only reached 0.1 ms/century. The discrepancy between different models in the ΔLOD trend indicates that model uncertainty is an important issue.
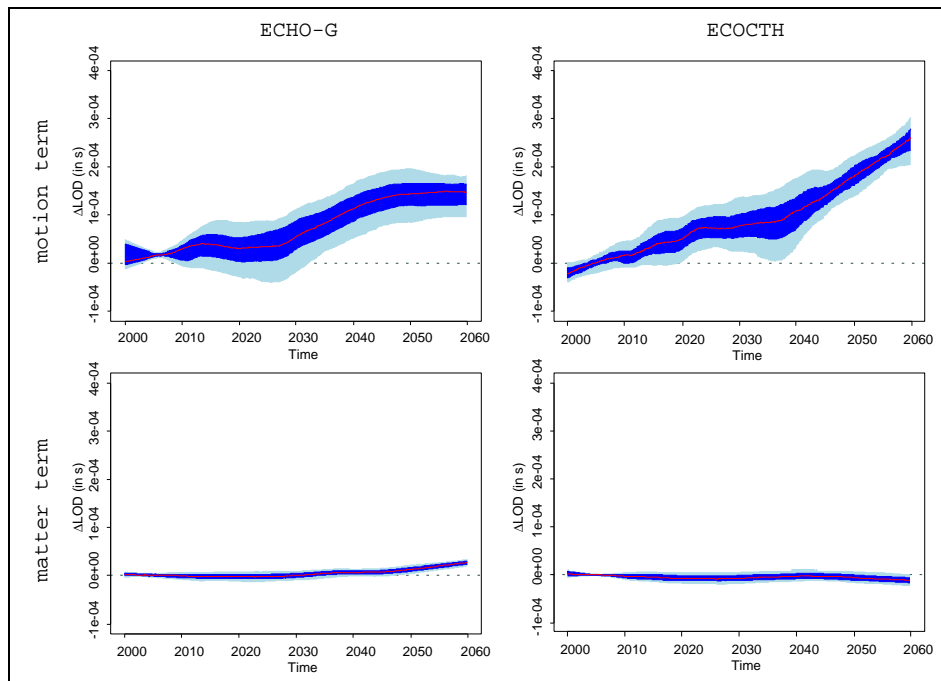
Figure 6.3: AAM motion (top) and matter (bottom) term effects on ΔLOD of ECHO-G (left) and ECOCTH (right), 25th to 75th percentile range (blue band), 5th to 95th percentile range (light blue band) and median (red line).

The uncertainties of the ECOCTH and ECHO-G (introduced in chapter 4) A1B scenario runs in Fig. 6.3 are again deduced from bootstrapping. As the number of ensembles is critically small the subset sample size was set to five years to ensure sufficient possible combinations. After drawing 1,000 bootstrap samples, a LOESS smoother with a 20 year bandwidth was applied to every sample. The reference is the 2000 to 2009 ensemble mean. Both models induce a significant positive trend in the axial AAM motion term for the 2000 to 2060 period. The ECHO-G model possesses a higher uncertainty in general embodied

by a broader ensemble spread. Interestingly, the strongest trend is simulated
for the period between 2025 and 2045, thereinafter the slope flattens. In con-
trast, the ECOCTH simulates the strongest increase in the last two decades and
reaches an AAM motion term induced lengthening of LOD nearly twice as high
as ECHO-G for the year 2060. A linear trend estimation does not seem very
suitable because the ECHO-G somehow shows a stepwise increase, whereas the
ECOCTH time series rather follows an exponential law.

The matter term trends have much smaller uncertainties and do not differ
significantly from zero until 2045 in case of ECHO-G and not at all for ECOCTH
at the five percent significance level. De Viron deduced a compensating effect
of the matter term. For the year 2100 he estimated an expectation value of the
CMIP2 model ensemble by approximately -0.075ms. His estimation is not backed
by the two models in this analysis. ECOCTH shows a slightly negative but not
significant trend, while ECHO-G even deduces a positive trend. A positive trend
in the matter term would mean that under the assumption of mass conservation,
more mass will be concentrated at lower latitudes equivalent to higher surface
pressure at low latitudes.

In the year 2060, the increased axial AAM (matter/non-IB+motion) within
the model would cause a lengthening of a solar day by about $0.17 \pm 0.03 \; ms$ for
ECHO-G and $0.26 \pm 0.03 \; ms$ for ECOCTH. The estimated errors only reflect
the model uncertainty. Of course, other sources of errors exist, for instance
the scenario itself is "uncertain". However it should be kept in mind that the
model ΔLOD result comprehends solely the effect of the atmosphere which is
superimposed by other effects on the interdecadal/centurial time scales. To give
an impression of the size of the atmospheric effect, other effects are estimated
for the year 2060 and summarised in table (6.1) referring to de Viron.

effect	60 year trend in ΔLOD estimate
Tidal friction	1.2
Contin. water reservation	-0.36
Post glacial rebound	-0.3
Sea level (thermal exp.)	0.03
Glacier melting	0.024

Table 6.1: Estimates for the 2000 to 2060 trend in ΔLOD (in $\frac{ms}{60y}$) (de Viron
et al., 2002).

The Earth constantly looses angular momentum to the moon due to tidal
friction. This effect is very strong on the centurial time scale. Unfortunately,
no error estimates are available for the effects, but tidal friction effect estimates
have a relatively high accuracy. The accuracy of the estimates decreases from
the top to the bottom of the table. Continental water reservation leads to an
decreased moment of inertia resulting in a faster Earth rotation. The third effect
accounts for the rise of continents which were covered by glaciers in the past.
Siberia and Fennoscandia are still rising.

In a changing climate the distribution and concentration of water and ice
masses will change when temperatures increase. The last two effects can directly
be linked to climate change.

The effect of an increased AAM on LOD in a future climate has the same
order of magnitude as that of post glacial rebound of continents or the reservation
of continental water. The differences and discrepancies between certain models in
predicting future LOD conditions point at high uncertainties. Interestingly, from
the year 2040 on the models start diverging. This behaviour is rather similar
to the projections of the global 2m temperature, where the models are in high
accordance until approximately 2040 and start diverging in the following (IPCC,
2007).

Chapter 7

Conclusions and Outlook

This work provides new insight into AAM fluctuations. A model-based approach has been performed to examine the ability of atmospheric GCMs to generate typical AAM variations. The atmospheric standalone model is driven by greenhouse gas, solar, SST and SIC forcing as well as by a prescribed aerosol climatology. Five twentieth century simulations have been conducted with the ECHAM5 model differing only in the initial states. A detailed structure analysis compares AAM time series from these simulations to those of geodetic ΔLOD and polar motion observations and to reanalysis data.

For the axial AAM component, different frequency bands are separated from the simulated time series by a Fourier decomposition. The power spectrum of the axial AAM time series shows several significant peaks concentrating at periods of three to five years. For the 1962 to 2006 period, the correlation coefficient between the median of the ECHAM5 AAM ensemble and the observed ΔLOD time series is estimated by $\rho_{ECHAM,obsLOD} = 0.7$ in a frequency band with periods from 2.5 to 5.5 years. The simulated AAM is able to explain a similar proportion of the ΔLOD variance as the reanalysis based AAM. The correlation estimation has been accomplished for every bootstrap sample and indicates a wide range with an inter-quantile range of $IQR(\rho_{ECHAM,obsLOD}) > 0.1$.

The excitation of AAM oscillations in the spectral domain at 2.5 to 5.5 year periods can be attributed to an effective SST forcing in the ENSO region. Significant correlations at the one percent level between the model's 2m temperature and the model's global axial AAM cover the whole tropical Central Pacific.

The ECHAM5 simulations fail in producing quasi-biennial zonal wind oscillations in the tropical stratosphere. Apparently, the setting of 31 vertical layers

is not sufficient to originate a QBO within the model. The stratospheric zonal winds oscillate semiannually at the one percent significance level instead of biannually such as it is observed.

On a seasonal scale, significant signals of the axial AAM ensemble median are revealed for frequencies $f = \frac{N}{1y}$ with $N = 1, 2, 3, 4, 5, \ldots$. The statistical robustness of the $\frac{N}{1y}$ oscillations exceeds those from reanalysis data by far. It is demonstrated that the seasonal cycle of the simulated global axial AAM has a non-harmonic structure during the main decrease in May and June. Signals at frequencies $N \geq 3$ contribute to the annual and semiannual signals.

The ECHAM5 simulations are able to explain the observed annual ΔLOD variations by more than 96.4 percent. During the evolution of the ECHAM model chain the constitution of the annual AAM cycle has improved dramatically in recent years. E.g. the ECHAM3 model produced an annual AAM amplitude which only explained about 50 percent of the annual ΔLOD variations.

In case of the semiannual ΔLOD oscillations, the results are worse in quality compared to the annual ones. The model uncertainty is remarkably larger for the semiannual AAM oscillations. A phase shift of about 9 days between the ECHAM5 semiannual AAM cycle and the observed ΔLOD cycle indicates a rather good agreement but the size of the amplitude is underestimated strongly by the model and only reaches about 66 percent of the observed one. The semiannual AAM cycle based on NCEP illustrates deviations in the same direction, although it is closer to the observations than the ECHAM5 based AAM. A significant difference between the semiannual amplitude in zonal wind speed of ECHAM5 and NCEP is present for the Southern Hemisphere jet stream denoting a possible source of the ECHAM5 underestimation in the AAM semiannual amplitude.

Noticeably high correlations are found between the annual mean solar irradiance and the annual amplitudes of the axial AAM of NCEP and the observed ΔLOD. The annual amplitudes deduced from NCEP are significant at the ten percent significance level, a physical relation could be existent. For the semiannual case correlations are strongly negative and significantly different from zero at the ten percent level for NCEP and the observed ΔLOD. The ECHAM5 AAM does not indicate a relation between the annual/semiannual amplitudes and the solar irradiance at all. For the semiannual case an one-way ANOVA of the ECHAM results indicates that only 11.2 percent of the semiannual amplitude

variability can be assigned to external boundary conditions.

To investigate external excitations of axial AAM variations within the ECHAM5 standalone runs, an ANOVA is applied to the time series of the axial AAM density component for every grid point. In the tropical Atlantic and Pacific the proportion of explained variance by external forcing factors reaches maximum values exceeding 50 percent. In the inner tropics internal variability is less effective on annual and interannual time scales compared to high latitude regions. In general, the AAM density variations of ocean grid points is influenced by external factors to a bigger extent. In high latitude regions only a few grid points show a significant excitation due to external forcing.

In another ANOVA study the decadal trend variability is analysed. Significant trends of local AAM density for the last three decades are mainly positive and found at Southern Hemisphere ocean locations. But only very few grid points show statistically robust trends for the 1974 to 2003 period. Nevertheless, the global axial AAM trend during this epoch is significant at the one percent significance level for the ECHAM5 standalone simulations. Possible external excitations are revealed by the ANOVA technique. Interestingly the global patterns are quite similar to the proportion of explained variance of monthly mean AAM density variations by external factors. The decadal trends at the tropical Atlantic are again remarkably strongly driven by boundary conditions, whereas Europe and the Northeast Atlantic do not show any significant decadal trend variations which can be explained by the combined SST/SIC, solar, greenhouse gas and aerosol forcing.

The equatorial AAM components of the standalone runs are compared to the ones deduced from the NCEP reanalysis. Structures in the time-frequency domain of the NCEP equatorial AAMs are rather well captured by the simulation. Geodetic observations with the oceanic signals removed indicate smaller amplitudes of the annual cycle and a phase shift of one to two months. The x-component is highly correlated with the sun spot cycle. Significant coherences between NCEP and ECHAM5 are exposed for periods of 11 years for a certain time span.

Two coupled ocean-atmosphere GCMs (ECHO-G and ECOCTH) are analysed concerning the global axial AAM long term trends under an A1B-scenario until the year 2060. The motion term has a significantly positive trend within both models. Until 2040 the axial AAM increase is in a good agreement between

the two models. Afterwards the ECOCTH intensifies the AAM motion term increase while the ECHO-G denotes a stabilisation at a certain level resulting in a ΔLOD increase of about $0.17 \pm 0.03 \ ms$ for ECHO-G and $0.26 \pm 0.03 \ ms$ for ECOCTH in 2060 respectively. The uncertainty of the motion term trend is much higher than the one of the matter term. Trends in the AAM matter term are generally weak. In contrast to the ECOCTH model the ECHO-G deduced AAM matter term trend is significantly positive for the last two decades of the research period.

This work has been able to answer most of the questions which have been posed. But new questions have emerged during the research process. The state of the AAM understanding still has a very rudimentary character, thus, this work can be regarded as fundamental research. Naturally, many new questions arise in such a research field keeping in mind that the extent of interactions in the whole Earth-geophysical fluid system is enormous. It is impossible to give respect to all interactions, therefore, a lot of assumptions and neglects were made, for instance in solving the fundamental Liouville equation, in the atmospheric model itself, and in estimating the Earth's rotation respond to imposed angular momentum changes of its fluid subsystems. Nevertheless, the major causes of variations in Earth rotation are well understood by now and this work has highlighted new aspects of causes of AAM variations.

The approach of clearly differentiating between internally and externally caused AAM fluctuations is advisable as the atmosphere is a partially chaotic system and therefore the globally integrated AAM contains both deterministic signals and chaos. The model uncertainty represents conditional probabilities given the external boundary conditions. A continuation of the ANOVA presented in this work in such a manner that an experimental design would allow to separate the effect of different forcing factors on AAM variations would be very beneficial and help to further perceive causes of AAM variations. Other interesting questions arose and have been formulated. Some hints were found that the solar irradiance has an impact on the size of the amplitude of the annual or semiannual cycle within the AAM. Another point which needs further devotions is the changing AAM on long term time scales in a changing climate. The work has also shown that firstly, two independent A1B scenario runs diverge from each other from 2040 on concerning their axial AAM component and secondly, the model uncertainty of both models is fairly high. All in all uncertainty is a big issue in long term AAM changes and should be analysed by further studies.

Appendix A

List of Symbols

A, B	Earth equatorial moment of inertia
α	probability of type I error, significance level
α_1	first coefficient of the auto-correlation function
β	probability of type II error
β^{cl}	confidence level
γ	auto-covariance function
C, C_m	Earth polar moment of inertia
c_1	Fourier coefficient number one
c_p, c_v	specific heat at constant pressure, volume
$\vec{\chi}$	dimensionless excitation function
CH_4	methane
CO_2	carbon dioxide
Δ	non-centrality parameter
$div(\vec{v})$	divergence
DOF	degrees of freedom
$E(\mathbf{X})$	expectation value of random variable $\mathbf{X}$
ϵ_i	error i
η	hybrid level
F	F-ratio
$F(x)$	function F of x
$\vec{F_R}$	friction force
$\vec{g}$	Earth's acceleration due to gravity
$\vec{h}$	angular momentum
H_0	null hypothesis
H_A	alternative hypothesis
$h_k(x)$	distance weighting function
h_k	specific enthalpies
I	interval
$\mathbf{I}$	tensor of inertia
$inf\{x\}$	infimum of x
J	cost function
κ	$cos(\varphi)$

$\vec{L}$	torque
λ	longitude
m	mass
m_k	k-th moment
μ_k	k-th central moment
μ	expectation value
MSE	mean squared error
N, n	number of realisations
$\mathcal{N}(\mu, \sigma)$	normal distribution with mean μ and standard deviation σ
N_2O	nitrous oxide
NO_2	nitrogen dioxide
ν	frequency
O_3	ozone
$\vec{\omega}$	Earth's angular velocity
$\vec{\Omega}$	uniform Earth's angular velocity
$\mathrm{P}(E)$	probability of event E
p_{surf}	surface pressure
Φ	gravitational potential
$\Phi(\nu(n))$	spectral density
φ	latitude
P_A	explained proportion of total variance
P_n^m	Associated Legendre functions of the first kind
$\Psi_0(\eta)$	wavelet function
q_i	mixing ratio
Q_R, Q_L, Q_F	heating (due to radiation, phase change, friction)
R	gas constant
ρ	density
ρ_{XY}	correlation coefficient between random variables $\mathbf{X}$ and $\mathbf{Y}$
ρ_{xx}	auto-correlation function of random variable $\mathbf{X}$
$\mathcal{S}$	sample space
σ	standard deviation
SO_2	sulfur dioxide
T	temperature
$\Theta_{i,k}$	parameter of distribution
u	zonal wind
V	volume
$\vec{v}$	wind vector
w_k	regression weight k
$W(h)$	distance weight
x_2	amplitude
x_3	phase shift
ξ	vorticity

Table A.1: List of Symbols

Appendix B

List of Acronyms

AAM	Atmospheric angular momentum
ANOVA	Analysis of variance
AR	Assessment report
COI	Cone of influence
CRU	Climate research unit
DORIS	Doppler orbit determination and radiopositioning integrated on satellite
ECCO	Estimating the circulation and climate of the ocean
ECOCTH	ECHAM ocean circulation tide hydrology model
ENSO	El Niño southern oscillation
ERP	Earth rotation parameter
GCM	General circulation model
GPS	Global Positioning System
IERS	International Earth Rotation and Reference Systems Service
IPCC	Intergovernmental Panel on Climate Change
LLR	Lunar Laser Ranging
LOD	Length of day
LOESS	Locally weighted regression
MJO	Madden Julian oscillation
MPI-M	Max Planck Institute for Meteorology
QBO	Quasi-biennial oscillation
SIC	Sea ice concentration
SLR	Satellite Laser Ranging
SOI	Southern oscillation index
SSH	Sea surface height
SST	Sea surface temperature
TAO	Tropical atmosphere ocean array
VLBI	Very long baseline radio interferometry

Table B.1: List of Acronyms

Appendix C

Tidal Modelling

N	l	l'	F	D	W	PERIOD DAYS	$UT1 - UT1_R$ A_i in $10^{-4}s$	$LOD - LOD_R$ A_i' in $10^{-5}s$	$\omega - \omega_R$ A_i'' in $10^{-14}\frac{rad}{s}$
1	1	0	2	2	2	5.64	-0.024	0.26	-0.22
2	2	0	2	0	1	6.85	-0.040	0.37	-0.31
3	2	0	2	0	2	6.86	-0.099	0.90	-0.76
4	0	0	2	2	1	7.09	-0.051	0.45	-0.38
5	0	0	2	2	2	7.10	-0.123	1.09	-0.92
6	1	0	2	0	0	9.11	-0.039	0.27	-0.22
7	1	0	2	0	1	9.12	-0.411	2.83	-2.39
8	1	0	2	0	2	9.13	-0.993	6.83	-5.76
9	3	0	0	0	0	9.18	-0.018	0.12	-0.10
10	-1	0	2	2	1	9.54	-0.082	0.54	-0.45
11	-1	0	2	2	2	9.56	-0.197	1.30	-1.10
12	1	0	0	2	0	9.61	-0.076	0.50	-0.42
13	2	0	2	-2	2	12.81	0.022	-0.11	0.09
14	0	1	2	0	2	13.17	0.025	-0.12	0.10
15	0	0	2	0	0	13.61	-0.299	1.38	-1.17
16	0	0	2	0	1	13.63	-3.208	14.79	-12.48
17	0	0	2	0	2	13.66	-7.757	35.68	-30.11
18	2	0	0	0	-1	13.75	0.022	-0.10	0.08
19	2	0	0	0	0	13.78	-0.338	1.54	-1.30
20	2	0	0	0	1	13.81	0.018	-0.08	0.07
21	0	-1	2	0	2	14.19	-0.024	0.11	-0.09
22	0	0	0	2	-1	14.73	0.047	-0.20	0.17
23	0	0	0	2	0	14.77	-0.734	3.12	-2.64
24	0	0	0	2	1	14.80	-0.053	0.22	-0.19
25	0	-1	0	2	0	15.39	-0.051	0.21	-0.17
26	1	0	2	-2	1	23.86	0.050	-0.13	0.11
27	1	0	2	-2	2	23.94	0.101	-0.26	0.22
28	1	1	0	0	0	25.62	0.039	-0.10	0.08
29	-1	0	2	0	0	26.88	0.047	-0.11	0.09
30	-1	0	2	0	1	26.98	0.177	-0.41	0.35
31	-1	0	2	0	2	27.09	0.435	-1.01	0.85
32	1	0	0	0	-1	27.44	0.534	-1.22	1.03
33	1	0	0	0	0	27.56	-8.261	18.84	-15.90
34	1	0	0	0	1	27.67	0.544	-1.24	1.04
35	0	0	0	1	0	29.53	0.047	-0.10	0.08
36	1	-1	0	0	0	29.80	-0.055	0.12	-0.10
37	-1	0	0	2	-1	31.66	0.118	-0.23	0.20
38	-1	0	0	2	0	31.81	-1.824	3.60	-3.04

39	-1	0	0	2	1	31.96	0.132	-0.26	0.22
40	1	0	-2	2	-1	32.61	0.018	-0.03	0.03
41	-1	-1	0	2	0	34.85	-0.086	0.15	-0.13
42	0	2	2	-2	2	91.31	-0.057	0.04	-0.03
43	0	1	2	-2	1	119.61	0.033	-0.02	0.01
44	0	1	2	-2	2	121.75	-1.885	0.97	-0.82
45	0	0	2	-2	0	173.31	0.251	-0.09	0.08
46	0	0	2	-2	1	177.84	1.170	-0.41	0.35
47	0	0	2	-2	2	182.62	-48.247	16.60	-14.01
48	0	2	0	0	0	182.63	-0.194	0.07	-0.06
49	2	0	0	-2	-1	199.84	0.049	-0.02	0.01
50	2	0	0	-2	0	205.89	-0.547	0.17	-0.14
51	2	0	0	-2	1	212.32	0.037	-0.01	0.01
52	0	-1	2	-2	1	346.60	-0.045	0.01	-0.01
53	0	1	0	0	-1	346.64	0.092	-0.02	0.01
54	0	-1	2	-2	2	365.22	0.828	-0.14	0.12
55	0	1	0	0	0	365.26	-15.359	2.64	-2.23
56	0	1	0	0	1	386.00	-0.138	0.02	-0.02
57	1	0	0	-1	0	411.78	0.035	-0.01	0.00
58	2	0	-2	0	0	1095.17	-0.137	-0.01	0.01
59	-2	0	2	0	1	1305.47	0.422	-0.02	0.02
60	-1	1	0	1	0	3232.85	0.040	0.00	0.00
61	0	0	0	0	2	-3399.18	7.900	0.15	-0.12
62	0	0	0	0	1	-6790.36	-1617.268	-14.95	12.62

Table C.1: low frequency constituents of tidal model (IERS 2003 conventions (McCarthy and Petit, 2004)); it includes 62 periodic components, with periods ranging from 5.6 days to 18.6 years

l = 134°.96 + 13°.064993(MJD-51544.5) Mean anomaly of the Moon
l' = 357°.53 + 0°.985600(MJD-51544.5) Mean anomaly of the Sun
F = 93°.27 + 13°.229350(MJD-51544.5) L -W with L : mean longitude of the Moon
D = 297°.85 + 12°.190749(MJD-51544.5) Mean elongation of the Moon from the Sun
W = 125°.04 - 0°.052954(MJD-51544.5) Mean longitude of the ascending node of the Moon

The corrected values $UT1_R$, LOD_R and ω_R for $UT1$, LOD and ω are obtained from the following linear combinations:

$$\xi_i \;=\; a_1 l + a_2 l' + a_3 D + a_4 F + a_5 W \tag{C.1}$$

$$UT1 - UT1_R \;=\; \sum A_i sin\xi_i \tag{C.2}$$

$$LOD - LOD_R \;=\; \sum A'_i cos\xi_i \tag{C.3}$$

$$\omega - \omega_R \;=\; \sum A''_i cos\xi_i \tag{C.4}$$

Appendix D

Dimensionless χ-Functions

In chapter 5 the axial AAM was derived. The equatorial components and the close to AAM related dimensionless chi-functions will follow in this chapter. The excitation function were introduced by Munk and MacDonald (1960) to obtain a dimensionless formulation of the Liouville Equation. The definition of the chi-components, which follows, is widely used in Earth system science. From a meteorological point of view AAM-terms express the integrated motions and matters of the atmosphere in a more direct manner and are therefore privileged in this work. After a linearisation approach similar to the one performed in chapter 5 the Liouville Equation can be expressed as non homogeneous forcing terms χ_i:

$$\chi_1 = \frac{\Omega^2 I'_{xz} + \Omega \dot{I}'_{yz} + \Omega h_x + \dot{h}_y - L_y}{\Omega^2 (C - A)} \tag{D.1}$$

$$\chi_2 = \frac{\Omega^2 I'_{yz} - \Omega \dot{I}'_{xz} + \Omega h_y - \dot{h}_x + L_x}{\Omega^2 (C - A)} \tag{D.2}$$

$$\chi_3 = \frac{\Omega^2 \, \Delta I'_{zz} + \Omega \, h_z - \Omega \int_0^{t'} L_z \, dt}{\Omega^2 \, C} \tag{D.3}$$

$\mathbf{I}'$ denotes the tensor of inertia of the atmosphere. C the polar moment of inertia and A the equatorial moment of inertia of the rigid Earth. The Earth's tensor of inertia is treated as perfectly rotationally symmetric:

$$\mathbf{I} = \begin{pmatrix} A & 0 & 0 \\ 0 & A & 0 \\ 0 & 0 & C \end{pmatrix} \tag{D.4}$$

Neglecting external torques, accelerations and vertical terms yields in a carte-

sian (x,y,z) coordinate system (winds $\dot{x}, \dot{y}$):

$$\chi_1 = \frac{-\Omega^2 \int_V \rho\, x\, z\, dV - \int_V 2\Omega\, \rho\, z\, \dot{y}\, dV}{\Omega^2 (C - A)} \tag{D.5}$$

$$\chi_2 = \frac{-\Omega^2 \int_V \rho\, y\, z\, dV + \int_V 2\Omega\, \rho\, z\, \dot{x}\, dV}{\Omega^2 (C - A)} \tag{D.6}$$

$$\chi_3 = \frac{-\Omega^2 \int_V \rho\, (x^2 + y^2)\, dV + \int_V \Omega\, \rho\, (y\, \dot{x} - x\, \dot{y}) dV}{\Omega^2\, C} \tag{D.7}$$

The excitation functions (Eq. D.6 to Eq. D.7) consist of contributions from a redistribution of mass and relative motion of mass.

$$\chi = \chi^{\text{matter}} + \chi^{\text{motion}} \tag{D.8}$$

After a transformation from the cartesian to a spherical $(\lambda, \varphi, |\vec{r}|)$ coordinate system with transformations:

$$x = r\, cos\varphi\, cos\lambda \tag{D.9}$$

$$y = r\, cos\varphi\, sin\lambda \tag{D.10}$$

$$z = r\, sin\varphi \tag{D.11}$$

and winds (u - eastward wind and v - southward wind) the chi-functions after integration transform to :

$$\chi_1 = -\frac{r^4}{(C-A)g} \int_{\varphi=-\frac{\pi}{2}}^{\frac{\pi}{2}} \int_{\lambda=0}^{2\pi} p_s\, sin\varphi\, cos^2\varphi\, cos\lambda\, d\lambda\, d\varphi - \frac{1.43 r^3}{\Omega(C-A)g}$$
$$\int_0^{p=p_s} \int_{\varphi=-\frac{\pi}{2}}^{\frac{\pi}{2}} \int_{\lambda=0}^{2\pi} (u\, sin\varphi\, cos\varphi\, cos\lambda - v\, cos\varphi\, sin\lambda) d\lambda\, d\varphi\, dp$$

$$\chi_2 = -\frac{r^4}{(C-A)g} \int_{\varphi=-\frac{\pi}{2}}^{\frac{\pi}{2}} \int_{\lambda=0}^{2\pi} p_s\, sin\varphi\, cos^2\varphi\, sin\lambda\, d\lambda\, d\varphi - \frac{1.43 r^3}{\Omega(C-A)g}$$
$$\int_0^{p=p_s} \int_{\varphi=-\frac{\pi}{2}}^{\frac{\pi}{2}} \int_{\lambda=0}^{2\pi} (u\, sin\,\varphi\, cos\,\varphi\, sin\lambda + v\, cos\varphi\, cos\lambda)\, d\lambda\, d\varphi\, dp$$

$$\chi_3 = \frac{0.7 r^4}{Cg} \int_{\varphi=-\frac{\pi}{2}}^{\frac{\pi}{2}} \int_{\lambda=0}^{2\pi} p_s\, cos^3\varphi\, d\lambda\, d\varphi$$
$$+ \frac{r^3}{\Omega Cg} \int_0^{p=p_s} \int_{\varphi=-\frac{\pi}{2}}^{\frac{\pi}{2}} \int_{\lambda=0}^{2\pi} u\, cos^2\varphi\, d\lambda\, d\varphi\, dp \tag{D.12}$$

The Equations in D.12 describe the complete atmospheric excitation. The factors (1.43 and 0.7) in the Equations account for the Earth's response to

changes in the excitations occurring in load and rotational deformation. In general the response effect of the Earth is counterbalancing excitation from subsystems to a certain extent.

Appendix E

η Values for ECHAM5

E.1 19 Layer Version

k	a_k	b_k
0	0.	0.
1	2000.	0.
2	4000.	0.
3	6046.109375	0.000338993268087506
4	8267.9296875	0.0033571869134903
5	10609.51171875	0.0130700394511223
6	12851.1015625	0.0340771488845348
7	14698.5	0.0706498026847839
8	15861.12890625	0.125916719436646
9	16116.23828125	0.201195418834686
10	15356.921875	0.295519590377808
11	13621.4609375	0.40540921688079
12	11101.55859375	0.524932205677032
13	8127.14453125	0.646107912063599
14	5125.140625	0.759698390960693
15	2549.96899414062	0.856437623500824
16	783.195068359375	0.9287468791008
17	0.	0.972985208034515
18	0.	0.992281496524811
19	0.	1.

Table E.1: Definition of hybrid vertical coordinate in ECHAM5 for a 19 layer setting

E.2   31 Layer Version

k	a_k	b_k
0	0.	0.
1	2000.	0.
2	4000.	0.
3	6000.	0.
4	8000.	0.
5	9976.13671875	0.000390858156606555
6	11820.5390625	0.00291970069520175
7	13431.3945315	0.00919413194060326
8	14736.35546875	0.0203191563487053
9	15689.20703125	0.0369748584926128
10	16266.609375	0.0594876408576965
11	16465.00390625	0.0878949761390686
12	16297.6210937	0.122003614902496
13	15791.59765625	0.161441504955292
14	14985.26953125	0.205703258514404
15	13925.51953125	0.254188597202301
16	12665.29296875	0.306235373020172
17	11261.23046875	0.36114501953125
18	9771.40625	0.41820228099823
19	8253.2109375	0.476688146591187
20	6761.33984375	0.535886585712433
21	5345.9140625	0.595084249973297
22	4050.7177734375	0.65356457233429
23	2911.5693359375	0.710594415664673
24	1954.80517578125	0.765405237674713
25	1195.88989257812	0.817166984081268
26	638.14892578125	0.864955842494965
27	271.6264648437	0.907715857028961
28	72.0635833740234	0.944213211536407
29	0.	0.972985208034515
30	0.	0.992281496524811
31	0.	1.

Table E.2:   Definition of hybrid vertical coordinate in ECHAM5 for a 31 layer setting

Bibliography

J.K. Angell. Evidence of a relation between El Nino and QBO, and for El Nino in 1991-1992. *Geophysical Research Letters*, 19:285–288, 1992.

M.P. Baldwin and D. O'Sullivan. Stratospheric effects of ENSO-related tropospheric circulation anomalies. *Journal of Climate*, 4:649–667, 1995.

M.P. Baldwin, L.J. Gray, T.J. Dunkerton, K. Hamilton, P.H. Haynes, W.J. Randel, J.R. Holton, M.J. Alexander, I. Hirota, T. Horinouchi, D.B.A. Jones, J.S. Kinnersley, C. Marquardt, K. Sato, and M. Takahashi. The quasi-biennial oscillation. *Reviews of Geophysics*, 39(2):179–229, 2001.

R.T.H. Barnes, R. Hide, A.A. White, and C.A. Wilson. Atmospheric Angular Momentum Fluctuations, Length-Of-Day Changes and Polar Motion. *Proceedings Roy. Soc. London*, 387:31–73, 1983.

S. Brinkop and E. Roeckner. Sensitivity of a general circulation model to parameterizations of cloud-turbulence interactions in the atmospheric boundary layer. *Tellus*, 47A:197–220, 1995.

I.N. Bronstein and K.A. Semendjajew. *Taschenbuch der Mathematik.* Verlag Nauka Moskau, 1991. ISBN 3-8154-2000-8.

P. Brosche, U. Seiler, J. Sündermann, and J. Wünsch. Periodic changes in the Earth's rotation due to oceanic tides. *Astronomy and Astrophysics*, 220:318–320, 1989.

B.F. Chao. Interannual length-of-day variation with realtion to the Southern Oscillation/El Niño. *Geophysical Research Letters*, 11:553–563, 1984.

B.F. Chao. Correlation of interannual length-of-day variation with El Niño / Southern Oscillation. *Journal of Geophysical Research*, 93:7709–7715, 1988.

B.F. Chao. Length-of-day variations caused by El Niño-Southern Oscillation and Quasi-Biennial Oscillation. *Science*, 243:923–925, 1989.

J. Chattopadhyay and R. Bhatla. Possible influence of QBO on teleconnections relating Indian summer monsoon rainfall and sea-surface temperature anomalies across the equatorial pacific. *International Journal of Climatology*, 22(1): 121–127, 2002.

F.P. Chavez, J. Ryan, S.E. Lluch-Cota, and C.M. Niquen. From anchovies to sardines and back: Multidecadal change in the Pacific Ocean. *Science*, 299: 217–221, 2003. doi: 10.1126/science.1075880.

W.S. Cleveland. Wind contributions to the Earth's angular momentum budgets in seasonal variation. *Journal of Geophysical Research*, 105(10):12417–12431, 2000.

W.S. Cleveland. Robust locally weighted regression and smoothing scatterplots. *J. Amer. Statist. Assoc.*, 74:829–836, 1979.

S.A. Clough, F.X. Kneizys, and R.W. Davies. Line shape and the water vapor continuum. *Atmos. Res.*, 23:229–241, 1989.

J.W. Cooley and J.W. Tukey. An algorithm for the machine calculation of complex Fourier series. *Math. Comput.*, 19:297–301, 1965.

O. de Viron, V. Dehant, H. Goosse, and M. Crucifix. Effect of global warming on the length-of-day. *Geophysical Research Letters*, 29(7), 2002. doi: 10.1029/2001GL013672.

R.A. del Rio, D. Gambis, and D.A. Salstein. Interannual signals in length of day and atmospheric angular momentum. *Annales Geophysicae*, 18(3):347–364, 2000.

R.A. del Rio, D. Gambis, D. Salstein, P. Nelson, and A. Dai. Solar activity and earth rotation variability. *Journal of Geodynamics*, 36(4):423–443, 2003.

W. Demtröder. *Experimentalphysik 1: Mechanik und Wärme.* Springer-Verlag, 2000. ISBN 3-540-57097-7.

H.F. Diaz and V. Markgraf. *El Niño and the Southern Oscillation. Multiscale Variability and Global and Regional Impacts.* Cambridge University Press, Cambridge, 2000.

J.O. Dickey, S.J. Marcus, C.M. Johns, R. Hide, and S.R. Thompson. The oceanic contribution to the Earth's seasonal angular momentum budget. *Geophysical Research Letters*, 20(24):2953–2956, 1993.

A.T. Doodson and H.D. Warburg. *Admiralty Manual of Tides*. Her Majesty's Stationery Office, 1941.

B. Efron and R. Tibshirani. *An introduction to the Bootstrap*. London: Chapman & Hall, 1993.

B.S. Everitt and D.J. Hand. *Finite mixture distributions*. Chapman & Hall, 1981.

Y. Fouquart and B. Bonnel. Computations of solar heating of the Earth's atmosphere: A new parameterization. *Beitr. Phys. Atm.*, 53:35–62, 1980.

P. Friederichs and A. Hense. Interannual to Decadal Variability of the Atmospheric Circulation in Coupled and SST-forced GCM Experiments. *CLIVAR Exchanges*, 4(4):7–10, 1999. Not peer reviewed.

C. Fröhlich and J. Lean. The Sun's total irradiance: Cycles, trends in the past two decades and associated climate change uncertainties. *Geophysical Research Letters*, 25:4377–4380, 1998.

P. Gaspar and R.M. Ponte. Relation between sea level and barometric pressure determined from altimeter data and model simulations. *Journal of Geophysical Research*, 102:961–971, 1997.

M.A. Giorgetta, E. Manzini, E. Roeckner, M. Esch, and L. Bengtsson. Climatology and Forcing of the Quasi-Biennial Oscillation in the MAECHAM5 Model. *Journal of Climate*, 19(16):3882–3901, 2006.

R. Glowienka-Hense. Forced and free variability of the semi-annual wave in the ECHAM GCM. *Climate Dynamics*, 15(4), 1999. ISSN 0930-7575. doi: 10.1007/s003820050281.

W. Gray, J. Scheaffer, and J. Knaff. Influence of the stratospheric QBO on ENSO variability. *Journal of the Meteorological Society Japan*, 70(5):975–995, 1992.

R. S. Gross, I. Fukumori, and D. Menemenlis. Atmospheric and oceanic excitation of length-of-day variations during 1980-2000. *Journal of Geophysical Research*, 109, 2004. doi: 10.1029/2003JB002432. URL `http://hdl.handle.net/2014/7059`.

R.S. Gross, S.L. Marcus, T.M. Eubanks, J.O. Dickey, and C.L. Keppenne. Detection of an ENSO signal in seasonal length-of-day variations. *Geophysical Research Letters*, 23(23):3373–3376, 1996.

R.S. Gross, I. Fukumori, and D. Menemenlis. Atmospheric and Oceanic Excitation of Decadal-Scale Earth Orientation Variations. *Journal of Geophysical Research*, 110, 2005. doi: doi:10.1029/2004JB003565.

Y.B. Han, J. Zhao, and Z. Li. Inter-annual variation of the earth rotation and El Nino. *Chinese Science Bulletin*, 47(2):105–107, 2002.

B. Haurwitz. The motion of atmospheric disturbances on the spherical Earth. *J. Marine Res.*, 3:254–267, 1940.

A. Hense. Processing of observational data and its implication for climate analysis. In *Landolt-Börnstein - Group V Geophysics*, page 11pp. Springer Berlin Heidelberg, 2006.

A. Hense. Skript zur Vorlesung Numerische Analyse, April 2008.

A. Hense, T. Burkhardt, and P. Friederichs. Einführung in die Statistik, October 2005.

R. Hide and J.O. Dickey. Earth's variable rotation. *Science*, 253(5020):629–637, 1991.

R. Hide, N.T. Birch, L.V. Morrison, D.J. Shea, and A.A. White. Atmospheric angular momentum fluctuations and changes in the length of the day. *Nature*, 286:114–117, july 1980. doi: 10.1038/286114a0.

R. Hide, J.O. Dickey, S.L. Marcus, R.D. Rosen, and D.A. Salstein. Atmospheric Angular Momentum fluctuations during 1979-1988 simulated by global circulation models. *Journal of Geophysical Research*, 102:16423–16438, 1997.

J. Höpfner. Seasonal variations in length of day and atmospheric angular momentum. *Geophys. J. Int.*, 235:407–437, 1998.

IPCC. *Climate Change 2007: The Physical Science Basis*. IPCC, 2007.

G.M. Jenkins and D.G. Watts. *Spectral Analysis and its Application*. Holden-Day, San Fransisco, 1968.

P.D. Jones, M. New, D.E. Parker, S. Martin, and I.G. Rigor. Surface air temperature and its variations over the last 150 years. *Reviews of Geophysics*, 37: 173–199, 1999.

E. Kalnay, M. Kanamitsu, R. Kistler, W. Collins, D. Deaven, L. Gandin, M. Iredell, S. Saha, G. White, J. Woollen, Y. Zhu, M. Chelliah, W. Ebisuzaki,

W. Higgins, J. Janowiak, K.C. Mo, C. Ropelewski, J. Wang, R. Leetmaa, A. Reynolds, R. Jenne, and D. Joseph. The NCEP/NCAR 40-year reanalysis project. *Bull. Amer. Meteorological Society*, 77:437–471, 1996.

Modellbetreuungsgruppe D. Klimarechenzentrum. The ECHAM3 Atmospheric General Circulation Model. Revision 2. Technical report, Sep 1993.

A. Kolmogoroff. *Grundbegriffe der Wahrscheinlichkeitsrechnung.* Springer-Verlag Berlin, 1933.

T.N. Krishnamurti, H.S. Bedi, V. Hardiker, and L. Watson-Ramaswamy. *An Introduction to Global Spectral Modeling.* Oxford University Press, 1988. ISBN 978-0-387-30254-6.

J.E. Kristjánsson, T. Iversen, Ø. Kirkevåg, A. Seland, and J. Debernard. Response of the climate system to aerosol direct and indirect forcing: Role of cloud feedbacks. *Journal of Geophysical Research*, 110, 2005. doi: 10.1029/2005JD006299.

K. Labitzke. *Die Stratosphäre.* Springer-Verlag, Berlin, 1998. ISBN 3540650008.

K. Lambeck. *The Earth's variable rotation: geophysical causes and consequences.* Cambridge University Press, London, UK, 1980.

S. Legutke and R. Voss. The Hamburg Atmosphere-Ocean Coupled Circulation Model ECHO-G. Technical report, DKRZ, Hamburg, 1999.

E. Lehmann, G.C. Leckebusch, U. Ulbrich, and P. Nevir. Effects of ENSO on sub-seasonal to interannual length-of-day (LOD) variability, oral presentation at EGU Vienna. *EGU abstract*, page 1, 2008.

S.J. Lin and R.B. Rood. Multidimensional flux form semi-Lagrangian transport. *Monthly Weather Reviews*, 124:2046–2068, 1996.

U. Lohmann and E. Roeckner. Design and performance of a new cloud microphysics scheme developed for the ECHAM4 general circulation model. *Clim. Dyn.*, 12:557–572, 1996.

D.J. Lorenz and E.T. DeWeaver. Tropopause height and zonal wind response to global warming in the IPCC scenario integrations. *Journal of Geophysical Research*, 112, 2007. doi: 10.1029/2006JD008087.

E.N. Lorenz. The problem of deducing the climate from the governing equations. *Tellus A*, 15(1):1–11, 1964.

F. Lott and M.J. Miller. A new subgrid-scale orographic drag parameterization: Ist formulation and testing. *Quarterly Journal of the Royal Meteorological Society*, 123:101–127, 1997.

S.J. Marsland, H. Haak, J.H. Jungclaus, M. Latif, and F. Roeske. The Max Planck Institute global ocean/sea ice model with orthogonal curvilinear coordinates. *Ocean Modelling*, 5:91–127, 2003.

D.D. McCarthy and G. Petit. IERS Conventions 2003. Technical report, Bundesamts für Kartographie und Geodäsie, Frankfurt am Main, 2004.

G.A. Meehl, G.J. Boer, C. Covey, M. Latif, and R.J. Stouffer. The Coupled Model Intercomparison Project (CMIP). *Bull. Amer. Meteorol. Soc.*, 81:313318, 2000.

F. Mesinger and A. Arakawa. Numerical methods used in atmospheric models. *Global Atmospheric Research Programme (GARP) Publication Series*, 17: 3771–3791, 1976.

S.-K. Min, S. Legutke, A. Hense, and W.-T. Kwon. Internal variability in a 1000-year control simulation with the coupled climate model ECHO-G - I. Near-surface temperature, precipitation and mean sea level pressure. *Tellus*, 57A:605–621, 2005.

S.-K. Min, S. Legutke, A. Hense, U. Cubasch, W.-T. Kwon, and U. Schlese. East Asian climate change in the 21st century as simulated by the coupled climate model ECHO-G under IPCC SRES scenarios. *Journal of the Meteorological Society Japan*, 84:1–26, 2006.

E.J. Mlawer, S.J. Taubman, P.D. Brown, M.J. Iacono, and S.A. Clough. Radiative transfer for inhomogeneous atmospheres: RRTM, a validated k-correlated model for the longwave. *Journal of Geophysical Research*, 102:16663–16682, 1997.

W.H. Munk and G.J.F. MacDonald. *The Rotation of the Earth: A Geophysical Discussion.* Cambridge Univ. Press, 1960.

W.H. Munk and R.L. Miller. Variations in the Earth's Angular Velocity Resulting from Fluctuations in Atmospheric and oceanic circulation. *Tellus*, 2:93–101, 1950.

I. Naito and N. Kikuchi. A seasonal budget of the Earth's axial angular momentum. *Geophysical Research Letters*, 17(5):631–634, 1990.

BIBLIOGRAPHY

I. Naito and N. Kikuchi. Reply to Rosen and Salstein's comment. *Geophysical Research Letters*, 18(10):1927–1928, 1991.

I. Naito, Y.-H. Zhou, M. Sugi, R. Kawamura, and N. Sato. Three-dimensional atmospheric angular momentum simulated by the Japan Meteorological Agency model for the period of 1955-1994. *Journal of the Meteorological Society Japan*, 78(2):111–122, 2000.

N. Nakicenovic and R. Swart. *Emissions Scenarios*. IPCC Special Report. Cambridge University Press, 2000.

T.E. Nordeng. Extended versions of the convective parameterization scheme at ECMWF and their impact on the mean and transient activity of the model in the tropics. *Technical Memorandum No. 206*, 1994.

H.A. Panofsky and G.W. Brier. *Some Applications of Statistics to Meteorology*. Penn State Univ, PA, 1958.

P. Pâquet, V. Dehant, and C. Bruyninx. Earth rotation observations and their geophysical implications. *Bulletin Astronomique de Belgrade*, 156:89–108, December 1997.

S.G.H. Philander. *El Niño, La Niña, and the Southern Oscillation*. Academic Press, San Diego, 1990.

H.J. Punge and M.A. Giorgetta. Differences between the QBO in the first and in the second half of the ERA-40 reanalysis. *Atmospheric Chemistry and Physics*, 7:599–608, 2007.

N.A. Rayner, D.E. Parker, E.B. Horton, C.K. Folland, L.V Alexander, D.P. Rowell, E.C. Kent, and A. Kaplan. Globally complete analyses of sea surface temperature, sea ice and night marine air temperature, 1871-2000. *Journal of Geophysical Research*, 108, 2003. doi: 10.1029/2002JD002670.

N.A. Rayner, P. Brohan, D.E. Parker, C.F. Folland, J.J. Kennedy, M. Vanicek, T. Ansell, and S.F.B. Tett. Improved analyses of changes and uncertainties in sea surface temperature measured in situ since the mid-nineteenth century: the HadSST2 data set. *Journal of Climate*, 19(3):446–469, 2006.

R.J. Reed, W.J. Campbell, L.A. Rasmussen, and D.G. Rogers. Evidence of downward-propagating annual wind reversal in the equatorial stratosphere. *Journal of Geophysical Research*, 66:813–818, 1961.

E. Röckner, G. Bäuml, L. Bonaventura, R. Brokopf, M. Esch, M. Giorgetta, S. Hagemann, I. Kirchner, L. Kornblueh, E. Manzini, A. Rhodin, U. Schlese, U. Schultzweida, and A. Tompkins. The atmospheric general circulation model ECHAM 5. PART I: Model description. *Rep. 349*, 2003.

E. Roeckner, K. Arpe, L. Bengtsson, M. Christoph, M. Claussen, L. Dmenil, M. Esch, M. Giorgetta, U. Schlese, and U. Schultzweida. The atmospheric general circulation model ECHAM-4. Technical report, MPI for Meteorology, Hamburg, 1996.

R. D. Rosen and D. A. Salstein. Variations in atmospheric angular momentum on global and regional scales and the length of day. *Journal of Geophysical Research*, 88:5451–5470, June 1983.

R.D. Rosen. The axial momentum balance of Earth and its fluid envelope. *Surv. Geophys.*, 14:1–29, 1993.

R.D. Rosen and D.A. Salstein. Contribution of stratospheric winds to annual and semi-annual fluctuations in atmospheric angular momentum and the length of day. *Journal of Geophysical Research*, 90:8033–8041, 1985.

R.D. Rosen and D.A. Salstein. Comment on: "A seasonal budget of the Earth's axial angular momentum" by Naito and Kikucho. *Journal of Geophysical Research*, 18(10):1925–1926, 1991.

R.D. Rosen, D.A. Salstein, T.M. Eubanks, J.O. Dickey, and J.A. Steppe. An El Niño signal in Atmospheric Angular Momentum and Earth Rotation. *Science*, 225:411–414, 1984.

M.L. Salby and P.F. Callaghan. Interaction between the QBO and the Hadley circulation: Evidence of solar influence? *Journal of Climate*, 20(8):1583–1592, 2007.

C.-D. Schoenwiese. *Praktische Statistik für Meteorologen und Geowissenschaftler*. Gebrüder Bornträger, Berlin, Stuttgart, 2006. ISBN 978-3-443-01057-7.

A.J. Simmons and D.M. Burridge. An energy and angular-momentum conserving vertical finite difference scheme and hybrid vertical coordinates. *Monthly Weather Reviews*, 109:758–766, 1981.

A.J. Simons, D.M. Burridge, M. Jarraud, C. Girard, and W. Wergen. The ECMWF medium-range prediction models. Development of the numerical formulations and the impact of increased resolution. *Meteor.Atmos.Phys.*, 40: 28–60, 1989.

144

D. Stammer, C. Wunsch, I. Fukumori, and J. Marshall. State estimation improves prospects for ocean research. *Eos Trans. AGU*, 83(27):289–295, 2002. doi: 10.1029/2002EO000207.

V.P. Starr. An Essay on the General Circulation of the Earth's Atmosphere. *J. Meteorol.*, 5:39–43, 1948.

H.V. Storch and F.W. Zwiers. *Statistical Analysis in Climate Research*. Cambridge Univ. Press, 1999. ISBN 0521450713.

D.M. Straus and J. Shukla. Does ENSO Force the PNA? *J. Climate*, 15(4): 2340?2358, 2002.

J. Stuck. *Die simulierte axiale atmosphärische Drehimpulsbilanz des ECHAM3-T21 GCM*, volume 56. Asgard, January 2002.

D. Tanre, J.-F. Geleyn, and J.M. Slingo. *First results of the introduction of an advanced aerosol-radiation interaction in the ECMWF low resolution global model. In: Aerosols and their Climatic Effects*. H. Gerber and A. Deepak (Eds.), Hampton ,Virgina, 1984.

K.E. Taylor, D. Williamson, and F. Zwiers. The sea surface temperature and sea-ice concentration boundary conditions of AMIP II simulations. *PCMDI report No. 60*, 19(3):20pp, 2000.

M. Thomas. *Ocean induced variations of Earth's rotation - Results from a simultaneous model of global circulation and tides*. PhD thesis, University of Hamburg, 2002.

M. Thomas, H. Dobslaw, J. Stuck, and F. Seitz. The ocean's contribution to polar motion excitation - as many solutions as numerical models? In *Forcing of polar motion in the Chandler frequency band: A contribution to understanding interannual climate variations*. Plag, H.-P. and Chao, B. and Gross,R. and van Dam,T. (eds.), 2005.

M. Tiedtke. A comprehensive mass flux scheme for cumulus parameterization in large-scale models. *Monthly Weather Reviews*, 117:1779–1800, 1989.

C. Torrence and G.P. Compo. A Practical Guide to Wavelet Analysis. *Bull. Amer. Meteorological Society*, 79:61–78, 1998.

S. Uppala, J.K. Gibson, M. Fiorino, A. Hernandez, P. Kallberg, X. Li, K. Onogi, and S. Saarinen. ECMWF's Second Generation Reanalysis - ERA-40, 1999.

H. van Loon and K. Labitzke. The Southern Oscillation, part V, The anomalies in the lower stratosphere of the Northern Hemisphere in winter and a comparison with the quasi biennial oscillation. *Monthly Weather Reviews*, 115:357–369, 1987.

R.G. Veryard and R.A. Ebdon. Fluctuations in tropical stratospheric winds. *The Meteorological magazine*, 90:125–143, 1961.

H. von Storch and F.W. Zwiers. Recurrence Analysis of Climate Sensitivity Experiments. *Journal of Climate*, 1(2):157–171, 1988. doi: 10.1175/1520-0442.

C. Walter. *Simulationen hydrologischer Massenvariationen und deren Einfluss auf die Erdrotation*. PhD thesis, Technische Universität Dresden, 2007.

T. Winkelnkemper, F. Seitz, S.K. Min, and A. Hense. Simulation of historic and future atmospheric angular momentum effects on length-of-day variations with GCMs. Springer Verlag, in Press.

J.O. Wolff, E. Meier-Reimer, and S. Legutke. The Hamburg ocean primitive equation model. Technical report, DKRZ, Hamburg, 1997.

J.-S. Xu. On the relationship between the stratospheric quasi-biennial oscillation and the tropospheric Southern Oscillation. *JotAS*, 49(9):725–734, 1992.

T. Yasunari. A possible link of the QBOs between the stratosphere, troposhere and sea surface temperature in the tropics. *Journal of the Meteorological Society Japan*, 67(3):483–493, 1989.

W. Zdunkowski and A. Bott. *Dynamics of the atmosphere*. Cambridge University Press, London, UK, 2003. ISBN 052100666X.

B. Zheng, D.J. Gu, A.L. Lin, and C.H. Li. Dynamical mechanism of the stratospheric quasibiennial oscillation impact on the South China Sea Summer Monsoon. *Science in China Series D-Earth Sciences*, 9:1424–1432, 2007.

F.W. Zwiers. Interannual variability and predictability in an ensemble of AMIP climate simulations conducted with the CCC GCM2. *Climate Dynamics*, 12:825–847, November 1996. doi: 10.1007/s003820050146.

F.W. Zwiers and H. von Storch. Taking serial-correlation into account in tests of the mean. *Journal of Climate*, 8(2):336–351, 1995.